Progress in Developing a Clinically Viable Diagnostics Using Whispering Gallery Mode Resonators

By

Daniel C. Kim

Submitted to the graduate degree program in Chemistry and the Graduate Faculty of the University of Kansas in partial fulfillment of the requirements for the degree of Doctor of Philosophy

_____
Chairperson: Dr. Robert C. Dunn

_____
Dr. Susan Lunte

_____
Dr. Mario Rivera

_____
Dr. Yong Zeng

_____
Dr. Rongqing Hui

Date Approved: May 3rd, 2016

The Dissertation Committee for Daniel C. Kim
certifies that this is the approved version of the following dissertation:

Progress in Developing a Clinically Viable Diagnostics Using Whispering Gallery Mode Resonators

_____
Chairperson: Dr. Robert C. Dunn

Date Approved: May 25th, 2016

Abstract

Whispering gallery mode (WGM) resonators enable the label-free detection of analytes based on refractive index sensing. These WGM microsphere resonators achieve high sensitivities by confining light within their cavity. This enhances the pathlength amplifying sample-light interactions leading to improved sensing metrics. By taking advantage of their small footprint, high sensitivity and flexible design, we have developed a variety of unique label-free analytical platforms. We recently demonstrated a large scale multiplexed imaging platform where hundreds of resonators are simultaneously characterized by coupling a fluorescent dye to the resonator surface. This scheme was used to quantify several biomarkers of ovarian cancer with detection limits comparable to ELISA. Recently, we extended this technique by developing an evanescent scattering approach for characterizing the WGM resonances. Since signal levels scale with excitation power, measurements can be done with high temporal resolution using less expensive imaging equipment. This approach, therefore, offers promise for developing fast, inexpensive, sensitive detection for the multiplexed detection of disease biomarkers.

Making improvements to clinical tools used for diagnosing cancer have been of considerable interest as it can drastically improve the prognosis of patients. One such example is the introduction of prostate specific antigen as an early screening tool using ELISA. Since its introduction prostate cancer mortality rates have dramatically decreased due to the detection of the disease in early stages where the cancer is more treatable. The early detection approach can be adopted for all diseases such as ovarian cancer and multiple myeloma. However, challenges in identifying a single biomarker that exists in lower, undetectable concentrations have limited the development of early screening tools for many types of cancers. Additionally, immunoassay platforms amenable to routine screening must be quick, cost-effective and easily-integrated into the clinic.

WGM platforms provide an opportunity to detect and identify protein and non-protein disease biomarkers as a sensitive and multiplex approach. Additionally, WGM can be integrated with numerous fluidic platforms that improve the practical aspects of the development of a device which is critical for the translation of the tool into a clinical setting. Here, the integration of WGM detectors into platforms such as capillary electrophoresis (CE) and droplet analysis will be presented. Separation of serum using CE presents the advantage of separation non-diagnostically relevant proteins which can reduce non-specific binding. The progress of developing a WGM resonators platform for the diagnostics of multiple myeloma using CE-WGM separations will be discussed.

Acknowledgements

It has truly been a great journey. Looking back on where I was, who I was and what I hoped to accomplish, I can say with confidence that I have experienced something truly special. In the bliss of being in love with science (may it be slightly fortunately ignorant), I initially stumbled into graduate school. I say this because I initially did not understand the gravity of what graduate school meant. Fortuitously, I have had so much help in my training and development, and thus, have many people to thank for their support and life-long friendships.

During my graduate career, Dr. Robert Dunn (Bob) has continuously invested his time and effort to support, encourage, challenge and expand my knowledge and scientific abilities. His guidance has been invaluable to me moving forward as I pursue my scientific career. I have and will continue to appreciate Dr. Dunn's enthusiasm, high expectation and his humor. He always brought me back to earth and reminded me of the big picture. He has been an honest mentor and a true friend and it has been an honor to learn from him.

I am continually thankful to Dr. Siahaan, Dr. Volkin and the rest of the NIH-NIGMS biotechnology training grant staff for their support. I am extremely grateful for the financial support and all of the extra-circular opportunities that have opened many professional doors. Their hard work for organizing, planning and obtaining the training grant will always be appreciated. Additionally, I would like to thank Nancy Helm and other KU Pharmaceutical Chemistry staff.

I would also like to thank current and former members of the Dunn Lab. "Git 'er Dunn" was one of the first things I was introduced to by Dr. Heath Huckabay and Dr. Kevin Armendariz. I believe there is also a shirt design floating around… They have been instrumental in the early stages of my graduate career, in getting situated and comfortable in the lab and set the bar for the level of work required during my career here. I also would like to thank Dr. Sarah Wildgen for her willingness to always help in any possible way. Sarah was my go-to, day to day scientific and graduate student help. I am proud to

have worked with her on our whispering gallery mode project. I also would like to thank Sonivette Colon-Rodriguez and Nikki Savastano for being excellent undergraduate researchers who have assisted me on numerous aspects of my project such as the microfluidics and antibody functionalization. Additionally, I would like to thank Brittany Dewitt, Chess Volp, Lin Zeng and Brittany Sanders for their support as members of the Dunn Lab.

I could not have gotten through graduate school without the support of my parents who have listlessly given their love to me. They have been a rock and foundation my whole life and have taught me to stay challenged, think big and love always. To my sisters, who have always showered me with love and respect. To my friends, Amanda Furness, Ryan Johnson and Nhan To who I have always relied on to have great conversations about science, life, sports and games. Last but not least, CL, I am so fortunate to have you in my life for your continuing understanding and uncanny ability to always cheer me up. You have been the main source of my confidence and helped me through the toughest parts of my graduate career.

I have been blessed to have this finished this chapter of my life with all your supports. I cannot wait to stumble into my next fortunate adventure.

Table of Contents

List of Figures

List of Tables

Chapter 1

Introduction and Overview

1.1 Motivation for Biosensing in Cancer Diagnostics

Cancer is among the leading causes of death worldwide with over 14 million new cases each year.[1] In 2016, over 1.6 million new cases of cancer will be diagnosed and more than half a million will die from the disease in the U.S. alone.[1] It is postulated that with population growth and the unelucidated biochemistry of cancer that new cases will rise to 22 million within the next two decades.[1] These devastating statistics continually place a burden in social and economic facets of society and will remain a challenge for generations to come.

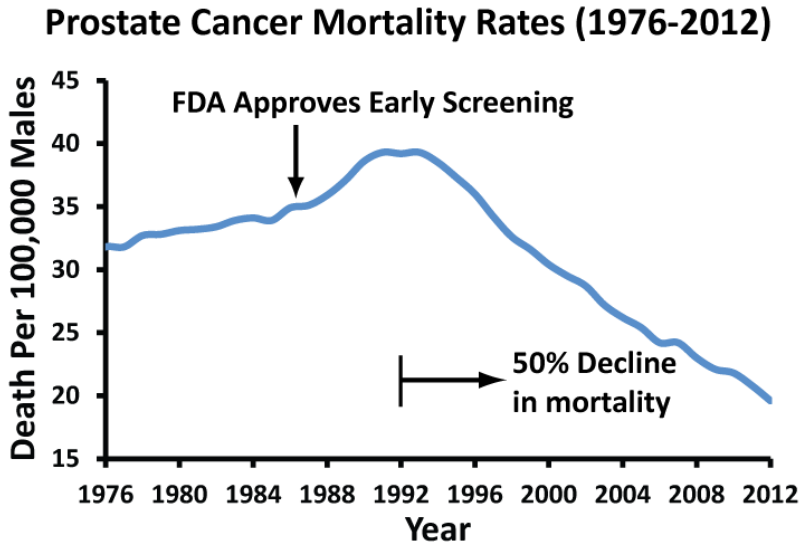

Figure 1.1. Prostate cancer mortality rates from 1976-2012. FDA approved the use of PSA as a screening tool in 1986. There has been a 50% decline in prostate cancer mortality since 1992.[2]

To tackle these challenges, improvements in cancer therapeutics alone may be insufficient. The success of prostate specific antigen (PSA) as an early diagnostic marker for prostate cancer demonstrates how early diagnosis is directly tied to the patient's prognosis.[3-5] As shown in **Figure 1.1**, since the introduction of the new diagnostic into clinics in 1986, prostate cancer has seen a markedly lower mortality rate for the disease. Since 1992, 4 years after the implementation of PSA for early screening, there has been a 50% decline in prostate cancer mortality rates.[6-8] Further studies have confirmed that the reduced mortality rates are largely due to the effectiveness of the diagnostic tool that allowed patients with prostate cancer to be identified at earlier stages.[3,7,9] The early detection approach, as demonstrated by a clinical implementation of PSA for prostate cancer diagnosis, holds considerable promise in improving cancer patient prognosis and thus, reducing cancer burden on our society.

Screening methods for men and women have been established and recommended in an effort to detect cancer early. Women ages from 40 to 44 are recommended to start annual breast cancer screening with mammograms.[10] Women older than 45 are told they should get mammograms every year. Mammograms are effective in catching 78% of breast cancer cases, however, the chances of a false positive after 10 mammograms is 50 to 60 percent.[11,12] These false positives prompt biopsies to confirm the diagnosis, thus, cause unnecessary discomfort to the patient. Minimizing false positives and reducing the need for invasive tests for cancer diagnosis would be highly beneficial for all cancer types. This dissertation is focused on the development of a diagnostics platform using blood tests to detect potential biomarkers for various cancers. In this chapter, we highlight the need for early diagnostics using the case study of ovarian cancer. Then, we discuss the need for a platform amenable for routine screening in the case of multiple myeloma.

1.1.1 Case for Early Diagnostics: Ovarian Cancer

Ovarian cancer is the most prevalent and fatal gynecological cancer. While it only contributes to 3% of cancer cases in women, it is the fifth-leading cause of cancer related deaths with a fatality rate of over 60%.[13-15] These statistics have changed little over the last several decades despite ongoing therapeutics development and improved clinical practices.[14,16] The high fatality rates are not entirely due to the aggressiveness of the disease; as ovarian cancer is entirely treatable when caught early in its progression. However, ovarian cancer is asymptomatic until distant or stage IV category where most cases of ovarian cancer are diagnosed.[16] **Figure 1.2** illustrates ovarian cancer 5-year survival rates (blue) and percentage of women diagnosed (red) plotted with respect to ovarian cancer stage:

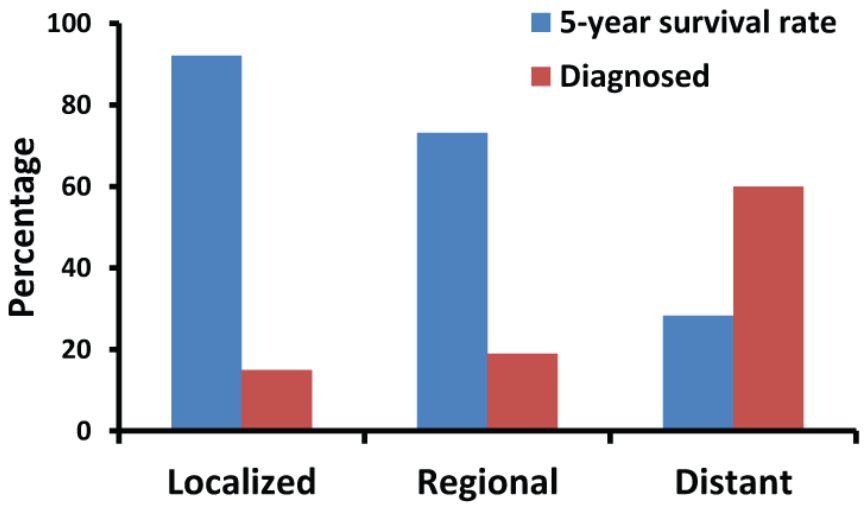

Figure 1.2. The 5-year survival rates (blue) of ovarian cancer patients and percentage of women diagnosed (red) in localized, regional and distant stages of ovarian cancer

This figure illustrates that the survival rates for ovarian cancer diagnosed in localized or stage I/II are over 90%, yet only 10% of ovarian cancer cases are identified at this stage. Greater than 60% of ovarian cancer cases are diagnosed in Stage IV (distant) where 5-year survival rates are unfortunately less than 30%.[13,15-17] Early detection of ovarian cancer, while possible, remains a challenge due to vague, non-specific early symptoms and limited ability of existing screening methods. Ultrasounds and blood

tests for cancer antigen-125 (CA-125) are currently used in the clinic as diagnostic tests, however they lack the specificity for the disease and more importantly have difficulty in detecting early stages of ovarian cancer, where the disease is most treatable.[18,19] Ongoing biomarker research have identified many other potential biomarkers, however, a single biomarker has yet to have the required specificity to be employed as a screening test. Many have suggested that multiplexing may be a promising approach. The current immunoassay technique, enzyme-linked immunosorbent assay (ELISA), used in the clinic is not easily multiplexable and exhibit other drawbacks which will be discussed in detail later. Thus, to tackle this disease and improve ovarian cancer patient outcome, new routine screening tools for early diagnosis must be developed.[19]

1.1.2 Case for Screening Platform: Multiple Myeloma

Multiple Myeloma (MM) is a plasma cell disease that leads to myelomas or plasma cell tumors in bone marrow. Formation and build-up of abnormal plasma cells can lead to anemia, bone and calcium problems, impaired immune response, and kidney problems. MM occurs when plasma cells located in the bone marrow become cancerous and exhibit unregulated growth. They can produce a tumor called a plasmacytoma which generally develops in the bone but in rare situations can migrate into the tissue.[2] The production of abnormal plasma cells causes various systematic symptoms in patients. For example, abnormal plasma cells have limited ability to produce antibodies that help fight off infections as part of the immune system. The suppressed immune system can be a symptom of MM patients.[20] Another indication of MM may be low blood counts due to the overgrowth and crowding of normal blood-forming cells leading to anemia. Additionally, abnormal plasma cells signal the breakdown of bones and limit new bone formation thus weaken bones. Fractured bones are a common symptom of MM patients with increased calcium levels in blood due to bone breakdown.[2,20]

In 2016, it is estimated that 30,330 new cases of MM will be diagnosed and 12,650 patients will die from the disease, making it the fourteenth most deadly cancer.[2] In addition, MM is especially difficult to manage due to its 100% relapse rate following treatment. Diagnostic tools for multiple myeloma currently exist, but exhibit significant drawbacks.[21-23] Patients are recommended for a serum protein electrophoresis (SPE) test which stratifies all serum proteins present into zones[24-26] as shown in **Figure 1.3**.

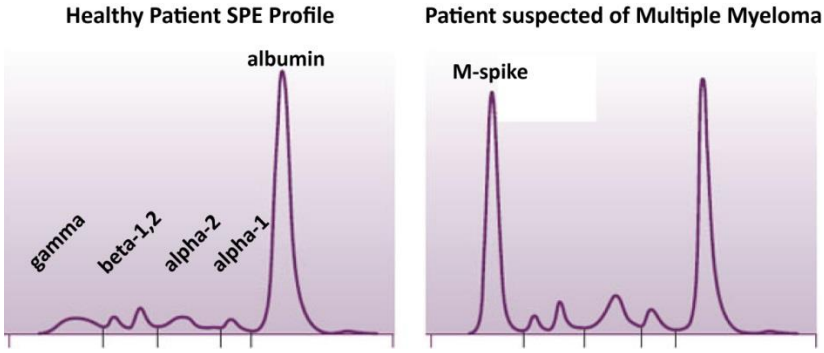

Figure 1.3. Capillary serum protein electrophoresis profile illustrations of healthy patient (left) and suspected multiple myeloma patient (right). An abnormal gamma band peak indicates a monoclonal gammopathy or M-spike.

The SPE profiles shown in **Figure 1.3** are representative of a healthy patient (left) where the gamma-globulin zone is low compared to the profile shown on the right, where there is a spike in the gamma-globulin region due to a monoclonal gammopathy (M-spike).[22,25] Only 17% of all M-spikes are found to be a result of multiple myeloma and thus, alone is a poor diagnostic tool.[26] The initial SPE must be paired with immunoassays for free light chains or quantification of immunoglobulin types for a confirmed diagnosis.[27-30] Furthermore, the quantification of numerous markers that can elucidate the tumor initiation, staging and type of the multiple myeloma such as lactate dehydrogenase (tumor initiation)[31] and β_2-microglobulin (staging)[31,32] would requires several separately performed immunoassays.

An ideal platform for MM diagnosis would couple the advantages of the fast screening of SPE with the specificity of biomarker immunoassays. The 100% relapse rate of MM presents a lifelong fiscal burden for current and former MM patients. The current platform for MM diagnosis with separate SPE and immunoassays ties up valuable clinical resources leading to higher patient costs. In addition, MM requires constant monitoring of patients before, during and after treatment thus the fragmented form of testing with SPE and several immunoassays is undesirable.[21] Therefore, further innovations in MM diagnostics must be made to mitigate the patient and clinical burden placed by this disease.

1.2 Desired Qualities of a Diagnostic Test for Cancer

1.2.1 Performance metrics of a Diagnostic

Large population testing for cancer must have extremely low false positive rates as a false positive result can lead to the use of invasive biopsies for confirmation. A screening tool must exhibit high sensitivity and specificity for a particular disease to be effective. Therefore, it is important to characterize a diagnostic tool's overall screening sensitivity, specificity and positive predictive values (PPV). Sensitivity is defined as the probability of a test that returns a true positive (positive result on an ill-patient) indication and is defined as:[33]

$$Sensitivity = \frac{\#\ of\ true\ positives}{\#\ of\ true\ positives + \#\ of\ false\ negatives} \qquad \text{Eq. 1.1}$$

For example, if a test is 100% sensitive, every ill-patient tested would return a positive result, in other words, no ill-patient would return a negative test result. The specificity of a diagnostic test is the probability of producing a true negative (negative result on a healthy patient) which is shown as:[33]

$$Specificity = \frac{\#\ of\ true\ negatives}{\#\ of\ true\ negatives + \#\ of\ false\ positives} \quad \text{Eq. 1.2}$$

A 100% specific test would produce no false positives. This metric is especially important when evaluating screening tools for cancer as a false positive can lead to biopsy studies. The positive predictive value (PPV) of a test is the probability that an ill person will exhibit a positive test, as defined by:[34]

$$PPV = \frac{\#\ of\ true\ positives}{\#\ of\ true\ positives + \#\ of\ false\ positives} \quad \text{Eq. 1.3}$$

Negative predictive value (NPV) of a test is the probability that a healthy person exhibits a negative test result, as calculated by:[34]

$$NPV = \frac{\#\ of\ true\ negatives}{\#\ of\ true\ negatives + \#\ of\ false\ negatives} \quad \text{Eq. 1.4}$$

The relatively low occurrence rates for deadly diseases such as ovarian cancer (20 in every 100,000)[18] and multiple myeloma (6 in every 100,000)[2] pose a challenge when developing a screening test for use in the general population. A consensus of most gynecologic surgeons and patients feel that no more than 10 operations in a population should be performed to identify a single case of ovarian cancer. Thus, an effective early screen for ovarian cancer requires a sensitivity of at least 75%, specificity greater than 99% and a minimum PPV of 10%.[35] Current tests such as a biopsy or other imaging tests such as an ultrasound are highly specific, but have low PPV values and thus is hard to conceive as a screening test.[36] Additionally, early stages of ovarian cancer are less likely to be

discovered due to the small sizes of tumor masses. Therefore, the current screening methods are ill-suited for early-detection.

Alternatively, there are blood tests for proteins which show considerable promise. When appropriate markers are identified for cancers, these tests are extremely advantageous due to being minimally invasive and information rich. However, for cancers such as ovarian cancer, a blood test specific for early stages of the disease have been difficult to identify. Other approaches to address this challenge are to routinely monitor biomarker levels or identify a panel of biomarkers using a multiplexed test to diagnose ovarian cancer.[37,38]

1.2.2 Multiplexed Biomarker Detection

The diagnostic performance of detection platforms must also be considered for its practicality and potential for clinical implementation. This section uses ovarian cancer as a case study to illustrate the benefits of a multiplexed approach for cancer diagnostics. Initiatives in biomarker discovery have fortunately provided many potential biomarkers for various cancers. However, biomarkers must exhibit high sensitivity and specificity for a particular cancer for clinical use as a screening tool. For example, a screening tool for low occurrence rate cancers, such as ovarian cancer, requires biomarker specificities greater than 99% to minimize false positives.[35,39] FDA approved markers for ovarian cancer CA-125[40], HE4[41,42] and other putative markers still under investigation such as osteopontin[43], OVX 1[44] and prolactin[45] are shown in **Table 1.1**. A viable ovarian cancer screening tool must exhibit sensitivity, specificity and a minimum PPV of 75%, 99% and 10% respectively.[35] As seen in **Table 1.1**, none of these markers alone provide metrics suitable to diagnose ovarian cancer with 99% specificity.

Table 1.1 Candidate biomarkers for ovarian cancer and their diagnostic capabilities.

Biomarker	Sensitivity	Specificity	Notes
CA-125	40 to 78%	77 to 86%	FDA approved for detecting the most commonly screened protein for ovarian cancer diagnosis. Poor performance alone. [46,47]
HE4	80% to 95%	60% to 96%	Recently FDA approved for post-surgical relapse monitoring. [41,42,47]
Osteopontin	70%	90%	Up-regulated in early stage cancer. Involved in tumor metastasis and progression. [43,48]
OVX-1	40%	83%	Elevated in Stage 1 carcinoma. Also implicated in breast and prostate cancer. [49]
Prolactin	95%	95%	Elevated in ovarian cancer patient serum[50]

Levels of CA-125 and HE4, two proteins approved by the Food and Drug Administration (FDA) as ovarian cancer biomarkers, can assist with diagnosis, used to monitor disease progression or predict reoccurrence of ovarian cancer.[41,44] Currently, elevated CA-125 or HE4 levels prompt an ultrasound test leading the detection of less than 20% of localized ovarian cancer when the disease is most treatable. HE4 has shown promise of higher specificity compared to CA-125, yet alone still lacks the specificity to be used in a routine screening test for ovarian cancer.[41,42] Therefore, these biomarkers combined with other diagnostic tests such as ultrasounds, lack the specificity and sensitivity required for early detection.

Table 1.2 Biomarker panels for ovarian cancer

Biomarker Panel	Sensitivity	Specificity	Detection Method
OVA1: Transthyretin, apolipoprotein, A-1, beta 2-microglobulin, transferrin, CA-125	93%	43%	Multivariate index assay[51]
CA-125, HE4, CEA, VCAM-1	86%	98%	Bead-based immunoassay[39]
Leptin, OPN, PRL, IGF-II	95%	94%	ELISA[52]
CA-125, MIF, Leptin, PRL, OPN, IGF-II	95.3%	99.4%	MS/ELISA[45]

Identifying groups of biomarkers that together can provide improved sensitivity and specificity for ovarian cancer is a promising approach. **Table 1.2** highlights four biomarker panels for ovarian cancer being developed for improved detection of ovarian cancer. The first panel shown in **Table 1.2** shows a highly sensitive test used to generate a malignancy score in women with an identified pelvic mass.[51] However, the specificity of this panel is lower than CA-125 alone. A successful implementation of multiplexed assays like the simultaneous detection of leptin, osteopotin, prolactin and insulin-like growth factor (IGF-II) was able to distinguish early stage ovarian cancer with 95% sensitivity and 94% specificity.[52] When this panel was used in conjunction with CA-125 and macrophage migration inhibitory factor (MIF), the sensitivity and specificity were further improved to 95.3% and 99.4% respectively.[45] This study, however, only included patients with advanced stages of ovarian cancer thus requiring further investigation to explore its utility in early detection of ovarian cancer.[45] Regardless, the addition of more putative biomarkers to a panel can improve the overall diagnostic ability.[38,44,49] More importantly, these multiplexed approaches exhibit improved sensitivity and specificity compared to tests using a single biomarker validating the multiplexed approach.

1.2.3 Label-free Detection of Biomarkers

In addition to the protein-based biomarkers for disease detection, recent work has suggested that small, noncoding ribonucleotides or microRNAS (miRNAs) can also act as specific indicators of a disease state in cancer.[53,54] These noncoding RNAs are 19 to 25 nucleotides are believed to be involved in many biological processes including cellular transcriptome regulatory roles.[53] miRNAs were first linked to cancer for chronic lymphocytic leukemia, where they participate in pathways fundamental to B cell receptor signaling, migration and adhesion and cell to cell interactions.[55] Since then, the role of miRNA in many cancers, including ovarian cancer, has been elucidated. More specifically, numerous miRNA targets (miR-21[56], miR-29a[56], miR-148b[57]) have been identified at elevated levels during early

stages of ovarian cancer. In one study, miR-148b was shown to be overexpressed in 92.21% of asymptomatic women which may be an important early stage biomarker pending further investigation.[57]

The accommodation of multiple classes of biomarkers to a diagnostic tool is a challenge in analytical platforms such as an enzyme linked immunosorbent assay (ELISA). The most straightforward approach to a multiplexed assay is to develop a label-free detection scheme. This approach can also avoid additional chemistries required to introduce labels which can lead to losses in biomolecular function. Label-free detection can enable a homogeneous platform for the detection of proteins and miRNA in a single assay. Furthermore, label-free platforms can reduce reagent costs, time and chemistry which can facilitate the transfer of the assay into the clinic. To access nucleic acids as a source of biomarkers in addition to proteins, new label-free analytical approaches are needed to improve clinical diagnostics for cancers.

1.2.4 Detection limits

ELISA (Enzyme linked immunosorbent assay) is considered the current "gold standard" for clinical diagnostics with detection limits in the general range of pM. While this is sufficient for existing blood tests such as PSA in prostate cancer, it may be advantageous to push for lower limits of detection for future early stage cancer biomarkers. This would make possible the detection of upregulated or downregulated biomarkers at the earliest stage of pathogenesis.

Lower detection limits may also aide in applications such as companion diagnostics. Companion diagnostics is generally defined as "a device that provides information that is essential for the safe and effective use of a corresponding therapeutic product" by the FDA.[58] This technology can be used to identify patients who are at increased risk for side-effects as a result of treatment and also monitor the patient response to a treatment. The trends in personalized medicine and companion diagnostics for cancer therapeutics require the monitoring of small changes (less than 1 pM) in analyte concentrations

which can have significant clinical impact.[59] To enable treatment monitoring and the growing role of companion diagnostics, we must strive to develop lower detection limit detection platforms.

1.2.5 Other Diagnostic Platform Considerations

During the development of a diagnostic for cancer, we have already discussed the required analytical performance metrics such as sensitivity, specificity and detection limits. The current blood based tests used for ovarian cancer in the clinic have limited diagnostic capabilities as a stand-alone exam. Blood based tests are often cheap and provide some degree of diagnostic capability thus utilized as a part of a diagnostic pathway where elevated CA-125 levels, for example, lead to the more expensive ultrasound exam. Since, positive results in the blood test lead directly to another confirmation test, ultimately the patient can receive large medical fees. Therefore, improved diagnostic capabilities for a blood based screening test can significantly reduce the cost for the patient and be more accessible for the patients.

ELISAs and blotting techniques are relatively inexpensive but may not provide enough analytical performance to precisely identify minute differences in biomolecular profiles. Additionally, these platforms are generally limited to a single analyte per test leading to lower throughput in multiplexed assays of biomarker panels. To make big strides in the field of cancer diagnostics, a platform that is low reagent consumption, high throughput, low clinical resource burden and low costs must be developed.

1.3 Clinical Immunoassay: Enzyme linked immunosorbent assay

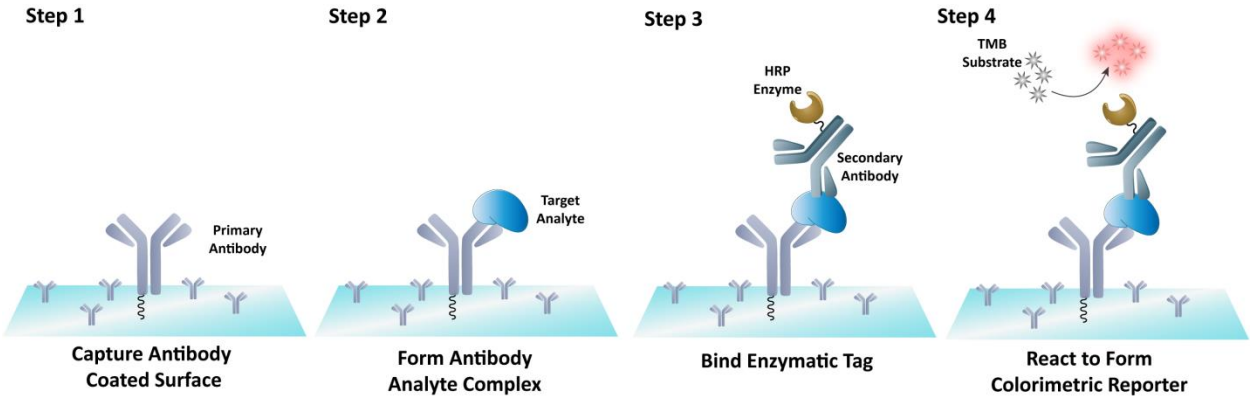

Figure 1.4. In step 1, the antibodies are coated onto the surface by either covalent attachment or physical adsorption. Then, the target analyte is introduced forming an antibody-antigen complex. Addition of a secondary antibody linked to an HRP enzyme binds to the complex. Then TMB is introduced in the presence of hydrogen peroxide to form a colorimetric product.

ELISA is considered the "gold standard" for diagnostics in the clinic as it provides high analyte specificity and robust detection of proteins in biological fluids. The method utilizes a capture and subsequent detection motif taking advantage of antibody-antigen interactions. Since the development of ELISA in the 1970s, there are many versions of the technique. A popular assay schematic is shown in **Figure 1.4** that illustrates a typical sandwich-based ELISA method.

In step 1, the assay wells are coated with the capture antibody bound using either covalent chemistries or noncovalent interactions. In step 2, the target protein within a sample solution is captured by the surface immobilized antibody forming the antibody-analyte complex. After the capture of the analyte, a secondary antibody bound to an enzymatic tag, such as horseradish peroxidase (HRP) is introduced and incubated with the solution in step 3. Finally, in step 4, for colorimetric detection, 3,3',5,5'-tetramethylbenzidine (TMB) is added. TMB reacts with HRP as a substrate being catalytically oxidized, by hydrogen peroxide, to form a colorimetric, diamine product.[60] For protein quantitation, absorbance at 450 nm is measured and compared to calibration wells.

There are many attractive features of ELISA that contribute to its wide use for biomarker diagnostics. The sandwich-ELISA approach exhibits higher degrees of specificity and reduced cross-reactivity for the analyte due to the use of a primary capture antibody and a secondary detection antibody. The assay also uses amplification of the colorimetric signal using a high turnover enzyme HRP resulting in low detection limits (nM) and high sensitivity. The assay platform is also simple and easily performed in multi-well plates that have now been developed into automated instruments. Despite these advantages, there are some key drawbacks in ELISA that limit its utility for early detection and treatment monitoring applications.

ELISA is a relatively reagent intensive technique that involves numerous incubation steps. The utilization of two binding antibodies as well as an enzymatic reaction to produce the colorimetric species all requires long incubation time and several reagents. The platform is generally limited for the detection of proteins due to the use of antibodies. A drawback of ELISA that labeling of the detection antibody with an enzyme can affect its biomolecular function, which may reduce its binding performance. Additionally, the fundamental requirement that the analyte of interest have two binding sites is a limitation. Furthermore, the detection and quantitation of a single protein must be performed in its own well due to the general colorimetric signal and thus is not easily amenable for multiplexing.

Label-free techniques overcome these limitations by allowing a homogeneous and general platform for the detection of proteins and nucleic acid biomarkers. Furthermore, label-free platforms reduce reagent usage, cost and time required for biomarker quantitation. Additionally, they can enable the multiplexed detection of biomarker panels for cancers to improve patient prognosis. However, these techniques are not without their drawbacks. Non-specific binding and reduced specificity due to the use of a single antibody versus two in ELISA and signal amplification required for low detection limits for label-free techniques are significant challenges. Therefore, all of the mentioned factors and other

criteria such as cost, throughput and detection limits, which can influence the adoption of these techniques into the clinic, must be evaluated.

1.4 Review of Current State of Label-Free Biosensors

Label-free techniques allow real-time detection of virtually any biomolecular complex requiring minimal sample preparation and reduced assay development. In these platforms, no additional labels or modification of the analyte of interest is required for their detection. Because of this, label-free techniques can be flexibly designed for many applications. These advantages are well-suited for the development of low cost, inexpensive, high throughput and clinically viable diagnostics. This section will highlight particular label-free techniques which have shown considerable promise for clinical applications.[61] **Table 1.3** compares various criteria relevant to clinical diagnostic platform development.

Table 1.3 Label-free biosensing techniques for the detection of biomarkers

Sensing Technique	Scalability/ Feasibility	Multiplexing Capability	Detection Limits	Throughput	Cost
Nanostructures and Nanowires[62-64]	Difficult	Good	fM	Moderate	High
Quartz-Crystal Microbalance[65]	Moderate	Limited	µM-pM	Poor	Moderate
Surface Acoustic Wave[66]	Moderate	Poor	pM-fM	Poor	Moderate
Interferometry[66]	Moderate	Poor	pM-fM	Poor	Low to Moderate
Surface Plasmon Resonance[66]	Moderate	Moderate	µM-pM	Moderate	High
Optical Resonators[66-69]	Mixed	Mixed	µM-aM	Mixed	Low

1.4.1 Electrochemical-Based Biosensors

Label-free electrochemical sensors are based on measuring the change in current, potential or conductivity that occurs when a target molecule binds to the functionalized sensor surface. These devices are particularly attractive due to their high sensitivities and simplicity with which they are conjugated with miniaturized hardware. An implementation of a electrochemical antibody-based biosensor by Kerman and colleagues measured the binding of human chorionic gonadotropin (hCG) with detection limits of 20 pM in human urine.[70] This group used a three-electrode system with carbon paste electrode as the working electrode, Ag/AgCl as the reference and platinum as the auxiliary electrode. More recently, extremely sensitive and multiplexed electrochemical based biosensors have been developed using higher conductivity graphene material and improved fabrication of nano-scale electrodes.[62,63]

Nanowires are mainly employed as miniature electrochemical sensors. The diameters of these nanowires are comparable to the biomolecular species being measured offering excellent signals which can ultimately be interfaced to macroscopic instruments. Biochemically functionalized wires can detect biomolecular interactions as changes in the dielectric environment around the nanowire. Extremely high sensitivity has allowed for the detection of a single virus. These impressive metrics combined with the development of nanowire arrays has enabled the simultaneous detection of three cancer biomarkers in serum samples. PSA with detection limits of ~2 fM have been routinely achieved using nanowire bionsensors.[64] Furthermore, fabrication of an array of nanowires demonstrated the multiplexed detection of PSA, carcinoembryonic antigen and mucin-1 with minimal cross-reactivity when each antigen was introduced. They also detected PSA spiked into donkey serum but show significantly reduced signal to noise ratios.[64] This may be a result of non-specific detection which can be a challenge for nanowires as they detect all changes in their dielectric environment. Though nanowire electrochemical sensors hold significant promise, a challenge for the adoption of these sensors is that

they require precise nanostructure fabrication equipment which drive up the cost of each sensor and limit their use in the clinical setting.

1.4.2 Acoustic-Based Biosensors

Acoustic sensors are based on vibrating elements which create acoustic waves. These waves can propagate along a surface for surface acoustic wave (SAW) or in the bulk as bulk acoustic wave (BAW). For biosensing, when molecules absorb to the sensor surface, the change in amplitude or frequency of the resonator can be measured. Quartz crystal microbalance (QCM) is a bulk acoustic wave device which utilizes a piezoelectric quartz crystal. When the crystal is electrically excited using two electrodes the resonance frequency can be measured. A functionalized crystal used in this platform can detect specific binding events down to the pM level.[65] However, bulk acoustic wave devices experience losses in detection limits in solution due to acoustic losses caused by longitudinal waves into the liquid which limit performance.

Surface acoustic waves overcome this limitation by utilizing acoustic waves that travel along the substrate. In this platform the electrodes are interdigitated as shown in **Figure 1.5** creating confined acoustic energy near the surface when a potential is applied across the system.

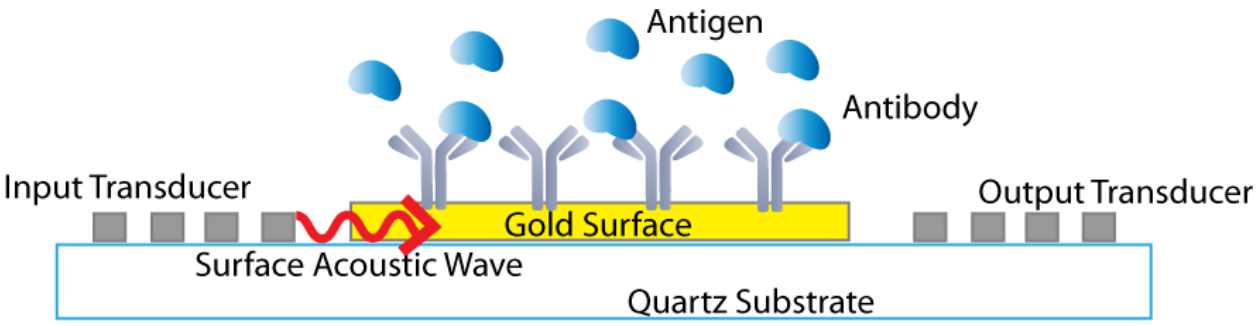

Figure 1.5. A schematic of a surface acoustic wave biosensor. The interdigitated electrodes are used to produce a surface wave along a piezoelectric substrate. Any binding event on the surface of the material is observed as a delay line. The wave is measured using second electrode.

As shown in **Figure 1.5**, an input transducer forms a surface acoustic wave that travels through antibody functionalized gold surface. The output transducer detects the resulting surface acoustic wave after interrogation of the gold film. Changes in the surface acoustic wave frequency are related to the mass as antigen bind to the surface. These systems have theoretical mass detection limitations corresponding to fM levels which would be extremely competitive among current biosensors.[71] However, because the frequency change is influenced by many factors such as conductance of the liquid, dielectric and elastic constants of the adsorbent which are difficult to control, the implementation of these devices remain a challenge for clinical applications. Additionally, multiplexing is difficult to achieve in these devices without the use of more complicated electrode fabrication of additional transducing and detecting electrodes.

1.4.3 Optical-Based Biosensors

Label-free optical biosensors rely on measuring the interaction of light with surface adsorbed molecules. These platforms often rely on measuring refractive index which is a parameter that describes how light propagates through a medium. Refractive index-based sensors that are simple, low cost and highly sensitive exist in various platforms. In general, the sensing mechanism is similar for many optical biosensors where biomolecular interactions on a surface can be quantified in real-time by monitoring the changes in intensity, wavelength, polarization or phase of the light after being reflected at the active surface.

1.4.3.1 Surface Plasmon Resonance

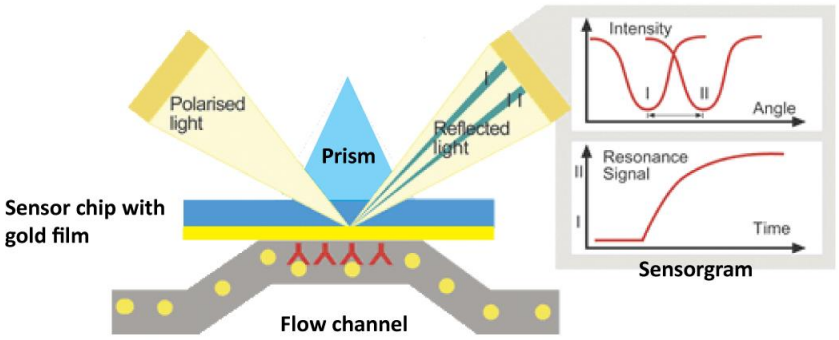

Figure 1.6. A schematic of a surface plasmon resonance is illustrated here. Surface plasmons are oscillations in the free electron density excited with an incident laser. A sensor chip with gold is commonly utilized as a substrate. The angle of reflection is measured as analyte binding to the sensor chip leading to the sensogram illustrated here.

A common and commercialized refractive index platform is surface plasmon resonance (SPR) illustrated in **Figure 1.6**. SPR utilizes metal surface plasmons to probe analyte interactions.[72,73] Surface plasmons are oscillations in the free electron density which are created when a metal coated dielectric material is excited with an incident laser. These resonances can be measured by monitoring the angle of reflection of the light that is diffracted on the metal coated dielectric interface. The angle of reflection depends on the refractive index of the surrounding media within the exponentially decaying evanescent wave. By functionalizing the surface with a biocapture molecule, binding events may be measured in real time using this approach. SPR is amenable to multiplexed assays by using high quality patterns in a SPR imaging approach.[74,75] While possible, the need for precise fabrication of microarrays increases the cost and reduces the scalability of the device which is a drawback for clinical implementation.

1.4.3.2 Interferometry

Interferometry based sensors are relatively simple devices that rely on measuring changes in the phase velocity of light resulting from the accumulation of biomolecules on a sensing strip.[66,76] These methods have been developed to sense biomolecules with detection limits in the femtomolar range.[77]

However, most interferometry devices have limited multiplexing capabilities thus reducing throughput. Alternatively, biolayer interferometry (BLI) uses white light interferometry at the end of a fiber optic to measure the thickness of transparent-thin film and can be easily multiplexed.[78] The commercialized Octet system (ForteBio, Menlo Park, CA), can measure responses from up to 16 sensors set up in parallel, where the sensors are dipped into the sample well.[79] The drawback to BLI is that the limit of detection is typically higher compared to most other interferometric techniques, which can make it difficult for the measurement of early stage biomarkers of cancer. Optical resonator sensors are emerging as an attractive alternative for biosensing for highly sensitive and multiplexed biosensing.

1.4.3.3 Optical Resonators

Optical resonator based sensors take advantage of a phenomenon referred to as whispering gallery mode (WGM) resonances.[68] Microcavities made of dielectric materials support the recirculation of light within the structure through continuous total internal reflection. When the resonance condition of the resonator is satisfied, the resonant wavelength can be directly related to the surrounding refractive index useful for sensing.[80-82] The highly efficient light recirculation leads to high sensitivities and low detection limits enabling detection of a single virus.[69,83] These promising optical resonator platforms continue to be developed for multiplexed sensing.[84,85] WGM resonators offer low detection limits, label-free, small footprint and high sensitivities for biosensing. Here, the development of WGM based biosensors will be discussed in subsequent chapters, including a discussion of their fundamental working theory and their applications and development.

1.5 Motivation for Dissertation

The dire statistics of cancer mortality rates and overall burden placed on society by cancer calls for a need for newer diagnostic approaches. The early detection strategy to improve cancer prognosis is highly promising as demonstrated by the 50% reduction in prostate cancer mortality after the introduction of PSA as an early detection biomarker.[9] For this approach to be adopted for all types of cancers, diagnostic platforms must be amenable to multiplexed biomarker panels to overcome the challenges in identifying a single biomarker for a given disease. A screening tool with attributes such as lower detection limits, label-free, compatibility with proteins and nucleic acids, and throughput can drastically improve cancer patient prognosis.

Currently, a screening method for most cancers that accommodates all of these criteria is still under development. While ELISA is the most popular clinical diagnostic tool and gold standard for diagnostics, it has limited multiplexing capabilities, limited compatibility with nucleic acids and low overall throughput. This creates challenges for developing large scale screens. To overcome these challenges, the development of optical resonator label-free biosensors and their integration in microfluidic platforms for small volume, real-time and inexpensive assays will be discussed. The following chapters are devoted to improvements made for WGM label-free diagnostic platforms working towards a clinically viable assay platform.

1.6 References

1. Siegel, R. L., et al. Cancer statistics, 2015. *CA: A Cancer Journal for Clinicians* **2015**, *65*, 5-29.
2. www.cancer.org.
3. Welch, H. G., et al. Prostate cancer diagnosis and treatment after the introduction of prostate-specific antigen screening: 1986–2005. *Journal of the National Cancer Institute* **2009**.
4. Labrie, F., et al. Serum prostate specific antigen as pre-screening test for prostate cancer. *The Journal of urology* **1992**, *147*, 846-851; discussion 851-842.
5. Heijnsdijk, E. A., et al. Quality-of-life effects of prostate-specific antigen screening. *New England Journal of Medicine* **2012**, *367*, 595-605.
6. Howrey, B. T., et al. The Impact of PSA Screening on Prostate Cancer Mortality and Overdiagnosis of Prostate Cancer in the United States. *The Journals of Gerontology Series A: Biological Sciences and Medical Sciences* **2013**, *68*, 56-61.
7. Hankey, B. F., et al. Cancer surveillance series: interpreting trends in prostate cancer—part I: evidence of the effects of screening in recent prostate cancer incidence, mortality, and survival rates. *Journal of the National Cancer Institute* **1999**, *91*, 1017-1024.
8. Hsing, A. W., et al. International trends and patterns of prostate cancer incidence and mortality. *International journal of cancer* **2000**, *85*, 60-67.
9. Etzioni, R., et al. Quantifying the role of PSA screening in the US prostate cancer mortality decline. *Cancer Causes & Control* **2008**, *19*, 175-181.
10. Jatoi, I. Breast cancer screening. *The American journal of surgery* **1999**, *177*, 518-524.
11. Tabar, L., et al. Reduction in mortality from breast cancer after mass screening with mammography: randomised trial from the Breast Cancer Screening Working Group of the Swedish National Board of Health and Welfare. *The Lancet* **1985**, *325*, 829-832.
12. Elmore, J. G., et al. Ten-year risk of false positive screening mammograms and clinical breast examinations. *New England Journal of Medicine* **1998**, *338*, 1089-1096.
13. Moyer, V. A. Screening for ovarian cancer: US Preventive Services Task Force reaffirmation recommendation statement. *Annals of internal medicine* **2012**, *157*, 900-904.
14. Yap, T. A., et al. Beyond chemotherapy: targeted therapies in ovarian cancer. *Nat Rev Cancer* **2009**, *9*, 167-181.
15. Gajjar, K., et al. Symptoms and risk factors of ovarian cancer: a survey in primary care. *ISRN obstetrics and gynecology* **2012**, *2012*.
16. Jacobs, I. J., et al. Progress and challenges in screening for early detection of ovarian cancer. *Molecular & Cellular Proteomics* **2004**, *3*, 355-366.
17. Chambers, A. F., et al. Ovarian cancer biomarkers in urine. *Clinical cancer research* **2006**, *12*, 323-327.
18. Neesham, D. Ovarian cancer screening. *Australian family physician* **2007**, *36*, 126.
19. Etzioni, R., et al. The case for early detection. *Nature Reviews Cancer* **2003**, *3*, 243-252.
20. Mahindra, A., et al. Multiple myeloma: biology of the disease. *Blood Reviews* **2010**, *24, Supplement 1*, S5-S11.
21. Korthals, M., et al. Molecular monitoring of minimal residual disease in the peripheral blood of patients with multiple myeloma. *Biology of Blood and Marrow Transplantation* **2013**, *19*, 1109-1115.
22. Kyle, R. A., et al. Monoclonal gammopathy of undetermined significance. *British journal of haematology* **2006**, *134*, 573-589.
23. Yasui, H., et al. Recent advances in the treatment of multiple myeloma. *Current pharmaceutical biotechnology* **2006**, *7*, 381-393.

24. Schrier, S. Multiple myeloma and related serum protein disorders. *Scientific American Medicine, New York: Scientific American, Inc* **1994**, *9*, 1-16.
25. Gammopathies, M. V. P. Understanding and interpreting serum protein electrophoresis. *Am Fam Physician* **2005**, *71*, 105-112.
26. Alexanian, R., et al. Differential diagnosis of monoclonal gammopathies. *Archives of Pathology and Laboratory Medicine* **1999**, *123*, 108-113.
27. Wochner, R. D., et al. The role of the kidney in the catabolism of Bence Jones proteins and immunoglobulin fragments. *The Journal of experimental medicine* **1967**, *126*, 207-221.
28. Jenner, E. Serum free light chains in clinical laboratory diagnostics. *Clinica Chimica Acta* **2014**, *427*, 15-20.
29. Tate, J. R., et al. Practical considerations for the measurement of free light chains in serum. *Clinical chemistry* **2003**, *49*, 1252-1257.
30. Graziani, M. S., et al. Serum free light chain analysis in the diagnosis and management of multiple myeloma and related conditions. *Expert review of molecular diagnostics* **2014**, *14*, 55-66.
31. van Rhee, F., et al. High serum-free light chain levels and their rapid reduction in response to therapy define an aggressive multiple myeloma subtype with poor prognosis. *Blood* **2007**, *110*, 827-832.
32. Greipp, P. R., et al. International staging system for multiple myeloma. *Journal of Clinical Oncology* **2005**, *23*, 3412-3420.
33. Altman, D. G., et al. Diagnostic tests. 1: Sensitivity and specificity. *BMJ: British Medical Journal* **1994**, *308*, 1552.
34. Altman, D. G., et al. Statistics Notes: Diagnostic tests 2: predictive values. *Bmj* **1994**, *309*, 102.
35. Clarke-Pearson, D. L. Screening for ovarian cancer. *New England Journal of Medicine* **2009**, *361*, 170-177.
36. Menon, U., et al. Sensitivity and specificity of multimodal and ultrasound screening for ovarian cancer, and stage distribution of detected cancers: results of the prevalence screen of the UK Collaborative Trial of Ovarian Cancer Screening (UKCTOCS). *The lancet oncology* **2009**, *10*, 327-340.
37. Terry, K. L., et al. Blood and urine markers for ovarian cancer: a comprehensive review. *Disease markers* **2004**, *20*, 53.
38. Hwang, J., et al. Correlation between preoperative serum levels of five biomarkers and relationships between these biomarkers and cancer stage in epithelial overian cancer. *Journal of gynecologic oncology* **2009**, *20*, 169-175.
39. Yurkovetsky, Z., et al. Development of a multimarker assay for early detection of ovarian cancer. *Journal of Clinical Oncology* **2010**, *28*, 2159-2166.
40. Welander, C. What do CA 125 and other antigens tell us about ovarian cancer biology? *Acta obstetricia et gynecologica Scandinavica. Supplement* **1991**, *155*, 85-93.
41. Hellström, I., et al. The HE4 (WFDC2) protein is a biomarker for ovarian carcinoma. *Cancer research* **2003**, *63*, 3695-3700.
42. Anastasi, E., et al. HE4: a new potential early biomarker for the recurrence of ovarian cancer. *Tumor Biology* **2010**, *31*, 113-119.
43. Kim, J.-H., et al. Osteopontin as a potential diagnostic biomarker for ovarian cancer. *Jama* **2002**, *287*, 1671-1679.
44. Donach, M., et al. Combined use of biomarkers for detection of ovarian cancer in high-risk women. *Tumor Biology* **2010**, *31*, 209-215.
45. Visintin, I., et al. Diagnostic markers for early detection of ovarian cancer. *Clinical cancer research* **2008**, *14*, 1065-1072.

46. Tamakoshi, K., et al. Clinical value of CA125, CA19-9, CEA, CA72-4, and TPA in borderline ovarian tumor. *Gynecologic oncology* **1996**, *62*, 67-72.
47. Nguyen, L., et al. Biomarkers for early detection of ovarian cancer. *Women's health* **2013**, *9*, 171-187.
48. Nakae, M., et al. Preoperative plasma osteopontin level as a biomarker complementary to carbohydrate antigen 125 in predicting ovarian cancer. *Journal of Obstetrics and Gynaecology Research* **2006**, *32*, 309-314.
49. Woolas, R. P., et al. Combinations of multiple serum markers are superior to individual assays for discriminating malignant from benign pelvic masses. *Gynecologic oncology* **1995**, *59*, 111-116.
50. Levina, V. V., et al. Biological significance of prolactin in gynecologic cancers. *Cancer research* **2009**, *69*, 5226-5233.
51. Ueland, F. R., et al. Effectiveness of a multivariate index assay in the preoperative assessment of ovarian tumors. *Obstetrics & Gynecology* **2011**, *117*, 1289-1297.
52. Mor, G., et al. Serum protein markers for early detection of ovarian cancer. *Proceedings of the National Academy of Sciences of the United States of America* **2005**, *102*, 7677-7682.
53. Calin, G. A., et al. MicroRNA signatures in human cancers. *Nature Reviews Cancer* **2006**, *6*, 857-866.
54. Ferracin, M., et al. Micromarkers: miRNAs in cancer diagnosis and prognosis. *Expert review of molecular diagnostics* **2010**, *10*, 297-308.
55. Calin, G. A., et al. A MicroRNA signature associated with prognosis and progression in chronic lymphocytic leukemia. *New England Journal of Medicine* **2005**, *353*, 1793-1801.
56. Resnick, K. E., et al. The detection of differentially expressed microRNAs from the serum of ovarian cancer patients using a novel real-time PCR platform. *Gynecologic oncology* **2009**, *112*, 55-59.
57. Chang, H., et al. Increased expression of miR-148b in ovarian carcinoma and its clinical significance. *Molecular medicine reports* **2012**, *5*, 1277-1280.
58. Khoury, J. D., et al. Next-generation companion diagnostics: promises, challenges, and solutions. *Archives of Pathology and Laboratory Medicine* **2014**, *139*, 11-13.
59. Agarwal, A., et al. The current and future state of companion diagnostics. *Pharmacogenomics and personalized medicine* **2015**, *8*, 99.
60. Josephy, P. D., et al. The horseradish peroxidase-catalyzed oxidation of 3, 5, 3', 5'-tetramethylbenzidine. Free radical and charge-transfer complex intermediates. *Journal of Biological Chemistry* **1982**, *257*, 3669-3675.
61. Hunt, H. K., et al. Label-free biological and chemical sensors. *Nanoscale* **2010**, *2*, 1544-1559.
62. Kasianowicz, J. J., et al. Nanoscopic porous sensors. *Annu. Rev. Anal. Chem.* **2008**, *1*, 737-766.
63. Patolsky, F., et al. Nanowire-based biosensors. *Analytical Chemistry* **2006**, *78*, 4260-4269.
64. Zheng, G., et al. Multiplexed electrical detection of cancer markers with nanowire sensor arrays. *Nature biotechnology* **2005**, *23*, 1294-1301.
65. Vashist, S. K., et al. Recent advances in quartz crystal microbalance-based sensors. *Journal of Sensors* **2011**, *2011*.
66. Fan, X., et al. Sensitive optical biosensors for unlabeled targets: A review. *Anal Chim Acta* **2008**, *620*, 8-26.
67. Chiasera, A., et al. Spherical whispering-gallery-mode microresonators. *Laser & Photonics Reviews* **2010**, *4*, 457-482.
68. Arnold, S., et al. Shift of whispering-gallery modes in microspheres by protein adsorption. *Opt. Lett.* **2003**, *28*, 272-274.

69. Vollmer, F., et al. Whispering-gallery-mode biosensing: label-free detection down to single molecules. *Nat. Methods* **2008**, *5*, 591-596.
70. Vestergaard, M., et al. An overview of label-free electrochemical protein sensors. *Sensors* **2007**, *7*, 3442-3458.
71. Gronewold, T. M. Surface acoustic wave sensors in the bioanalytical field: Recent trends and challenges. *Anal Chim Acta* **2007**, *603*, 119-128.
72. Homola, J. Present and future of surface plasmon resonance biosensors. *Analytical and bioanalytical chemistry* **2003**, *377*, 528-539.
73. Piliarik, M., et al. Surface plasmon resonance biosensing. *Biosensors and Biodetection* **2009**, 65-88.
74. Ruemmele, J. A., et al. A localized surface plasmon resonance imaging instrument for multiplexed biosensing. *Analytical Chemistry* **2013**, *85*, 4560-4566.
75. Lee, H. J., et al. Surface plasmon resonance imaging measurements of antibody arrays for the multiplexed detection of low molecular weight protein biomarkers. *Analytical Chemistry* **2006**, *78*, 6504-6510.
76. Lin, V. S.-Y., et al. A porous silicon-based optical interferometric biosensor. *Science* **1997**, *278*, 840-843.
77. Syahir, A., et al. Label and label-free detection techniques for protein microarrays. *Microarrays* **2015**, *4*, 228-244.
78. Nirschl, M., et al. Review of transducer principles for label-free biomolecular interaction analysis. *Biosensors* **2011**, *1*, 70-92.
79. Cooper, M. A. Optical biosensors: where next and how soon? *Drug discovery today* **2006**, *11*, 1061-1067.
80. Gorodetsky, M. L., et al. Optical microsphere resonators: optimal coupling to high-Q whispering-gallery modes. *J. Opt. Soc. Am. B* **1999**, *16*, 147-154.
81. Vollmer, F., et al. Protein detection by optical shift of a resonant microcavity. *Appl. Phys. Lett.* **2002**, *80*, 4057-4059.
82. Teraoka, I., et al. Perturbation approach to resonance shifts of whispering-gallery modes in a dielectric microsphere as a probe of a surrounding medium. *J. Opt. Soc. Am. B* **2003**, *20*, 1937-1946.
83. Vollmer, F., et al. Single virus detection from the reactive shift of a whispering-gallery mode. *Proc. Natl. Acad. Sci. U. S. A* **2008**, *105*, 20701-20704.
84. Huckabay, H. A., et al. Whispering gallery mode imaging for the multiplexed detection of biomarkers. *Sens. Actuators, B* **2011**, *160*, 1262-1267.
85. Washburn, A. L., et al. Quantitative, label-free detection of five protein biomarkers using multiplexed arrays of silicon photonic microring resonators. *Anal. Chem.* **2009**, *82*, 69-72.

Chapter 2

Whispering Gallery Mode Biosensors

Sensors that respond to refractive index changes due to surface binding events offer a flexible, sensitive and general detection platform that can be developed for disease biomarker screens. These platforms can enable high throughput and homogeneous detection schemes for proteins and nucleic acids without the use of labels. While many optical biosensors have been developed, optical resonator sensors based on whispering gallery mode (WGM) have shown considerable potential as platforms for clinical diagnostics.

2.1 Introduction to Whispering Gallery Modes

It has been known that sound waves spoken at a circular wall, like the dome of St. Paul's Cathedral, could travel long distances. This phenomenon termed, acoustic whispering gallery mode, were first described by Lord Rayleigh in the late 1800's.[1]

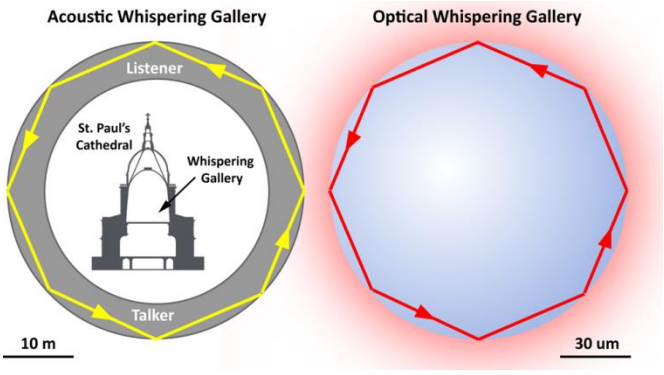

Figure 2.1. Acoustic whispering gallery mode shown on the left is an illustration of sound waves travelling along the circumference of a dome structure, such as the dome of St. Paul's Cathedral. The same phenomena are observed with light waves along the circumference of a dielectric material shown on the right.

In his 1912 publication titled "The problem of the whispering gallery", he characterized the sound intensity of these sound waves in a path along the gallery to discover nodes. Based on these findings he concluded that the circular structure of the gallery had the ability to contain sound waves through surface reflections allowing a whisper to travel long distances in a confined manner.[1] Likewise, light waves experience a similar phenomenon where small, circular dielectric structures confine light waves along their diameter as illustrated in **Figure 2.1**. These structures, tens of microns in diameter, can exhibit highly efficient recirculation of light via continuous total internal reflection. Concepts important to describe the working mechanism of WGM optical sensors are total internal reflection and the evanescent wave.

2.1.1 Total internal reflection and the evanescent wave

Light waves can be confined and recirculated within a whispering gallery mode structure and as a result, allow for longer interaction pathlengths between the light and the resonator surroundings. To understand this phenomenon, one must consider Snell's law which describes how light behaves when passing from one material to another:

$$n_1 sin\theta_1 = n_2 sin\theta_2 \qquad \text{Eq. 2.1}$$

where n_1 and n_2 are the refractive indices of the material ($n_1 > n_2$), θ_1 and θ_2 are the incident and refracted angles of the light beam measured from the normal of the interface. Snell's law describes that as light passes from a high index (n_1) to a low index (n_2) material, the refracted light waves will be bent away from the normal (θ_2) at angles greater than the incident angle (θ_1) with respect to their interface normal as illustrated in **Figure 2.2a**. As θ_1 is increased, there is a certain incident angle at which all of the

refracted light is contained at the boundary of the two mediums ($\theta_2 = 90°$). This angle is defined as the critical angle (θ_c):

$$\theta_c = sin^{-1}\left(\frac{n_2}{n_1}\right) \qquad \text{Eq. 2.2}$$

Any incident angle greater than this critical angle leads to the complete reflection at the interface, thus all of the light is reflected back into the same high index material. This condition is referred to as total internal reflection (TIR) and is illustrated by **Figure 2.2b**.

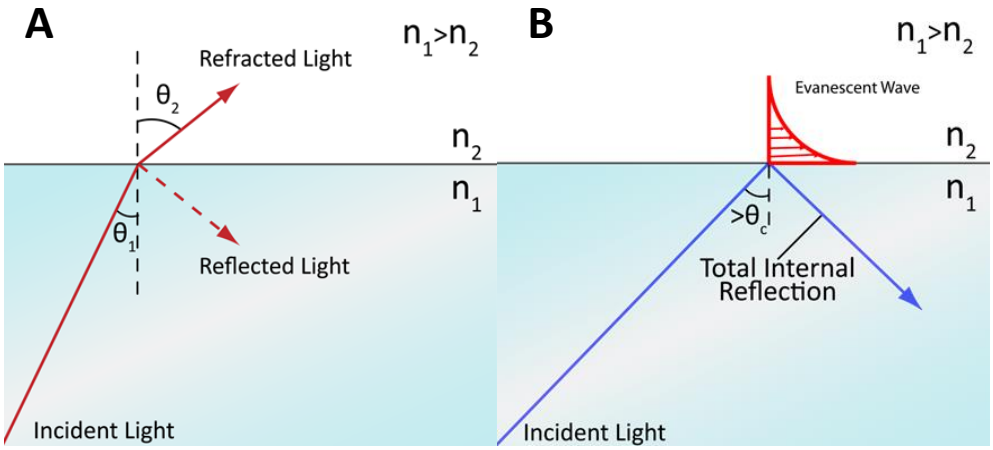

Figure 2.2. Total internal reflection and the creation of an evanescent wave.

Even though all of light is reflected back into the original medium under TIR, there exists a non-propagating, exponentially decaying evanescent wave that interacts with the neighboring medium up to 200 nm beyond the material boundary.[2] This phenomenon has been used extensively to excite molecules such as fluorophores located near the surface in fluorescence microscopy due to benefits such as background reduction and surface sensitivity.[3] Additionally, the evanescent wave has been exploited for sensing local refractive index changes. For biosensing applications, the evanescent wave

with limited propagation depth is advantageous for selectively detecting surface changes against the background signals in the bulk solution. This has allowed for the use of WGM as sensitive detectors for specific surface binding events with extraordinary detection limits.[4-6]

2.1.2 Whispering gallery mode resonance

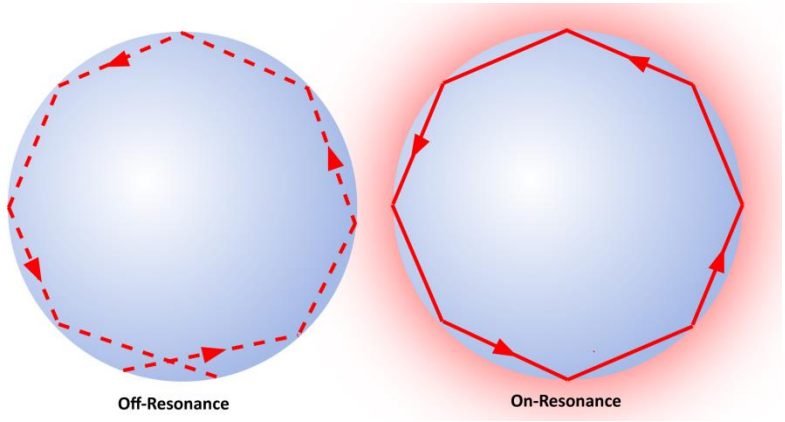

Figure 2.3. Dielectric structures can exhibit resonance when the conditions described in equation 2.3 are met. The left is an illustration of off-resonance when light does not interfere constructively. On the right, shows a resonance where constructive interference leads to the strong confinement of light.

Whispering gallery mode resonators take advantage of continuous total internal reflection leading to the confinement of light within its spherical structure. The light path along the circumference can have a resonance as shown schematically in **Figure 2.3.** A resonance light path occurs when the roundtrip distance within the structure is an integer multiple of the coupled wavelength. In this instance, the light coherently drives itself by returning in phase leading to constructive interference. Constructive interference allows the circulating intensity to grow until the rate at which light is coupled into the cavity is balanced by the rate at which it is lost. This condition is described as the WGM resonant condition which is given by:[2,7]

$$\lambda_r = \frac{2\pi r n_{eff}}{m} \qquad \text{Eq. 2.3}$$

where $\lambda_{r,}$ is the resonant wavelength, r is the radius, n_{eff} is the effective refractive index surrounding the sphere, and m is the integer multiple of the wavelength. Again, the build-up of an intense electromagnetic field due to the recirculation of light confined in these structures lead to sensitive interactions with the surrounding media useful for sensing. This is reflected in equation 2.3 where changes in the effective refractive index can be linearly related to the resonant wavelength. Thus, by tracking changes in the resonant wavelength of an optical resonator changes in the local refractive index can be measured. Furthermore, the interaction between the light and the resonator surrounds are multiplied leading to long effective pathlengths, due to efficient light recirculation leading to impressive detection limits and high sensitivities. This has generated great interest in utilizing WGM resonators as label-free sensors for biological applications.

2.1.3 Schematic for WGM Measurements

A common approach to measuring the resonant wavelength of a WGM resonator involves a thin optical fiber to evanescently couple light. Thinned optical fibers are prepared by removing the outer jacket and pulling the fiber down to approximately 3 μm in diameter. The fiber is positioned precisely near the resonator surface to efficiently tunnel light from the fiber into the resonator via frustrated total internal reflection. The output of the fiber is monitored using a photodetector as the tunable laser is scanned where a sharp dip in intensity is recorded as illustrated in **Figure 2.4.**

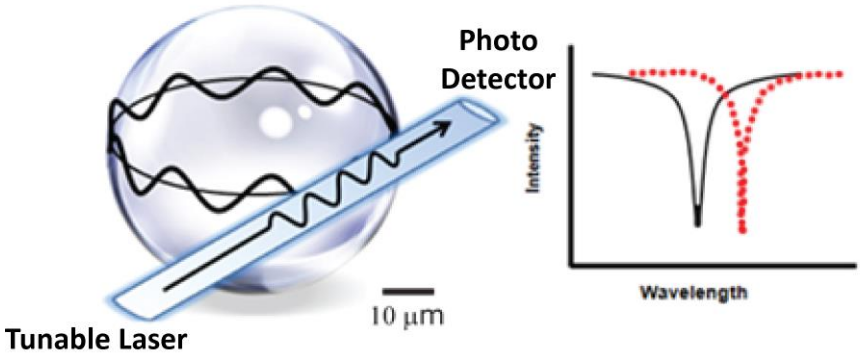

Figure 2.4. A typical WGM schematic where a fiber optic carrying light from a tunable source is brought near the surface of a spherical dielectric material. The output of the fiber optic is monitored while the wavelength is tuned. At a particular wavelength, light efficiently couples into the sphere leading to a dip in the transmission observed. This transmission dip shifts proportionally to the effective refractive index of the sphere's local environment.

The center of the intensity dip corresponds to the WGM resonant wavelength where light from the tunable laser is efficiently coupled into the resonator. Any changes in the effective refractive index near the resonator are observed as a proportional shift (shown in red), which is exploited in sensing applications. [6-12]

2.1.4 Whispering gallery mode for sensitive detection of biological interactions

As described in equation 2.3, WGM are utilized as sensors by measuring changes in the local refractive index. **Figure 2.5** illustrates how resonators can be implemented as biosensors by attaching biological recognition elements to their surface to specifically bind target analytes which change the n_{eff}. Binding events that occur on the resonator surface cause measurable changes of the resonant condition. Most biomolecules have a greater refractive index (n = ~1.5) than buffer solution (n = ~1.33) therefore measurements in solutions are easily achievable and have been extensively demonstrated.

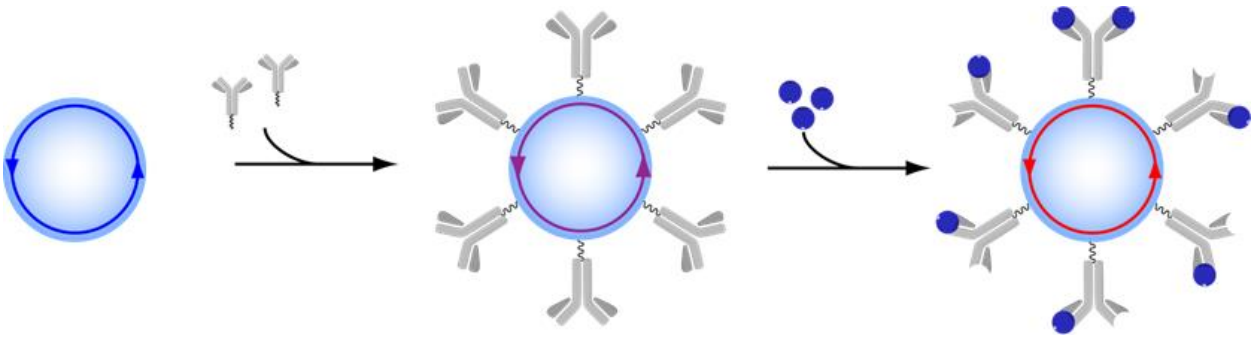

Figure 2.5. Schematic of a WGM biosensor. Biocapture material, such as antibody, is covalently attached to the surface of microspheres. Subsequent binding events between the antibody and antigen lead to changes in the local refractive index of the microsphere which can be monitoring by measuring its resonant wavelength.

The magnitude of the resonant wavelength shift due to binding of surface events has been modeled where the shift in resonant wavelength is described by:[4,13]

$$\frac{\Delta\lambda}{\lambda} = \frac{\alpha_{ex}\sigma_p}{\epsilon_0(n_s^2 - n_m^2)r} \qquad \text{Eq. 2.4}$$

In this equation, α_{ex} is the excess polarizability, σ_p is the surface coverage of target molecules, n_s and n_m are the refractive indices of the sphere and surrounding medium respectively, ε_0 is the vacuum permittivity and r is the radius of the sphere. The surface coverage and excess polarizability are directly related to the resonant shift. Furthermore, since the excess polarizability can be related to the molecular weight of the target molecule, resonant wavelength shifts can be used to quantitatively measure the number of analyte molecules and their bulk concentrations in solution.

In the process of validating WGM sensors for clinical diagnostics, it is important to understand fundamental properties that impact the sensor performance. It is therefore critical to discuss the factors that contribute to the WGM sensitivity and detection limits with respect to the physical interactions between light and the microresonator cavity.

2.2 Resonator performance relationship to sensor metrics

The recirculation of light due to the resonant condition allows for enhanced light-matter interaction resulting in improved sensitivities. Thus, the efficiency with which light is confined within a resonator does affect the overall sensor performance. Resonator performance with respect to light confinement efficiency and pathlength will be discussed in the following section. Furthermore, a theoretical discussion of the relationship between quality factor and limits of detection will be described.

2.2.1 Quality factor

While quality factor is a general term applicable to electrical and mechanical oscillator systems, here we will focus on quality factors as it pertains to optical systems. The resonator performance is highly dependent on its ability to confine light. Quality factor is a measure of how efficiently a resonator can store light within its structure.

One way to quantify the quality factor is to measure the instantaneous energy stored in the resonator by integrating the density of the electric and magnetic fields over the resonant light path. The steady-state energy balance is when the rate of energy lost from the cavity is equal to the rate of energy entering the cavity and can be related to the quality factor as shown here:[14,15]

$$Q = \omega_R \frac{W}{P_C} \qquad \text{Eq 2.5}$$

where ω_R is the resonant angular frequency, W is the total energy and P_c is the power coupled into the resonator. Higher total energy leads to higher quality factors which can be interpreted as higher field densities along the circumference of the structure leading to more interactions between the resonator

and its local surroundings. This definition is limited for quantitative assessment of quality factors as instantaneous energy measurements are difficult to make.

An alternative to quantify the quality factor of a resonator is to consider the rate of energy dissipation within a resonator structure. The quality factor can be related to the time required for light stored within a cavity to completely dissipate as described by:[14,15]

$$Q = \omega_R \tau_{RD} \qquad \text{Eq 2.6}$$

where ω_R is the resonant angular frequency and τ_{RD} is the cavity ringdown time. This equation states the longer energy dissipation times corresponds to higher quality factors or efficient light confinement. A more accessible method for determining quality factors uses linewidth measurements.

All quality factors reported here have been measured using the linewidth method. Quality factor can be empirically determined by the following equation:[14,15]

$$Q = \frac{\lambda_r}{\delta\lambda_r} \qquad \text{Eq 2.7}$$

where λ_r is the resonant wavelength, and $\delta\lambda_r$ is the full width at half maximum of the resonant wavelength intensity. This method provides a simple characterization where finer linewidths correspond to high quality factors useful for describing light confinement within a resonator. All three definitions of quality factors combined give a physical description of light being retained within a resonator. High quality factors lead to high energy densities, longer photon lifetimes within the structure and narrower linewidths as described by the above equations.

For sensing, high quality factors are desirable as they improve the interaction of the recirculated photons with the resonator surroundings, ultimately leading to higher sensitivities. Therefore, it is

advantageous to improve the quality factors to the highest possible value when developing a clinically relevant WGM biosensor.

Quality factors can be deconstructed into four categories of light loss mechanisms as shown by:[14]

$$\frac{1}{Q} = \frac{1}{Q_{rad}} + \frac{1}{Q_{mat}} + \frac{1}{Q_{scat}} + \frac{1}{Q_{ext}} \quad \text{Eq 2.8}$$

Here Q_{rad}^{-1} describes the radiative losses associated with bending losses from the spherical cavity. These losses are inversely related to the size of the resonator. As the resonator size decreases, the angles at which light approaches the interface become steep resulting in increased light loss. For resonators with diameters greater than 15λ, these losses are negligible. Q_{mat}^{-1} accounts for light losses within the material where light is confined. This loss can be described by the equation:[14]

$$Q_{mat} = \frac{2\pi n}{\lambda \alpha_{mat}} \quad \text{Eq 2.9}$$

where n is the refractive index, α_{mat} is the absorption decay constant and λ is the wavelength. High α_{mat} values can diminish the quality factor resulting in poorer resonator performance. However, using fused silica and a wavelength of 633 nm, quality factors are limited by Q_{mat}^{-1} to a theoretical maximum value of ~9×10^9. These values are more than sufficient for sensitive detection of biomolecular interactions as demonstrated in these publications. Q_{scat}^{-1} represents losses due to surface scattering losses on the resonator due to surface imperfections. These losses are minimized in resonators formed from melts where the high temperatures create exquisitely smooth surfaces. Lastly, Q_{ext}^{-1} describes loss contributions from surface contaminants present on the resonator which may act as light absorbing species. All of these contribute to the intrinsic Q-factor of a WGM resonator.

2.2.2 Improved light-sample Interaction

When light is recirculated within a resonator, the evanescent wave at the resonator surface is created by continuous total internal reflection interacts with the outside media. Efficient light recirculation or high Q factors therefore contribute directly to the degree to which the light and sample of interest interact. Equation 2.10 depicts this relationship:[14]

$$L_{eff} = \frac{Q\lambda}{2\pi n} \qquad \text{Eq 2.10}$$

where L_{eff} is the effective path length, n is the refractive index, λ is the wavelength and Q is the quality factor. This equation states that the path length dependency on quality factors can lead to overall interaction lengths on the order of centimeters to meters even though the physical sensor dimensions are microns in size. The small footprint of the sensor with enhanced light-sample interactions leads to a flexible detection platform promising low detection limit measurements. A more in depth discussion of the relationship between resonator performance and sensing metrics, however, will include Q factors, path length, mode volume, finesse and detection limits in the following sections.

2.2.3 Detection Limits

The quality factor of WGM resonators influences the minimum measurable shift in resonant wavelength. Recalling the linewidth method for the determination of quality factor, equation 2.7, the quality factor increases as the FWHM of the WGM resonance peak becomes narrower. Narrower spectral peaks also allow for the tracking of smaller changes in resonances as a response. Equation 2.11 represents the smallest measureable shift accounting for experimental noise and spectral bandwidth of the detection system:[2]

$$(\Delta\lambda_r)_{min} = \frac{\lambda_r * F}{Q} \qquad \text{Eq 2.11}$$

where λ_r is the resonant wavelength and *F* is a "measurement acuity factor" which includes experimental noise and spectral bandwidth contributions. When the limits of detection is determined in terms of the surface density of biomolecules the resulting equation is given by:[2,13]

$$\sigma_{LOD} = \frac{r(n_r^2 - n_m^2)F}{(\alpha_{ex}/\varepsilon_0)Q} \qquad \text{Eq 2.12}$$

where r is the radius of the resonator, α_{ex} is the excess polarizability of the biomolecule, ε_0 is the vacuum permittivity, and n_r and n_m are the refractive indices of the resonator and surrounding medium, respectively. This equation suggests that limits of detection are inversely proportional to the quality factor where higher quality factors lead to lower limits of detection. Additionally, the radius of the resonator must be decreased to obtain lower LODs. However smaller resonator sizes result in more radiative losses and thus lowers the quality factor. As a result, the size of the resonator must be optimized to the smallest size while minimizing radiative losses. Typical resonator diameters used for WGM biosensing range from 30 μm to 100 μm. Equation 2.12 for a resonator of 50 μm in diameter and a quality factor, achieved in experiments and by many other groups, of 4.5 x 10^6, the σ_{LOD} for the detection of bovine serum albumin (BSA) is calculated to be ~1.7 pg/mm^2 which is competitive with the best detection limits reported for SPR sensing, at ~1 pg/mm^2. We note here that quality factors up to 10^9 measured in the air have been reported in the literature.[16,17] However, most WGM resonators in solution exhibit quality factors up to 10^6. WGM biosensing demonstrates competitive limits of detection as a label-free, optical biosensor. For broader use of the technology in the clinic, environmental noise, detector cost and analytical performance must also be considered.

Consideration of experimental factors such as a data sampling, noise levels and data analysis methods can affect the relationship between quality factors and limits of detection. While previous

intuitive discussions where higher quality factors leading to lower detection limits hold true, these are often over simplified models. A more detailed experimental model was described by Silverstone et al. where a range of background noise signals using typical spectrometer and tunable laser sources were numerically modeled. The results of their studies proposed this relationship shown here:[18,19]

$$\Delta\lambda_{min}(3\sigma) = \frac{2.2*10^{-20}*\Delta f^{0.29}P^{0.65}}{SNR^{0.51}} \quad \text{Eq 2.13}$$

where Δf is the width of the resonant peak, P is the sampling rate and SNR is the signal to noise ratio. Silverstone et al. obtained this relationship by modeling signal to noise signals for heavily oversampled white noise within a 3σ level of certainty. Additionally, this equation is modeled using resonant wavelength peaks determined by Lorentzian curve fitting typical for WGM measurements. The equation suggests that when the quality factor, which is related to Δf, is improved by 3 orders of magnitude, the limits of detection is lowered by only a factor of 7.5.[18] These simulations suggest that improvements in quality factor as well as developing new data analysis and WGM peak determination methods must be made to develop biosensors with low detection limits. This will be discussed further in chapter 5 where a lock-in detector with WGM is described.

2.2.4 Sensitivity

The spectral sensitivity of a WGM sensor can be defined as:

$$S = \Delta\lambda/\Delta n \quad \text{Equation 2.14}$$

where Δλ is the shift of the sensor resonance in nm and Δn is the change in the refractive index. For biosensing, biomolecular events that occur on the surface of these resonators induce measurable changes in the refractive index. Here we will discuss the factors that affect WGM sensitivity. We have previously described quality factors in conceptual discussion, where higher quality factors lead to higher electric field densities. A crude but useful approximation assumes that all of the electric field related to sensing is contained in the surroundings of the resonator.

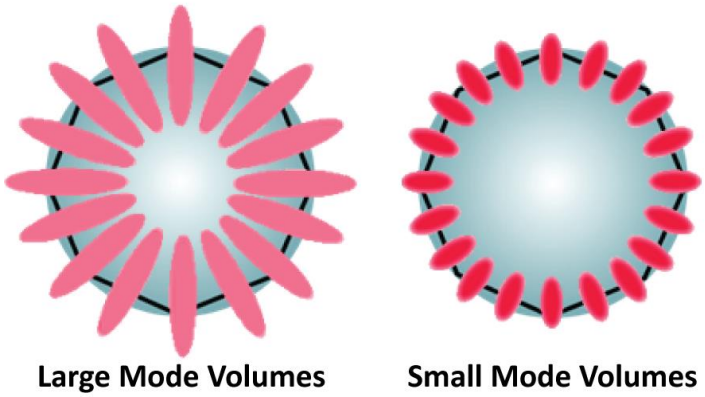

Figure 2.6. Illustration of large (left) and small (right) mode volumes for a spherical WGM resonator. Small mode volumes are advantageous for sensing due to the high concentrations of electric field at the sensing surface.

Mode volume describes the electric field density along the outer surface of the resonator.[20,21] A smaller mode volume is advantageous because this enhances the electromagnetic field strength or energy density on the sensing surface. A larger mode volume is related to lower energy densities leading to lower sensitivities. The comparison between larger mode volumes is made in **Figure 2.6** where larger mode volumes results in a more diffuse distribution of electric fields and thus weaker energy density. Smaller mode volumes have more concentrated electric fields in a smaller volume leading to higher energy densities. For sensing applications, small mode volumes are attractive to enable higher energy density interaction with the sensing surface. Mode volumes are related to the

wavelength of the excitation light where V ~ λ^3.[20-22] For the development of sensitive WGM detectors, shorter excitation wavelengths may lead to improved sensitivities.

2.2.5 Finesse

WGM biosensing performance can be summarized by a performance metric known as finesse (F). Finesse includes quality factors as well as mode volume to combine factors that contribute to the detection limit and sensitivity for WGM measurements. Finesse is proportional to the quality factor (Q) and inversely proportional to the mode volume (V):[21]

$$F \propto \frac{Q}{V} \qquad \text{Equation 2.14}$$

Resonators capable of achieving high finesse can lead to improved biosensor performance. Maximizing the Q-factor and minimizing the mode volume can result in highly sensitive WGM measurements useful for cancer diagnostics. Already there have been numerous demonstrations of WGM detectors measuring protein and nucleic acid surface binding with impressive metrics. These desirable characteristics have generated interest in the development of WGM sensing platforms. Decades of development has led to the optimization WGM resonator geometry and materials.

2.3 WGM resonator platforms for biosensing

Whispering gallery mode resonances can be supported in a variety of materials such as polymers, glass and diamonds. The greater the contrast in refractive index of the material and fluid solution of interest should result in less light lost leading to higher Q-factors. The absorption spectra of the material must also be considered with respect to the excitation wavelength as to minimize Q_{mat}^{-1}

losses.[14] The flexibility of the material choice that support WGM resonances can prove beneficial for commercialization where cost can inhibit the development of diagnostic tools. Fortunately, there are several geometries for WGM using inexpensive materials such as silicon wafer, silica microspheres and glass capillaries shown in **Figure 2.7**. The design attributes of each geometry are outlined in **Table 2.1** highlighting their advantages and disadvantages.

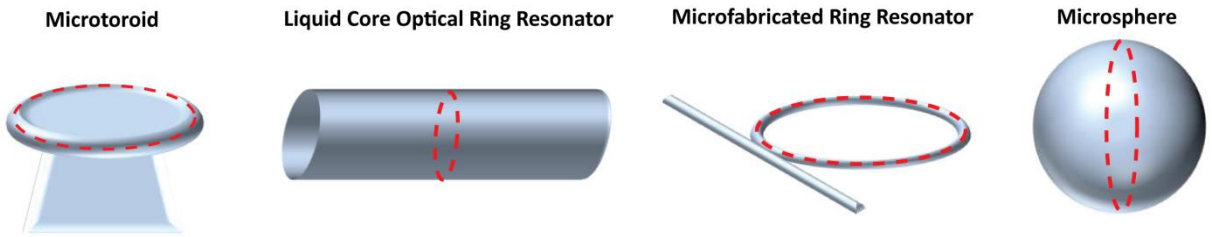

Figure 2.7. Illustration of WGM geometries employed for biosensing. The light path for each geometry is outlined in the red line.

Table 2.1. WGM geometries and their sensing metrics and platform integration

Optical Resonator Geometry	Detection Limits	Q-Factor	Multiplexing	Fluid Handling	Fabrication
Microtoroid[23,24]	10^{-7} RIU nM	$>10^{8}$	Difficult	Moderate	Complicated
Liquid Core Optical Ring Resonator[25-27]	$10^{-4} – 10^{-7}$ RIU nM – pM	10^{3} to 10^{6}	Difficult	Excellent	Complicated
Microfabricated Ring Resonator[11,28]	$10^{-4} – 10^{-6}$ RIU nM – pM	10^{3} to 10^{6}	Good	Good	Moderate
Microsphere[4,5,13]	10^{-7} RIU nM – pM	10^{5} to 10^{9}	Moderate	Poor	Easy

2.3.1 Microtoroid Resonators

Microtoroid structures are fabricated into a 3-D ring resonator designed to exhibit high Q-factors.[29] Fabrication of these resonators requires a combination of photolithography and wet etching. Silicon wafers with 2 μm thermal oxide layer is primed with a coating of photoresist then micropatterned with circles using a photomask. After washing away non-cross-reacted regions and

removing the oxide layer, a selective XeF_2 dry etch isotopically removes the silicon below the silica disks leaving microdisks above the substrate surface.[23,29] High quality factors are achieved in this geometry due to the 3-dimensional isolation of the resonator structure leading to low light loss. In this geometry, Q-factors greater than 10^8 have been measured leading to sensitive detection of biomolecules. Despite the high quality factors, drawbacks such as the difficulty of fabrication, fluidic implementation and light coupling alignment make this geometry difficult to develop for routine use in the clinic.

2.3.2 Liquid Core Optical Ring Resonator (LCORR)

Capillary ring resonators known as liquid core optical ring resonators (LCORR) provide a unique system where the resonator senses the fluidic located interior to the resonator. The physics of this detection scheme has been studied and modeled extensively.[30] The WGM resonance is excited along the outer circumference of the capillary using a tapered fiber optic. To enable the sensing of the fluid interior, the capillary wall is thinned to dimensions less than 4 μm via HF etching.[26,27] For biosensing applications the inner walls of the capillary are coated with a bioaffinity molecule. This platform demonstrates ease of fluidic integration using the capillary as both the resonator and fluid carrier. However, the fragile nature of thinned capillaries renders this platform difficult to adapt for clinical applications. Additionally, multiplexing is a challenge without the use of multiple capillaries each coated with different biomolecules. For a more robust platform, microfabricated ring resonators have been developed for multiplexed, on-chip immunoassays.

2.3.3 Microfabricated Ring Resonator

Microfabricated ring resonators are a WGM approach fabricated using common and scalable photolithography. Arrays of WGM supporting ring resonators can be fabricated on a silicon wafer. Additionally, waveguides are fabricated tangent to each ring resonator in this configuration resulting in a

robust light coupling method with no additional alignment required. This is an advantage as the distance between the resonator and the waveguide can be precisely optimized to maximize light coupling efficiency. Light is initially free spaced coupled into the waveguides either through a grating coupler or a focusing optic. The light is guided near ring resonators via waveguides to excite WGM resonances in these structures.[28] The ease of fabrication and on-chip design enables mass fabrication of these devices into a commercialized Maverick system from Genalyte.[31] Many resonators and their waveguides can be fabricated onto a single silicon wafer for the multiplexed detection of up to 32 analytes of interest as demonstrated by Genalyte.[32]

Despite the development of a commercial instrument using this robust, multiplexed, fluid-amenable platform, ring resonators exhibit lower Q-factors which is attributed to the rough surfaces inherent to photolithographic processes. As such their limits of detection tend to be lower compared to other geometries. Higher quality factors can be achieved using a microsphere based WGM resonator.

2.3.4 Microsphere Resonator

Microsphere resonators are commonly used as WGM resonators due to their low costs, ease of fabrication and optimal resonator performance. Microspheres can be formed on the end of fibers or capillaries using a straight forward melting method. Spheres formed from melts can range in size from several microns to 200 µm and can demonstrate high Q-factors up to 10^6-10^9.[33] This has enabled lower detection limits 10^{-7} RIU compared to microfabricated ring resonators (10^{-4} to 10^{-6} RIU). The impressive performance metrics of microsphere resonators combined with ease of fabrication and cost-efficiency has made this geometry a popular platform for WGM biosensing.

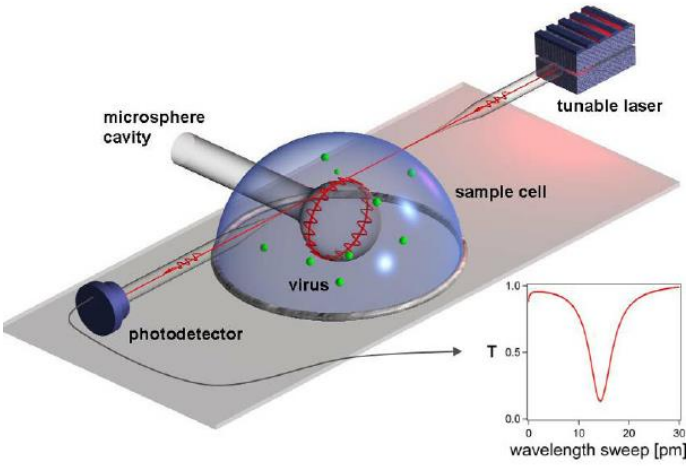

Figure 2.8. Microsphere cavity sensing of virus particles Adapted from Ref. 9. A thinned fiber optic carrying light from a tunable laser is brought near a microsphere in the sample cell. The output of the fiber is monitored using a photodetector to track the resonance as binding events occur on the sensor surface.[9]

The coupling of light into these spheres traditionally require a thinned fiber optic precisely aligned with the microsphere structure as shown in **Figure 2.8** adapted from Ref 6. The intensity of the fiber output is monitored by a photodetector. When the wavelength of the light is tuned a decrease in the transmission is observed. It is possible to measure the resonances of multiple spheres by simply placing more microspheres along the fiber. However, distinguishing shifts of multiple resonance spectra using a single transmission output is a challenge, thus, multiplexing is limited in this platform. Second, the integration of a fluidic system to these spherical detectors is a challenge as the thinned fiber is subject to movement during fluid exchanges required for a label-free biochemical assay. We believe that these drawbacks can be resolved through innovation to take full advantage of the impressive sensing metrics of spherical resonators.

2.4 Summary of spherical WGM innovations

Spherical WGM sensors offer high quality factors resulting in impressively low detection limits in biosensing. The microsphere platform for WGM biosensing present challenges for integration into a multiplexed system when traditional transmission based tracking of resonances is employed. In an effort to enable multiplexing with the desirable performance metrics inherent to spherical resonators, a WGM imaging (WGMi) was developed.[5,6] WGMi uses fluorescence imaging scheme which allows the simultaneous measurement of individual WGM resonances in a field of spheres as shown in **Figure 2.9**.

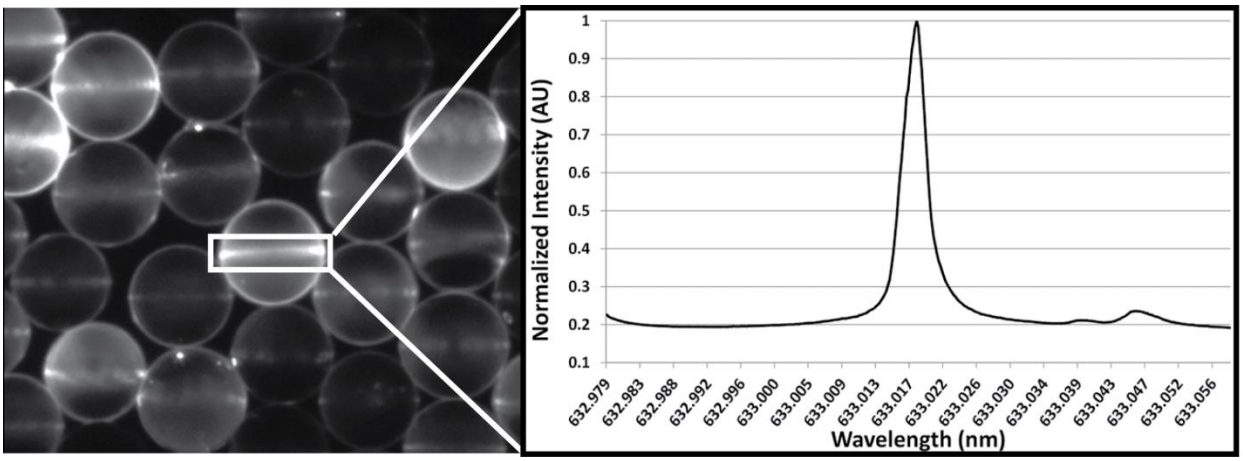

Figure 2.9. WGM imaging. The image (left) was obtained by a CCD camera. A field of fluorescent dye labeled microspheres is excited using a dove prism. A ring of enhanced fluorescence indicates a resonance which can be measured by monitoring the intensity of the region of interest (right).

A field of spheres is imaged using a CCD camera where fluorescent dye covalently attached to the resonator surface is excited exhibiting a ring of fluorescence upon resonance. Each resonance can be analyzed by extracting intensity information from the stacks of images collected. This WGMi approach has provided a new scheme for multiplexing using spherical WGM resonators.[6] Furthermore, WGMi been utilized to detect three putative markers of ovarian cancer simultaneously with negligible cross talk.[6]

Despite this advancement, spherical resonators have yet to be easily incorporated into fluidic platforms. The compatibility of these detectors with fluid exchanges critical for any bioassay must be improved to translate this technology for routine diagnostics. The projects outlined in the following chapters present solutions to these limitations in hopes of developing a clinical viable cancer diagnostic platform.

2.5 References

1. Rayleigh, L. CXII. The problem of the whispering gallery. *The London, Edinburgh, and Dublin Philosophical Magazine and Journal of Science* **1910**, *20*, 1001-1004.
2. Vollmer, F., et al. Whispering-gallery-mode biosensing: label-free detection down to single molecules. *Nat. Methods* **2008**, *5*, 591-596.
3. Axelrod, D., et al. Total internal reflection fluorescence. *Annual review of biophysics and bioengineering* **1984**, *13*, 247-268.
4. Arnold, S., et al. Shift of whispering-gallery modes in microspheres by protein adsorption. *Opt. Lett.* **2003**, *28*, 272-274.
5. Huckabay, H. A., et al. Whispering gallery mode imaging for the multiplexed detection of biomarkers. *Sens. Actuators, B* **2011**, *160*, 1262-1267.
6. Huckabay, H. A., et al. Label-free detection of ovarian cancer biomarkers using whispering gallery mode imaging. *Biosens. Bioelectron.* **2013**, *45*, 223-229.
7. Vollmer, F., et al. Protein detection by optical shift of a resonant microcavity. *Appl. Phys. Lett.* **2002**, *80*, 4057-4059.
8. Vollmer, F., et al. Multiplexed DNA quantification by spectroscopic shift of two microsphere cavities. *Biophys. J.* **2003**, *85*, 1974-1979.
9. Vollmer, F., et al. Single virus detection from the reactive shift of a whispering-gallery mode. *Proc. Natl. Acad. Sci. U. S. A* **2008**, *105*, 20701-20704.
10. Vollmer, F., et al. Label-free detection with high-Q microcavities: a review of biosensing mechanisms for integrated devices. *Nanophotonics* **2012**, *1*, 267.
11. Washburn, A. L., et al. Quantitative, label-free detection of five protein biomarkers using multiplexed arrays of silicon photonic microring resonators. *Anal. Chem.* **2009**, *82*, 69-72.
12. Kim, D. C., et al. Integration of microsphere resonators with bioassay fluidics for whispering gallery mode imaging. *Analyst* **2013**, *138*, 3189-3195.
13. Soria, S., et al. Optical microspherical resonators for biomedical sensing. *Sensors* **2011**, *11*, 785-805.
14. Gorodetsky, M. L., et al. Optical microsphere resonators: optimal coupling to high-Q whispering-gallery modes. *J. Opt. Soc. Am. B* **1999**, *16*, 147-154.
15. Chiasera, A., et al. Spherical whispering-gallery-mode microresonators. *Laser Photonics Rev.* **2010**, *4*, 457-482.
16. Hoa, X., et al. Towards integrated and sensitive surface plasmon resonance biosensors: a review of recent progress. *Biosensors & bioelectronics* **2007**, *23*, 151-160.

17. Fan, X., et al. Sensitive optical biosensors for unlabeled targets: A review. *Anal Chim Acta* **2008**, *620*, 8-26.
18. Meldrum, A., et al. Capillary-type microfluidic sensors based on optical whispering gallery mode resonances. *Reviews in Nanoscience and Nanotechnology* **2014**, *3*, 193-209.
19. Silverstone, J., et al. Ultimate resolution for refractometric sensing with whispering gallery mode microcavities. *Optics express* **2012**, *20*, 8284-8295.
20. Ilchenko, V. S., et al. Optical resonators with whispering-gallery modes-part II: applications. *IEEE Journal of Selected Topics in Quantum Electronics* **2006**, *12*, 15-32.
21. Kippenberg, T. J. A. *Nonlinear optics in ultra-high-Q whispering-gallery optical microcavities*. California Institute of Technology2004.
22. Yoshie, T., et al. Optical microcavity: Sensing down to single molecules and atoms. *Sensors* **2011**, *11*, 1972-1991.
23. Vahala, K. J. Optical microcavities. *Nature* **2003**, *424*, 839-846.
24. Ozgur, E., et al. Label-Free Biosensing with High Selectivity in Complex Media using Microtoroidal Optical Resonators. *Scientific reports* **2015**, *5*.
25. Zhu, H., et al. Integrated Refractive Index Optical Ring Resonator Detector for Capillary Electrophoresis. *Anal. Chem.* **2007**, *79*, 930-937.
26. Zhu, H., et al. Opto-fluidic micro-ring resonator for sensitive label-free viral detection. *Analyst* **2008**, *133*, 356-360.
27. Suter, J. D., et al. In *Engineering in Medicine and Biology Society, 2009. EMBC 2009. Annual International Conference of the IEEE*; IEEE, 2009, pp 1042-1044.
28. Washburn, A. L., et al. Label-free quantitation of a cancer biomarker in complex media using silicon photonic microring resonators. *Anal. Chem.* **2009**, *81*, 9499-9506.
29. Zhang, X., et al. Silica microtoroid resonator sensor with monolithically integrated waveguides. *Optics express* **2013**, *21*, 23592-23603.
30. White, I. M., et al. Liquid-core optical ring-resonator sensors. *Optics Letters* **2006**, *31*, 1319-1321.
31. Luchansky, M. S., et al. High-Q optical sensors for chemical and biological analysis. *Analytical Chemistry* **2011**, *84*, 793-821.
32. Graybill, R. M., et al. Emerging Biosensing Approaches for microRNA Analysis. *Analytical Chemistry* **2015**.
33. Foreman, M. R., et al. Whispering gallery mode sensors. *Advances in Optics and Photonics* **2015**, *7*, 168-240.

Chapter 3

Fluidics compatible WGM Platform

3.1 Introduction

Whispering gallery mode biosensing platforms are predominantly built around either high index glass microsphere resonators or microfabricated planar ring resonators.[1-3] The former uses commercially available or easily fabricated microspheres while the latter is produced on-chip using standard microfabrication techniques. Microfabricated planar ring resonators have demonstrated multiplexing capabilities and are easily incorporated with the fluidics necessary for sample handling and delivery.[4] Microsphere resonators, on the other hand, have historically suffered by comparison in these metrics but offer superior optical characteristics. Microspheres are formed from melts which yield exquisitely smooth surfaces, leading to Q-factors which can be orders of magnitude larger than other resonator designs.[2] Large Q-factors translate into long effective path lengths which improves the sensitivity and limits of detection, both of which are obviously desirable in sensing applications. Moreover, microspheres are inexpensive, commercially available, and are offered in a range of sizes and materials.

For sensing it is highly desirable to combine the multiplexing and fluidics capabilities of microring resonators with the optical properties of microsphere resonators. Recently, we reported a fluorescence imaging approach that enables the WGM resonances from each microsphere in a field of resonators to be simultaneously measured. This enables large scale multiplexing which removes one of the barriers listed above when using microspheres in sensing applications.

3.1.1 Summary of initial work

WGM imaging was introduced as a novel way to track the individual resonances from numerous spheres in a single measurement.[5,6] In this approach, light is simultaneously coupled into a large number of microspheres using the evanescent field created from total internal reflectance in a Dove prism. Each microsphere is labeled with the same fluorescent dye, which acts as marker signaling when a particular resonator comes into resonance. As the excitation wavelength from a tunable diode laser is scanned, a ring of enhanced fluorescence is observed around a microsphere when a WGM resonance is reached. This enables the WGM resonance from each sphere in a large field of view to be simultaneously measured using fluorescence imaging.[5,6] For the detection of several biomarkers in a multiplexed assay, each sphere size was functionalized with a different antibody enabling a visual indication of the identity of biomolecule. Huckabay et al. demonstrated the use of spherical resonators to detect the binding of prolactin, CA-125 and osteopotin in a multiplexed assay.[6] Here, we discuss the development of a method that stabilizes microspheres to a substrate without losses in quality factor, to address the challenge of fluidic implementation to spherical WGM detection platforms.

3.1.2 Challenges of Fluidics for Spherical WGM sensing

While WGM imaging enables easily multiplexed WGM detection, developing a sensing platform amenable to fluidic exchanges remains a challenge. Typical biosensing assays require multiple fluid exchanges or mixing steps which can perturb spheres resting on a substrate through gravity alone. This creates problems since the resonant wavelength of a resonator is linked to the axis around which the WGM resonates. Any change in the WGM path around the sphere due to reorientations on the substrate, therefore, can shift the resonant wavelength and nullify an assay.

Immobilizing microsphere resonators on a substrate, however, presents challenges for WGM sensing since the circumference of the sphere supporting the resonance must remain pristine. This

precludes embedding the spheres in adhesives or other films that would disrupt the coupling of light around the sphere. One can envision loading spheres into microfabricated arrays of wells to hold them in place, but this turns out to be problematic in practice. First, the poor monodispersity of spheres complicates matching well size with sphere dimensions for stable immobilization. The larger issue, however, arises from complications associated with efficiently coupling light into the immobilized spheres. It is very difficult to load arrays with spheres such that they are both tightly held and in good contact with the substrate, which is necessary for efficient coupling of light into the resonator through evanescent field excitation.

3.1.3 Approach and application

In this chapter, we discuss a method for immobilizing microsphere resonators on glass substrates adapted from a calcium-assisted glass-to-glass bonding method. The latter was initially developed for microfluidic glass chip fabrication.[7] The method creates a stable contact between the high index glass microsphere resonators and a glass substrate, enabling efficient coupling of light into the immobilized microspheres. Measurement of resonator Q-factors confirms that the immobilization method does not degrade the WGM resonance or greatly perturb the interface between the sphere and the substrate. To demonstrate the robustness of the immobilized microresonators, lipid bilayers were transferred onto the substrate bound microspheres using a combination of the Langmuir-Blodgett (LB) and Langmuir Schaeffer (LS) techniques. Bilayers of the lipid DOPC doped with 5 mol% ganglioside GM1 were formed using this sequential transfer method where each leaflet was transferred at 25 mN/m. GM1 binds cholera toxin, the oligomeric protein secreted by *Vibrio cholera* which causes the dehabilitating diarrhea associated with cholera.[8] Here we demonstrate the sensing capabilities of the bilayer draped over immobilized microspheres by tracking changes in their WGM resonant wavelength upon the addition of cholera toxin. Analysis of the resulting binding curves yields a measured K_d of 1.5 x

10^{-11}, consistent with literature values, and a detection limit of 3.3 pM.[9,10] The reported bonding scheme, therefore, is shown not to perturb the optical properties of the resonators while immobilizing them sufficiently onto the substrate for assay development and implementation. The novel coupling of Langmuir-Blodgett films with WGM resonators also enable the characterization of quality factor losses due to dye concentration important for WGM imaging development.

3.1.4 Effect of resonance reporting dye on quality factors

As previously discussed, WGM imaging requires the incorporation of dye molecules to the resonator surface to exhibit a ring of enhanced fluorescence upon resonance. The addition of a dye to the WGM sensing surface, however, may have adverse effects on the optical properties of the resonator. First, steric competition between dye molecules and antibody molecules on the sensor surface may reduce the number of available antigen binding sites reducing sensitivity, decreasing dynamic range and increasing limits of detection. Secondly, WGM sensor performance is related to the efficiency with which light is recirculate around the resonator. Thus, any mechanism leading to light loss from the resonator can result in lower quality factor and sensitivity.[11] Characterization of changes in the quality factor with dye concentration can reveal an optimized detection platform using WGM imaging. Controlling dye concentrations is difficult using surface functionalization. However, LB films enable excellent compositional control of dye within lipid monolayers useful for this dye loading study. Here, LB films containing a range of 0.25 to 10 mol% TR-DHPE dye as a model to study dye loading effects on the quality factors of WGM resonators.

3.2 Materials and Methods

3.2.1 Microsphere Immobilization

High refractive index (n = 1.9), barium titanate ($BaTiO_3$) glass microspheres (45 μm ± 7% diameter, Mo-Sci, Rolla, MO) were cleaned in a 5% Contrad solution. The spheres were rinsed in an ethanol/water (30/70 v/v) solution and stored in absolute ethanol. Spheres were exchanged into an aqueous PBS solution prior to use. A glass bonding solution was prepared with 0.125% w/v calcium acetate (Fisher Scientific, Hampton, NH) and 0.125% w/v powdered detergent (Alconox Inc., White Plains, NY) in nanopure H_2O. Approximately 100 uL of the bonding solution was placed on a clean glass cover slip (Fisher Scientific, Pittsburg, PA) and allowed to deprotonate the glass surface for ~5 minutes. Approximately 5 μL of the clean microspheres in PBS solution were transferred to the sample slide and allowed to dry for 20 minutes at 50°C. The sample slide was washed thoroughly with nanopure H_2O to remove any unbound spheres and excess salts from the surface prior to monolayer transfer.

3.2.2 Langmuir-Blodgett trough transfer of lipids

Dioleoylphosphatidylcholine (DOPC) and ganglioside GM1 (GM1) were obtained at >99% purity (Avanti Polar Lipids, Alabaster, AL) and used without further purification. The fluorescent lipid probe, Texas-Red dihexadecanoyl-sn-glycero-3-phosphoethanolamine (TR-DHPE) (Life Technologies, Carlsbad, CA), was diluted in methanol to obtain appropriate working concentrations. DOPC/GM1 (95:5 mol%) solutions were prepared at 1 mg/mL concentrations in a 65:35 volume mixture of chloroform and methanol. Lipid mixtures prepared for WGM assays were further doped with 0.25 mol% TR-DHPE to enable WGM fluorescence imaging. Approximately 50 μL of the appropriate lipid solution was dispersed on a 18MΩ water subphase in a Langmuir-Blodgett trough (Type 611, Nima Technology, Coventry, England). The solvent was allowed to evaporate for at least 15 min prior to initiating

compression/expansion cycles to anneal the film. Each monolayer was subjected to two compression/expansion cycles between surface pressures of 10 mN/m and 40 mN/m with the barrier rate held constant at 100 cm^2/min. Following the last expansion, the monolayers were compressed to 25 mN/m and held for ~10 min prior to transfer onto the substrate. Bilayers were transferred on to the immobilized glass microspheres at dipping velocity of 1 mm/min by the Langmuir-Blodgett/Langmuir-Schaeffer method resulting Y-type bilayers. All bilayers were transferred and imaged at 22°C.

3.2.3 Assay Preparation

Prepared glass cover slips were fit into the custom flow cell. Refractive index matching fluid (n=1.514 immersion oil, Olympus, Center Valley, PA) was used between the prism surface and sample slide. A syringe pump (Harvard apparatus, Holliston, MA) was used to fill the flow cell chamber with a PBS solution (MP Biomedicals, Solon, OH). A second syringe pump and fluidic controller (Warner Instrument Corp., Hamden, CT) was used to inject aliquots of purified recombinant cholera toxin beta labeled with A555 (CTxB-A555) (Molecular Probes, Eugene, OR) into the flow chamber. Each injection was allowed in incubate in the flow chamber for 5 minutes before being flushed with PBS and imaged.

3.2.4 TIR fluorescence imaging

Fluorescence imaging assays of cholera toxin binding to supported bilayers of DOPC/GM1 utilized CTxB-A555 (Molecular Probes). Binding of the CTxB-A555 to the lipid bilayer was imaged with an inverted microscope (Olympus IX71) equipped with a 60x PlanAPO objective (1.45 NA, Olympus). The 514 nm line from an argon ion laser (Innova 90, Coherent Inc., Santa Clara, CA) was coupled into the microscope through the objective using a total internal reflection illumination configuration. Emission from the bound CTxB-A555 was collected with the same objective, filtered to remove the excitation light

(Chroma), and imaged onto a cooled CCD (Coolsnap K4). Image collection was controlled with Slidebook software (Intelligent Imaging Innovations).

3.2.5 Fluorescence WGM imaging

The tunable output from a Vortex II TLB-6900 external cavity diode laser (New Focus, Santa Clara, CA) was directed into a N-BK7 Dove prism (n = 1.52, Edmund Optics, Barrington, NJ), on which the sample was mounted. Total internal reflection at the substrate interface creates an evanescent field, which was used to launch light into the immobilized microspheres. At a WGM resonance, an enhanced ring of fluorescence from TR-DHPE doped into the LB films and layered onto the microspheres was imaged from above. The fluorescence was collected through a 10X UMPlanFL (0.3 NA) objective (Olympus, Center Valley, PA), filtered to remove the residual excitation (Chroma, Bellows Falls, VT), and imaged onto a cooled CCD camera (Coolsnap K4, Roper Scientific, Tuscon, AZ). A LabView program controlled scanning of the laser system, which was synchronized with Slidebook image collection software (Intelligent Imaging Innovations, Denver, CO).

3.2.6 Dye study for quality factor characterization

Monolayers were transferred onto microscope slides with immobilized WGM resonators using the same procedures outlined previously. DOPC lipids were doped with TR-DHPE at increasing concentrations of 0.25, 0.5, 0.75, 1, 5 and 10 mol%. Approximately 50 μL of the lipid solution was dispersed on a 18 MΩ water subphase in a Langmuir-Blodgett trough. The solvent was allowed to evaporate for at least 15 min prior to initiating compression/expansion cycles to anneal the film. The monolayers were compressed to 25 mM/m then subsequently transferred on to the immobilized glass microspheres at a substrate velocity of 1 mm/min. The quality factors of at least 20 WGM resonators at each condition were measured to provide sufficient statistics.

3.3 Results and Discussion

3.3.1 Optimization of sphere bonding

Allen et al. demonstrated robust glass to glass surface bonding using a 0.5% Alconox/0.5% calcium acetate slurry.[7] WGM resonator immobilization on glass substrates using this method produced rigidly bonded spheres, however, the substrate had residue on the resonator surface which adversely affected the quality factors of these resonators. Alconox and calcium acetate concentrations were adjusted adapting the method developed by Allen et al.[7] to obtain residue-free resonator surfaces. We systematically lowered the calcium acetate solution (0.25%, 0.125% and 0.0625% w/w) while maintain the Alconox concentration (0.5% w/w). Less salt residue was observed, as expected, however, the sphere adhesion to the surface was noticeably impaired. This is not clearly understood but we suspect that since Alconox is anionic, higher concentrations may compete against the silanol groups on the glass surfaces and disrupt the calcium to surface silanol interaction. Thus, we lowered the concentration of Alconox and calcium acetate simultaneously. We discovered that 0.125% w/w of Alconox and 0.125% w/w of calcium acetate produced sufficiently bonded spheres with minimal residual salts leading to improved quality factors. We intend to use this method for resonators with antibodies attached on their surfaces for WGM immunoassays, thus, we wanted to reduce incubation temperatures and time to minimize the potential of antibody denaturation.

The reported method requires 2 hr incubation at 115°C to form a tight bond between two glass slabs. It was speculated that this is needed to fully remove moisture that may be trapped between the two surfaces. Our sphere and substrate interface has less trapped moisture compared to two flat glass slabs**,** thus, milder temperatures can be utilized to remove moisture. Both time and temperatures were minimized according to **Table 3.1**.

Temperature	Incubation Time	Sphere immobilization
90°C	1 hr, 40 mins, 20 mins	Good at all incubation times
70°C	1 hr, 40 mins, 20 mins	Good at all incubation times
50°C	1 hr, 40 mins, 20 mins	Good at all incubation times
22°C (RT)	1 hr, 40 mins, 20 mins	Mild at 1 hr, no bonding at 40 and 20 mins

At incubation times of 20 mins at 50°C had sufficient bonding efficacy of the resonator to the substrate. Room temperature bonding at 1 hour may prove more useful for protein integrated WGM resonators to lessen the potential for thermal degradation.

Using these optimized conditions, high index barium titanate ($BaTiO_3$) microspheres were bonded to glass substrates using the steps outlined schematically in **Figure 3.1**. A glass substrate was first rubbed with a slurry of basic detergent (Alconox) containing 8.0 mM Ca^{2+}. The spheres were then deposited on the glass substrate and incubated at 50^{o}C for approximately 20 minutes until dry. The spheres, now bonded to the substrate, were incubated in 18 MΩ water overnight to remove the residual salts and unbound spheres from the substrate surface.

3.3.2 Proposed mechanism for glass-glass bonding

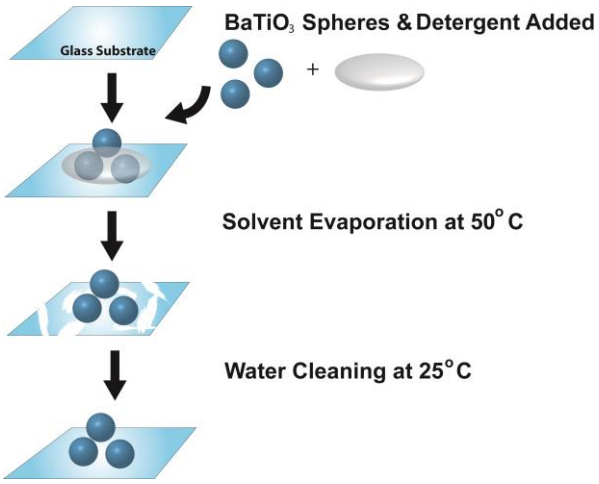

Figure 3.1. Schematic of the calcium-assisted procedure for immobilizing WGM microsphere resonators to a glass substrate. A drop containing 0.125% (v/v) Alconox and 0.125% (v/v) calcium acetate solution is placed along with a cluster of microspheres onto a clean glass substrate. The sample is then placed in a 50°C oven for 20 minutes. Evaporation of the solvent leaves a salt residue which is removed by bathing in deionized water overnight at room temperature, leaving a clean glass substrate with microspheres bound to the surface.

Conceptually, one can envision the divalent calcium ion acting as a bridge between the negatively charged surface groups on the microspheres and substrate, thus leading to stable bond formation.[7] However, as the original report showed, a more complicated mechanism is almost certainly needed since other divalent cations do not lead to bond formation. Regardless of the mechanism, this approach does successfully immobilize $BaTiO_3$ spheres on the glass substrate. The bonding scheme outlined in **Figure 3.1** uses a lower temperature, which was found in the original study to lead to reversible bond formation. However, as will be shown, this gentler bonding method is more than sufficient to immobilize spheres for the assay employed in this report. Additionally, this immobilization scheme can be used to adhere dye functionalized spheres without loss of dye function. This is important for the WGM imaging approach which uses fluorescence to detect sphere resonances.

3.3.3 Fabrication of lipid films on WGM resonators

Another advantage of the microsphere bonding scheme results from the flexibility inherent in this approach when designing assays. Immobilizing microsphere resonators onto a substrate opens new opportunities for functionalizing the resonators using techniques that are not compatible for use with free spheres. For example, Langmuir-Blodgett (LB) and related techniques offer extraordinary capabilities for creating highly ordered films on substrate surfaces.[12-14] These techniques provide exquisite layer-by-layer control over film properties such as composition, packing, and constituent orientation which has generated interest in using this control to tailor assay properties.[12,13] As illustrated in **Figure 3.2**, the LB method involves the transfer of films from an air-water interface onto a substrate surface using a dipping method.

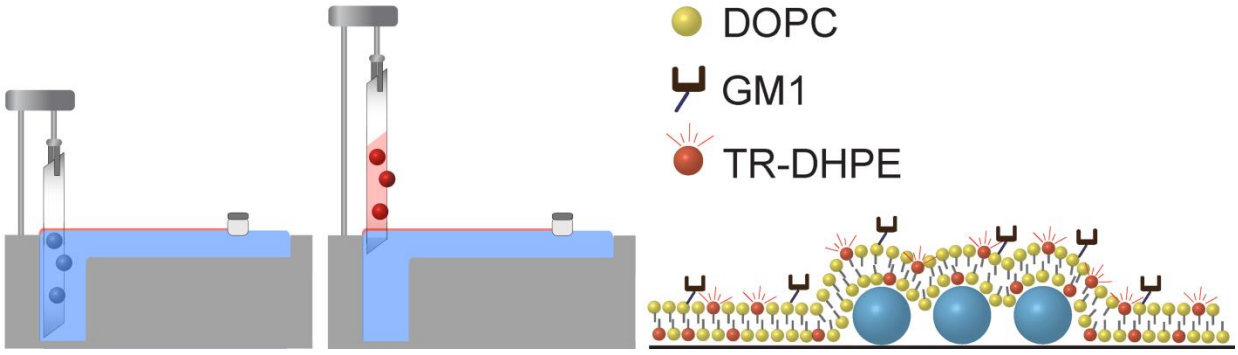

Figure 3.2. Schematic of the Langmuir-Blodgett trough used to transfer lipid films onto a substrate. A 50 uL aliquot of the lipid solution is dispersed on the water subphase and a moving barrier compresses the film to the desired surface pressure. A glass substrate with bonded microspheres is slowly pulled through the air-water interface, transferring a lipid monolayer onto the substrate surface. For these experiments, a second monolayer is transferred onto the first using the Langmuir-Schaffer technique, creating a bilayer as shown schematically in the right panel.

As suggested in **Figure 3.2**, here we show that the bonded spheres are sufficiently immobilized to withstand LB film transfer, thus creating new opportunities for assay development using microsphere resonators.

3.3.4 WGM resonance characterization of immobilized spheres

To confirm that the immobilization procedure does not interfere with or degrade WGM resonances of the microspheres, fluorescence imaging experiments were first performed using LB films doped with a fluorescent marker. For these experiments, immobilized microspheres were coated with a DOPC bilayer containing 0.25 mol% TR-DHPE, transferred using the LB/LS method. The fluorescent lipid analog, TR-DHPE, was added to act as a fluorescent reporter of the WGM resonances. The immobilized spheres were mounted on a Dove prism, as shown in **Figure 3.3**, where light from a tunable diode laser experiences total internal reflection at the sample interface. As the wavelength of the diode laser was scanned, the associated evanescent field launches light into the immobilized spheres. WGM resonances are detected as an enhanced ring of fluorescence around the particular microsphere resonator, which is detected from above using fluorescence imaging. The fluorescence was collected and imaged onto a CCD camera as shown in **Figure 3.3**.

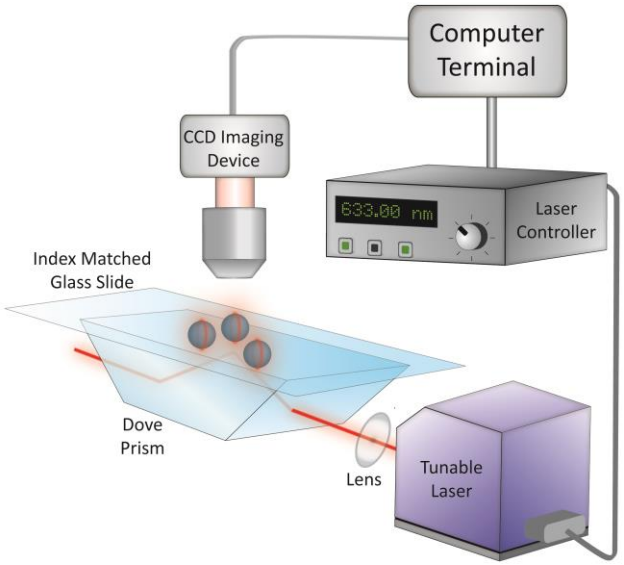

Figure 3.3. Schematic of the instrumentation used for the fluorescence imaging of WGM resonances. Light from a tunable diode laser is directed through a Dove prism, which creates an evanescent field at the substrate interface. The evanescent field couples light into the immobilized microspheres and WGM resonances are detected through fluorescence imaging of a dye marker located on their surface. As the excitation wavelength is tuned, an enhanced ring of fluorescence is observed around the spheres as a WGM resonance is reached. The fluorescence is collected and imaged onto a CCD camera.

Figure 3.4 shows a typical series of fluorescence images taken on the same field of microspheres as the excitation wavelength from the tunable diode laser is scanned. These spheres have been immobilized onto the substrate surface using the scheme in **Figure 3.1** and exhibit bright fluorescence rings indicative of WGM resonances. The excitation spectrum for each resonator can be extracted from a series of fluorescence images collected as a function of excitation wavelength. A typical excitation spectrum is shown in **Figure 3.4**. The Q-factor calculated from this spectrum is 1.0 x 10^5 which is comparable to measured Q-factors for spheres resting on substrates through gravity alone. This demonstrates that the immobilization process has little effect on the quality of the WGM resonance.

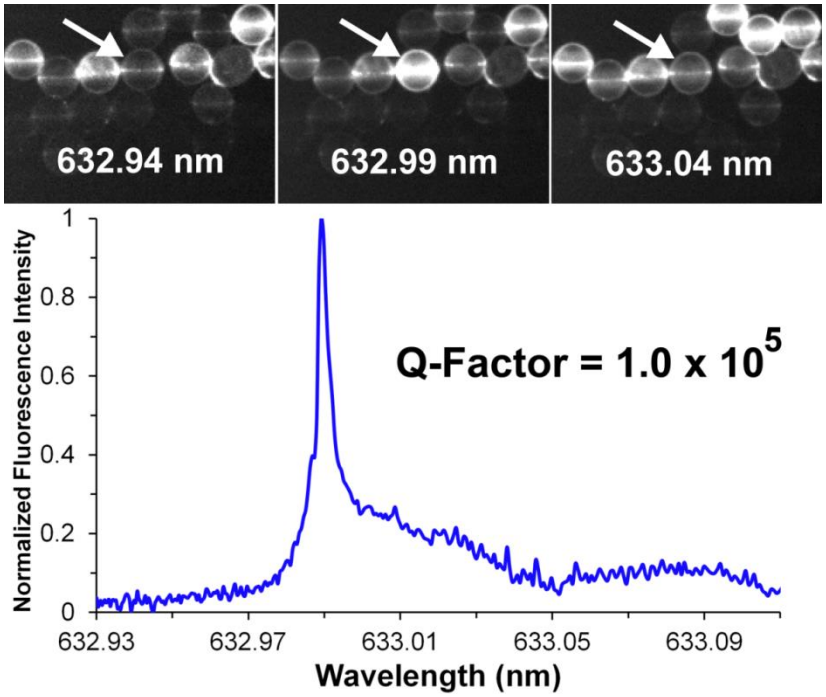

Figure 3.4. (top) Representative fluorescence images of 45 µm spheres extracted from a series of images taken as the wavelength of the diode laser is scanned between 632.93 nm and 633.10 nm. The arrow denotes a sphere that undergoes a large change in fluorescence, indicating a WGM resonance near 632.99 nm. (bottom) Excitation spectrum of the WGM resonance for the indicated sphere, extracted from the series of fluorescence images by integrating the emission from the sphere in each image.

3.3.5 Testing of fluidic system with WGM resonators

Having shown that the immobilization procedure does not degrade resonator optical properties, the utility of membrane coated microspheres for bioassay development was explored. Bioassays require rapid fluid exchanges and the immobilized resonators need to maintain both close contact with the substrate surface and not reorient during these processes. To test the stability of the immobilized microspheres during rapid fluid exchanges, the flow cell in **Figure 3.5** was fabricated.

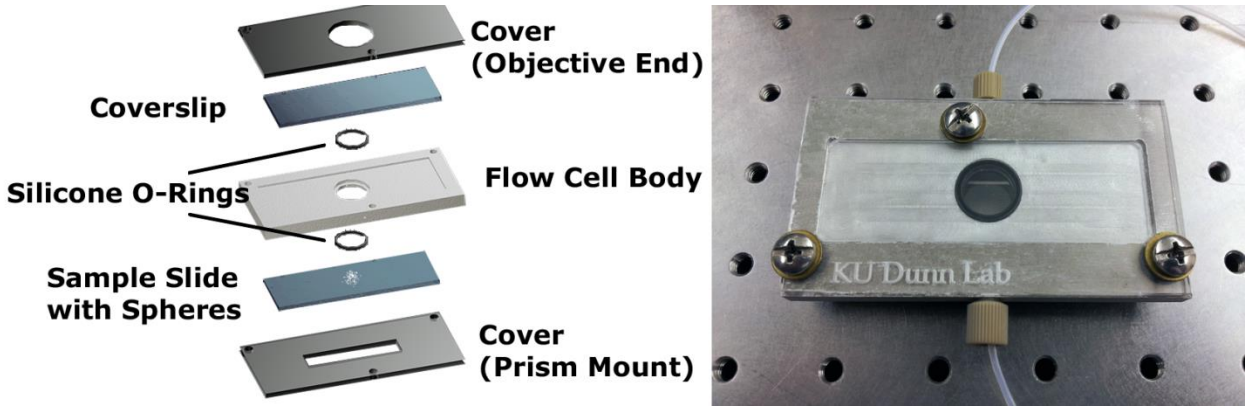

Figure 3.5. (left) Schematic of the flow cell used for fluidic exchange and WGM imaging. The bottom cover accepts the Dove prism used to launch light into the small resonators which are imaged from above through the transparent window. An image of the flow cell is shown on the right.

The glass substrate supporting the immobilized microspheres rests on a rigid bottom plate that is notched to accept the Dove prism. An aluminum flow cell body that contains the solution inlet and outlet ports is sandwiched between the sample substrate and top coverslip using two silicone o-rings to form a water tight seal. The thickness of the flow cell body dictates the dead volume of the cell which is 500 uL. Screws connect a rigid top cover with the bottom PMMA plate and compress the o-rings. An image of the assembled flow cell is shown in **Figure 3.5**.

Studies using the flow cell shown in **Figure 3.5** indicate that the immobilized spheres remain stable at all flow rates studied (up to a maximum flow of 3 mL/min). This demonstrates that the bonding method described above results in resonators compatible with assay fluidics. As shown above,

the resonator immobilization scheme does not degrade resonator optical properties while rigidly holding the spheres on the substrate surface under high flow rates. This approach, therefore, removes a significant barrier encountered when integrating microsphere resonators with the fluidics necessary for assay development using the WGM imaging method.

3.3.6 Lipid bilayer sensing using WGM resonators

Lipid films containing ganglioside GM1 were transferred onto immobilized microsphere resonators to detect the presence of cholera toxin (CTx) using WGM imaging. CTx is secreted by *Vibrio cholera* and leads to the debilitating diarrhea associated with cholera infection.[8] CTx is a 85 kDa protein containing one active alpha subunit and five binding beta subunits which bind GM1, an acidic glycosphingolipid found ubiquitously in the outer leaflet of cellular membranes.[8] The high affinity of CTx beta subunit (CTxB), a 11.4 kDa protein, for GM1 is considered a model for protein-sugar interactions and has reported K_d values ranging from nanomolar to picomolar depending on the particular system studied.[10] In our study, a 57 kDa non-toxic pentameric CTxB fluorescently labeled with Alexa 555 (CTxB-A555) was detected.

A monolayer of DOPC containing 5 mol% GM1 was transferred onto a microsphere/substrate platform at a surface pressure of 25 mN/m using the LB method. A second monolayer at the same surface pressure and composition was deposited on the first using the Langmuir Schaeffer (LS) method, creating a bilayer covering the entire surface area of the substrate. At this surface pressure, both GM1 and the dye marker distribute homogeneously in the DOPC lipid film matrix. To confirm that the membranes incorporating GM1 were capable of CTxB binding, bulk fluorescence imaging of the bilayers were measured following the addition of fluorescently labeled CTxB-A555.

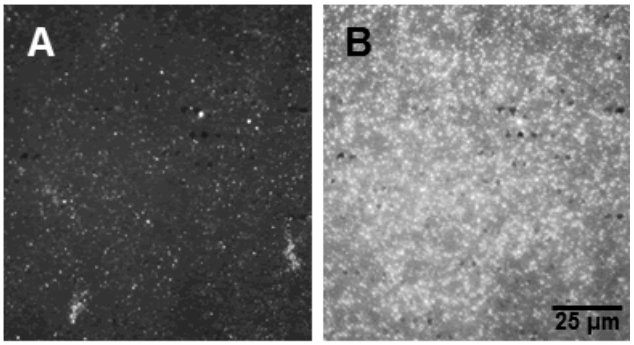

Figure 3.6. Bulk fluorescence assay of the binding of fluorescently labeled CTxB (CTxB-A555) to DOPC/GM1 bilayers transferred onto a glass substrate at 25 mN/m. Fluorescence images of the same region of the bilayer are shown following incubation with (A) 27.6 pM CTxB-A555 and (B) 110 pM CTxB-A555. The increase in fluorescence indicates specific binding of CTxB-A555 at GM1 sites in the bilayer. Control studies of bilayers composed of DOPC but lacking GM1 (not shown) do not show any significant fluorescence after incubation with CTxB-A555.

Figure 3.6 presents fluorescence images of a DOPC/GM1 bilayer following increasing additions of CTxB-A555. The images are taken in the same region of the bilayer, which was allowed to react with the indicated dose of CTxB-A555 for 5 minutes, flushed with PBS buffer, and imaged. As seen in **Figure 3.6**, exposure of the bilayer to increasing aliquots of CTxB-A555 leads to increased fluorescence intensity, as CTxB-A555 binds to the GM1. Control studies using substrates coated with pure DOPC bilayers, lacking GM1, exhibited constant background signals over the same CTxB-A555 dosing levels. This suggests that the increase in fluorescence observed arises from specific interactions between GM1 and the CTxB-A555.

Having confirmed that CTxB-A555 specifically binds to the GM1 in the transferred membranes, studies were carried out to explore the WGM response of the membrane coated microspheres. For this study, TR-DHPE was incorporated into the lipid bilayer at 0.25 mol% to provide a fluorescence marker for the WGM imaging. To ensure consistency with the bulk fluorescence studies, the fluorescently labeled CTxB-A555 was also used in these binding studies. However, long pass filters were inserted to remove any residual fluorescence from the A555 marker. Using the WGM fluorescence imaging approach outlined in **Figure 3.3**, WGM excitation spectra were collected as a function of CTxB-A555

dose. **Figure 3.7** shows a typical series of WGM excitation spectra collected as a function of CTxB-A555 concentration. Prior to the addition of CTxB-A555, this particular microsphere resonator had a WGM resonance centered at 632.98 nm with a Q-factor of 1.0×10^5. With the addition of 2.8 pM CTxB-A555, the peak red-shifts 6.33 pm as CTxB-A555 binds to the GM1/DOPC bilayer on the sphere surface, which changes the effective refractive index around the resonator. The peak continues to red shift as additional CTxB-A555 is added as shown in **Figure 3.7**.

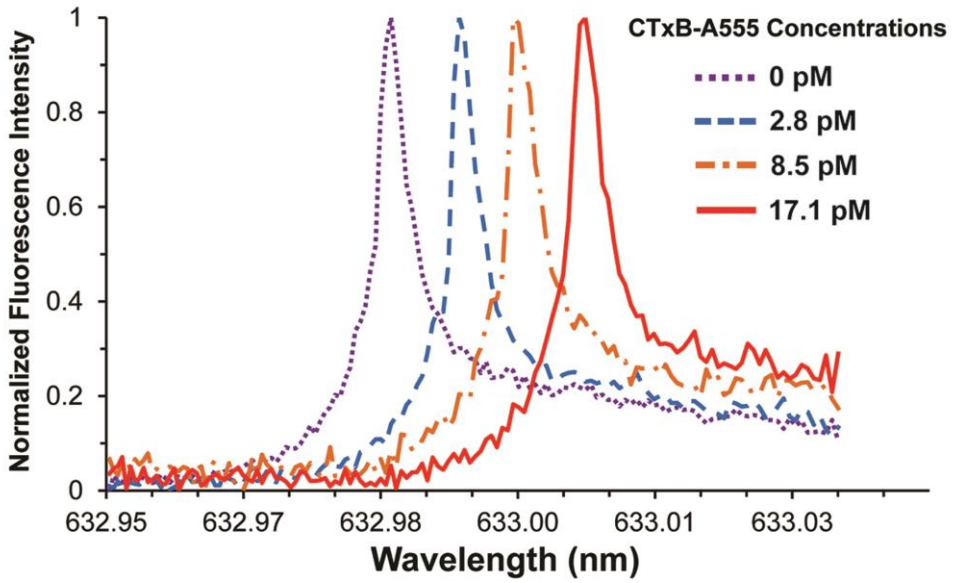

Figure 3.7. Representative WGM excitation spectra extracted from the same microsphere resonator at four different CTxB-A555 concentrations. Specific binding of CTxB-A555 to the GM1 containing bilayer coated around the microsphere, changes the effective refractive index and shifts the WGM resonance.

The results in **Figure 3.7** are summarized by the binding curve shown in **Figure 3.8**. This figure plots the WGM resonance shifts as a function of CTxB-A555 concentration, exhibiting the classic binding curve shape expected. The binding curve saturates at approximately 4.0×10^{-11} M CTxB-A555 and fitting the curve yields a measured K_d value of 1.5×10^{-11}. This value is in the range of the reported values (7.3×10^{-10} to 4.6×10^{-12}) measured using surface plasmon resonance.[9,10]

The calcium/alconox immobilization protocol adapted for microsphere resonators is compatible with lipid bilayers and was used for the detection of GM1 to CTxB-A555 binding. The high degree of compositional control using lipid bilayer films with WGM lends itself to study dye loading effects on resonator quality factors. The next section describes the dye loading effect on quality factors and describes the potential impact of dye loading on sensor performance.

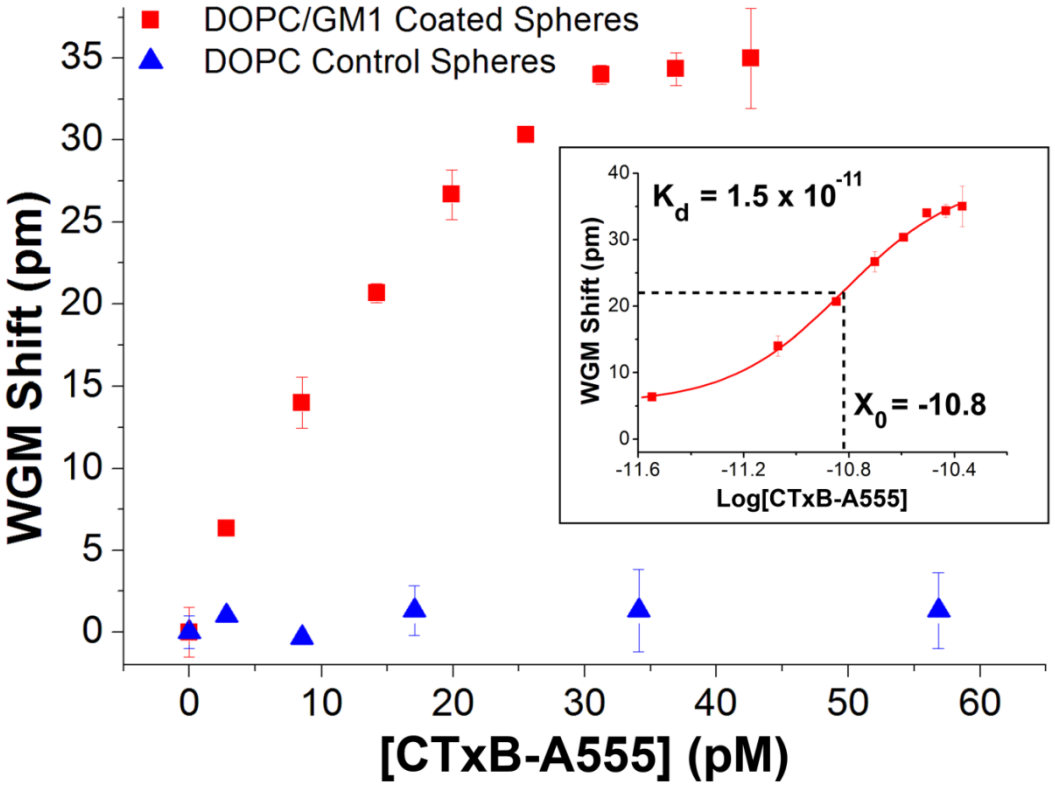

Figure 3.8. CTxB-A555 binding curves measured by tracking shifts in the WGM resonance with CTxB-A555 concentration. For resonators coated with DOPC bilayers incorporating GM1 (red squares) the binding curve shows a saturation response with a detection limit of 3.3 pM. This is compared with control studies using spheres coated with pure DOPC bilayers (blue triangles), which show negligible shifts with CTxB-A555 addition. The inset shows a log plot of the data from which a K_d of 1.5 x 10^{-11} is calculated, which is consistent with literature values.

3.3.7 Relationship between dye concentration and WGM performance

Model membranes coated on the WGM resonators not only serve as a matrix containing capture material in biosensing as discussed previously but also provides a useful tool for assessing

resonator performance. WGM imaging utilizes dye as a resonance reporter enabling the measurement of hundreds of WGM resonances in a single experiment. However, as these fluorophores absorb energy from the resonant cavity, they operate as a mechanism of light loss from the resonator. This can potentially limit Q-factor and resonator performance which in turn can diminish sensor metrics.[15,16] Systematically varying concentration is hard to do using dye functionalized spheres. Whereas, the compositional control provided by LB lipid films enables the reliable transfer for a film of known dye concentration to the immobilized sphere surface. Therefore, dye incorporated LB films were used to measure the effect of fluorophore absorbance on resonator performance.

Here, a DOPC monolayer only doped with known concentrations of TR-DHPE dye was deposited on the immobilized microsphere substrate. The WGM resonances of these spheres were measured by using the dove prism light coupling method to excite at least 20 spheres simultaneously. The WGM spectra were collected and Q-factors were recorded at each dye concentration.

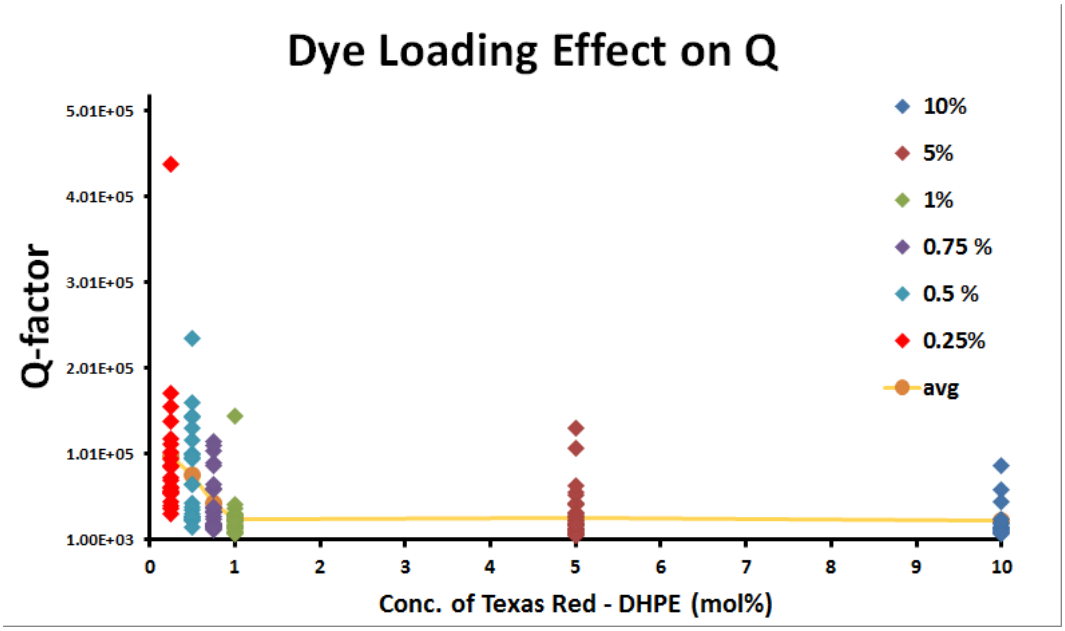

Figure 3.9. A plot of the quality factor versus TR-DHPE concentrations. The data (n = 10) shows that lower concentrations of TR-DHPE are correctly to higher average quality factors. As dye concentrations reach less than 0.25% the effect on quality factors become more significant.

Figure 3.9 plots Q-factors observed as the dye concentration is increased from 0.25 mol% to 10 mol% TR-DHPE. The averages of the Q-factors show the expected trend where reducing the number of light absorbing molecules from the surface of these WGM resonators leads to improved Q-factors. For sensing applications, higher Q-factors lead to improved sensor performance. Interestingly, no measurable difference in Q-factors was observed in concentrations higher than 1 mol% of TR-DHPE. But at lower concentrations (< 1 mol%) there is a slight increase in the statistical average of quality factors. We note that WGM resonance measurements at lower concentrations of TR-DHPE were difficult due to low fluorescence signals and photobleaching. As quality factor improves to push the limits of detection lower, the use of dye as a resonance reporter is a limitation for sensing, therefore, an approach based on scattering signals will be discussed in the follow chapter.

3.4 Conclusions and Future Directions

This chapter highlighted the development and application of microspheres immobilized on a substrate to improve fluidics using WGM imaging. High index microspheres were immobilized onto glass substrates using a calcium-assisted bonding method. The bonding method did not degrade the optical properties of the immobilized resonators, which was confirmed through characterization of resonator Q-factors. The immobilized resonators were stable in the fluidics necessary for assay development and amenable to lipid film transfer using the Langmuir-Blodgett and Langmuir-Schaeffer methods. Bilayers transferred onto immobilized spheres using the sequential transfer of monolayers of DOPC doped with 5 mol% GM1 were fabricated to detect CTxB-A555 which binds to GM1. Bulk fluorescence studies confirmed the specific binding of CTxB-A555 to GM1. This was also characterized by measuring shifts in the WGM resonance. Analysis of the resulting binding curves from WGM imaging

measurements yielded a K_d value of 1.5 x 10^{-11} which is consistent with previous SPR measurements. The measured detection limit of 3.3 pM is competitive with other approaches and the small size of the microspheres reduces the detection footprint and amount of material needed.

The LB film was also used to systematically control the dye concentration used in WGM imaging to study dye loading effects on resonator quality factors. We conclude that lower concentrations of dye (less than 1 mol%) indeed results in higher quality factors. However, due to the low concentrations of these dye molecules, fluorescence signals required for WGM measurement readily photobleach which deters any prolonged measurements. The next chapter summarizes a scattering approach to overcome dye loading issues for improved quality factors.

In summary, the calcium bonding method is shown to lead to stable and immobilized resonators that are compatible with the fluidics necessary for assay development. The simple immobilization procedure does not require expensive equipment or elaborate fabrication processes, thus making the approach generally applicable. This, therefore, removes a significant barrier for the development of sensitive, multiplexed biosensors using the superior optical properties of high-Q microsphere resonators. The favorable optical properties of spheres coupled with their availability in a wide range of sizes and materials opens new opportunities for cost effective assay development and deployment.

3.5 References

1. Vahala, K. J. Optical microcavities. *Nature* **2003**, *424*, 839-846.
2. Soria, S., et al. Optical microspherical resonators for biomedical sensing. *Sensors* **2011**, *11*, 785-805.
3. Washburn, A. L., et al. Label-free quantitation of a cancer biomarker in complex media using silicon photonic microring resonators. *Anal. Chem.* **2009**, *81*, 9499-9506.
4. Washburn, A. L., et al. Quantitative, label-free detection of five protein biomarkers using multiplexed arrays of silicon photonic microring resonators. *Anal. Chem.* **2009**, *82*, 69-72.
5. Huckabay, H. A., et al. Whispering gallery mode imaging for the multiplexed detection of biomarkers. *Sens. Actuators, B* **2011**, *160*, 1262-1267.
6. Huckabay, H. A., et al. Label-free detection of ovarian cancer biomarkers using whispering gallery mode imaging. *Biosens. Bioelectron.* **2013**, *45*, 223-229.
7. Allen, P. B., et al. Calcium-Assisted Glass-to-Glass Bonding for Fabrication of Glass Microfluidic Devices. *Anal. Chem. (Washington, DC, U. S.)* **2008**, *80*, 7153-7157.
8. Reed, R. A., et al. Interaction of Cholera-Toxin with Ganglioside Gm1 Receptors in Supported Lipid Monolayers. *Biochemistry* **1987**, *26*, 824-832.
9. MacKenzie, C. R., et al. Quantitative analysis of bacterial toxin affinity and specificity for glycolipid receptors by surface plasmon resonance. *The Journal of biological chemistry* **1997**, *272*, 5533-5538.
10. Kuziemko, G. M., et al. Cholera toxin binding affinity and specificity for gangliosides determined by surface plasmon resonance. *Biochemistry* **1996**, *35*, 6375-6384.
11. Gorodetsky, M. L., et al. Optical microsphere resonators: optimal coupling to high-Q whispering-gallery modes. *J. Opt. Soc. Am. B* **1999**, *16*, 147-154.
12. Girard-Egrot, A., et al. In *Nanobiotechnology of Biomimetic Membranes*, Martin, D., Ed.; Springer US, **2007**, pp 23-74.
13. Davis, F., et al. Structured thin films as functional components within biosensors. *Biosensors & Bioelectronics* **2005**, *21*, 1-20.
14. Terrettaz, S., et al. Protein-Binding to Supported Lipid-Membranes - Investigation of the Cholera-Toxin Ganglioside Interaction by Simultaneous Impedance Spectroscopy and Surface-Plasmon Resonance. *Langmuir* **1993**, *9*, 1361-1369.
15. Foreman, M. R., et al. Whispering gallery mode sensors. *Advances in Optics and Photonics* **2015**, *7*, 168-240.
16. Kippenberg, T. J. A. *Nonlinear optics in ultra-high-Q whispering-gallery optical microcavities*. California Institute of Technology **2004**.

Chapter 4

Platform Development for Whispering Gallery Mode Microspheres

4.1 Introduction

In the previous chapters, we showed that fluorescence imaging can be used to track WGM resonances of a field of fluorescent dye labeled spheres.[1] This enabled multiplexed detection of three putative biomarkers of ovarian cancer in a single assay with minimal cross-talk. The whispering gallery mode imaging approach, in general, provides a flexible, sensitive and label-free approach for biosensing. However, additional improvements were needed to develop a robust system that can withstand fluidic exchanges required for a clinical test. Therefore, we described a soft glass-to-glass bonding method with a calcium acetate/alconox solution to adhere microspheres to a glass substrate.[2] This enabled spherical microspheres to resist movement during routine fluid exchanges required for immunoassays.

In this chapter, we further investigate and demonstrate whispering gallery mode detection using a tapered fiber coupling scheme, optical films, and scattering WGM detection in an effort to improve quality factors. We also demonstrate tapered fiber coupled microspheres as a dip sensor for droplet sensing. We propose the use of this dip sensor with fluid handling platforms such as digital microfluidics. Additionally, we introduce several microfluidic prototypes that can integrate WGM microsphere resonators as an on-chip detection platform.

4.2 Materials and Methods

4.2.1 Thin Film fabrication for Q-factor Study

Microscope slides (Fisher Scientific) were rinsed with water and dried with nitrogen. Roughly 250 µL of AL-2233 material (Fiber Optic Center, New Bedford, MA) was pipetted to the center of the substrate on the spin coater. Spin coating conditions were set at ~5,000 rpm for ~30 sec to ensure complete coverage of the substrate and even height profiles. Post-spin, the substrate was placed in a 60°C oven to remove residual solvent. For thicker layers, this procedure was repeated to increase the coating thickness in increments of ~60 nm per spin.

4.2.2 Tapered fiber optic coupling

Fiber tapers were prepared by the following method. The jacket of a single mode optical fiber (630 HP, Edmund optics) was stripped to expose the cladding. After cleaning with ethanol to remove any residual material, the stripped portion of the fiber was placed in a laser-based micropipette puller (P-2000, Sutter Instruments) at the following settings: heat 250, velocity 5, delay 0 and pull 100. The proximal end of the tapered fiber and the distal end of light carrying fiber were fused using a fusion splicer (FSM-40S, Fujikura). The fabricated fiber was coated with PDMS by gently dipping the tapered portion of the fiber in a PDMS solution diluted with ethanol (50/50 v/v). The PDMS mixture of 10:1 polymer to curing agent (Sylgard 184, Dow Corning) was diluted with ethanol to create a thin but tactile coating on the fiber taper. Microspheres were then placed on the PDMS coated fiber taper and allowed to cure for at least 2 hours to complete the fabrication of the tapered fiber-resonator dip sensor.

4.2.3 Scattering WGM Assays

Refractive index measurements were made in solutions of NaCl (Fisher Scientific) mixed with appropriate amounts of 18 MΩcm water to make 1.332, 1.333, 1.334, 1.336, 1.339 and 1.343 RIU calibration standards. The flow cell illustrated previously in **Figure 3.5** was used having a reservoir volume of 500 µL. After each injection of RI solution, the resonant wavelength (n = 3) was measured and recorded after a 10 minute incubation. The images were captured using a CMOS camera (Model number 413C, Edmund Optic) through a 10x objective (UMPLanFL, Olympus). Data analysis was automated via custom programmed LabView (National Instruments) software. The LabView code is provided in the appendix. Bioassays for the detection of interleukin-6 (IL-6, BD Bioscience) in a concentration range of 0 to 563 pg/mL were performed. All IL-6 solutions were diluted in pH 7.4 phosphate buffer saline (PBS) (27 mM KCl, 15 mM KH_2PO_4, 1400 mM NaCl and 81 mM Na_2HPO_4, MP Biomedicals) obtained at 10x concentration.

4.2.4 Microfluidic Platform Fabrication

Microfluidic photomasks were designed using AutoCad (AutoDesk) software. "Type D" marks two characteristics of the photomask: 1) the chrome layer will be plated on the bottom face of the film. 2) The desired microchip structures are indicated by white (clear) drawings in the AutoCad software. The resulting photomask from Infinite graphics (IGI) are negative films where the clear portions of the mask represent UV exposed areas and the dark areas represent unexposed areas. UV light crosslinks the SU-8 polymer thereby creating raised features on the silicon wafer.

A silicon master was created using SU-8 100 negative photoresist spun onto a 4 inch diameter silicon wafer to a thickness of 100 µm using a spin coater (Cee 100, Brewer Science). The wafer was then heated to 65°C for 10 min and ramped to 95°C for 30 min on a programmable hotplate (Thermo Scientific). After this "soft" bake, the negative mask was aligned on top of the photoresist coated wafer

and exposed at 344 mJ/cm^2 using a UV flood source (ABM Inc.) for 27 seconds. After exposure, the wafer was heated to 65°C for 5 min and ramped to 95°C for 20 min. The master was developed in SU-8 developer for 20 mins, rinsed with isopropyl alcohol and dried with nitrogen. Then, the master was finalized with a 2 hr "hard" bake step at 200°C. To create a PDMS chip from the silicon master, PDMS/curing agent mixed at a 10:1 ratio was poured onto the master and cured for at least 2 hours at 70°C. Microchannel reservoirs for buffer and waste were punched into the PDMS using Uni-Core biopsy punch (Ted Pella). Spheres stored in solution were pumped through the channel via negative pressure using a 5 mL syringe at the outlet of the channels. To perform refractive index assays in these devices, solutions of ethanol and deionized water were pressure injected using a 5 mL syringe pump.

4.2.5 Digital Microfluidics Fabrication

Glass substrates (plain beveled edge, Fisherbrand) were taped along the walls of the vacuum chamber dome using copper tape in an evaporative coater. A pressure of roughly 7.6 x 10^{-2} torr was achieved using a vacuum pump (MOD 1101006418, Franklin Electric) then a turbo pump (Turbovac 151, Leybold) was used to further lower the pressure to roughly 10^{-5} torr. Aluminum was evaporated by resistive heating to coat a thin film on the glass substrates. A shutter was placed over the metal plate holding the aluminum target to controllably coat the glass substrates. The shutter was opened for roughly 5 seconds to coat the glass substrate using a deposition monitor (Infinicon XTM/2). The vacuum was returned to atmosphere and the glass substrates now coated with aluminum were removed. The electrode contact pads (2 x 2 mm) were outlined using a M25 CO_2 Laser Engraver (University Laser Systems) at power 12.0% and speed 2.6%. The laser was used to etch away the aluminum coating isolating each electrode from each other. These electrode contact pads were designed to be adjacent to each other such that a small 100 μL droplet of solution creates an electrical circuit between 2 electrodes as shown in **Figure 4.1**.

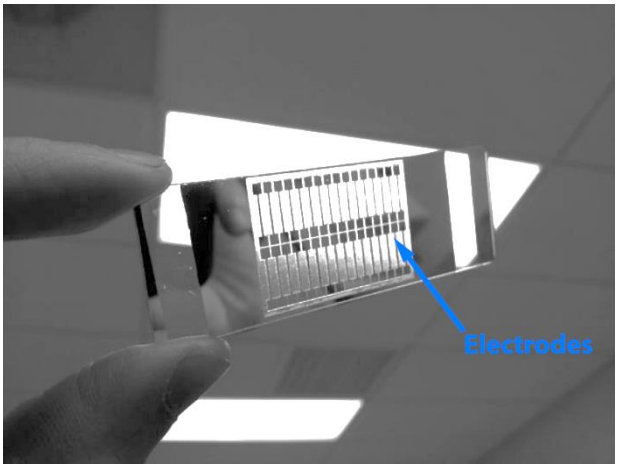

Figure 4.1. A DMF substrate. The electrodes were fabricated by etching aluminum to outline the electrodes shown here. The electrodes are electrically isolated but neighbor other electrodes for droplet actuation.

Then, several drops of silicone oil were dispersed and covered with Saran wrap. The chip was baked at 100°C for 1 hr to adhere the Saran wrap to the electrode surface. A solution Rain-X© and isopropyl alcohol in a 1:5 w/w ratio was distributed on top of the chip surface and dried on a hot plate at 80°C for 20 mins. The resulting digital microfluidic chip was actuated using a flyback transformer from a CRT monitor. The output of the power supply when a 5 V square wave at 10 kHz is applied is 300 to 1000 V. Voltages were carefully applied using well insulated leads.

4.3 Results and Discussion

4.3.1 Light coupling

The first attempts to couple light microsphere structures used a free-space laser beam focused on to the edge of a sphere.[3,4] These off-axis Gaussian beams directed at spherical structures exhibit resonances that could exhibit quality factors up to 10^{6}.[3] Free-space light coupling, however, has less utility for most practical refractive index sensing applications due to mie scattering. Light coupling via evanescent fields, on the other hand, effectively introduces light with efficiencies in the range of up to

80 up to 99.99%.[5-7] One example of evanescent field coupling is performed by directing light from a laser source at a prism permitting total internal reflection on the prism interface as shown in **Figure 4.2**.

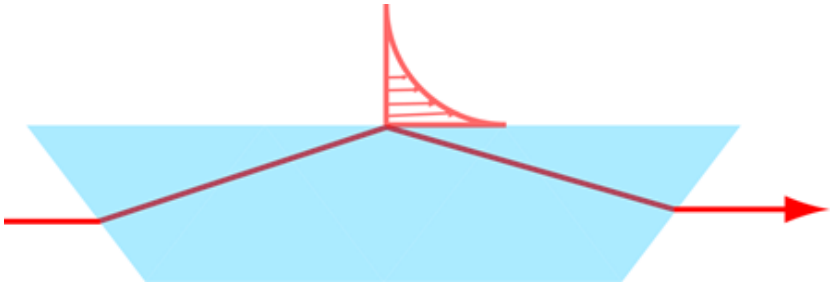

Figure 4.2. Illustration of an evanescent wave created by TIR on the surface of a dove prism.

This creates an evanescent field component at the prism surface and decays outwardly. When a microsphere is placed within the evanescent field, photons are transferred into the microsphere via frustrated total internal reflection. The photons that are coupled into the microsphere structure travels along its circumference ultimately returning to the location. At this point, the photon can either be recirculated in the structure or transferred out of the microsphere back into the prism. The degree of overlap between the resonator and the evanescent wave formed at the light coupling interface has an effect on the efficiency of the light coupled in and amount of light coupled out of the resonator. Therefore, coupling gap distances can affect the overall sensor performance.

4.3.1.1 Coupling gap distance

An optimized gap between the resonator and coupling surface can allow sufficient pumping of photons into the resonator structure but more importantly reduce the amount of photons that can couple out of the microsphere into the prism. **Figure 4.3** illustrates coupling gap conditions that lead to optimized photon pumping into the resonator.

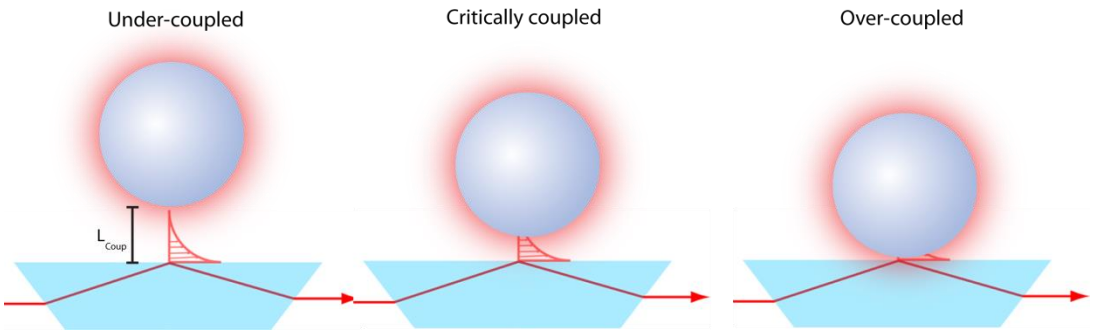

Figure 4.3. Illustration of coupling motifs. (left) under-coupled regime where the resonator has little interaction with the evanescent wave. (middle) critically coupled regime where a slight distance between the resonator and dove prism is introduced. (right) over coupled regime where the resonator rests directly on top of the dove prism.

The evanescent wave decay length, d, is given by:[8]

$$d = \frac{\lambda_0}{4\pi n_1}(sin^2(\theta - n^2)^{-1/2} \qquad \text{Equation 4.1}$$

where λ_0 is the wavelength of light, n_1 is the refractive index of the prism, θ is the angle of incidence, n_2 is the refractive index of media at the interface of the coupling prism and n is (n_2/n_1). For example, a system with λ_0 = 633 nm, θ is 65°, dove prism, n_1 = 1.515, and solution of water, n_2 = 1.333, the decay length is roughly 153 nm. In **Figure 4.3**, the left-most motif is an under-coupled system where the distance between the resonator and prism surface, l_{coup}, is much greater than d. This leads to very little overlap of the evanescent tail with the resonant mode of the microsphere. This under-coupled regime, leads to very few photons being pumped into the resonator. For sensing, this regime may exhibit lower sensing metrics as low number of photons lead to low electric field densities within the resonator structure available for surface sensing interactions. In contrast, the far right image of **Figure 4.3** shows the over-coupled regime where the large overlap of the evanescent wave and the microsphere leads to efficient photon pumping. However, due to the close proximity the microsphere and prism, light scattering losses dominate due to higher photon out coupling rates. This results in low quality factors

with lower sensor performance. The ideal coupling is a balance of the two previous regimes illustrated in the middle of **Figure 4.3**. This is termed as critical coupling where light is efficiently pumped into the resonator and the slight gap between the two surfaces minimizes out coupling of photons.[9-11] This regime, therefore, maximizes the field density by efficiently retaining the photons within the microsphere structure with lower light loss. High field densities lead to greater interaction between the recirculated light and the microsphere's local environment.[12,13] This presents advantages for sensing applications where improved field densities lead to higher sensitivities.

In practice, to achieve critical coupling, a device that physically controls the distance between the two surfaces, such as a micromanipulator or pedestal, can be used.[13,14] This configuration utilizes a resonator fabricated at the tip of a capillary and is micromanipulated by holding its stem.[14-16] A tapered fiber is meticulously aligned at a particular distance from the microsphere to achieve critical coupling. This platform is less amenable for fluidic exchange systems due to the bulkiness of the fiber alignment systems. Instead of micromanipulating the more thinned fiber, stem-held spheres were introduced to maintain optimized gap distances. These stem-held spheres have been introduced into microfluidic devices,[17] the aligning of a fiber optic within a microfluidic cell makes mass fabrication a challenge and can be difficult to maintain. Here, we introduce an index matched gap material to achieve critical coupling for improved sensor performance using a prism light coupling configuration.

The material, AL-2233 (Fiber Optic Center, New Bedford, MA), is a transparent polymer with a RI of 1.33, is traditionally used as a low refractive index light guide cladding or as anti-reflection coatings. For our purpose, this material provided a thin coating of a RI similar to that of water. Using an index matched coating creates an "optical gap" for the resonator as shown in **Figure 4.4**.

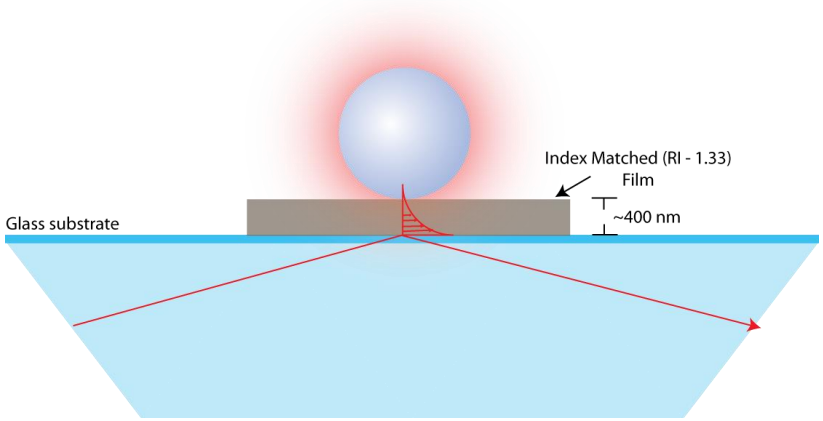

Figure 4.4. Illustration of an index matched optical film used to critically couple light into the resonator.

The light undergoes TIR at the interface between the prism and refractive index coating matched to that of water. The evanescent wave extends through the coating critically coupling into the resonator. The thickness of the film was increased in layer increments where each coating application would add a thickness of roughly 60 nm. The quality factors of spheres with the index matched coating substrate showed the potential of exhibiting higher quality factors, up to 10^6, using a prism coupling set up compared to the typical 10^4 Q-factors observed as shown in **Figure 4.5**.

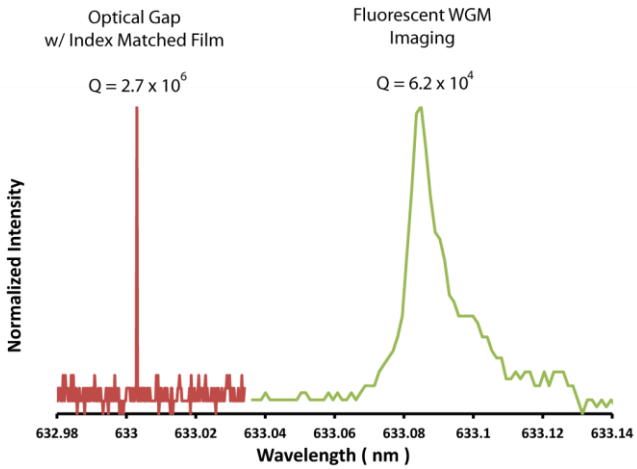

Figure 4.5. WGM spectrum shown on the left was obtained using the schematic shown in figure 4.4 where the sphere was placed on top of an optical film for critical coupling. The WGM spectrum on the right was obtained from a sphere resting on the coupling surface.

However, some microspheres in the gap prism configuration continued to exhibit lower quality factors. This may be attributed to uneven coating methods. A characterization of the coating profile studying a large coating area could perhaps elucidate this. Initial results, however, show that a gap between the coupling surface and resonator statistically improved the overall Q-factors as expected.

The gap height or film thickness was characterized using a 2D stylus profilometer (Tencor Alphastep 200). We were limited to measurements on the edges of the film coating where the height contrast provided estimates of the film thickness. The highest quality factors were observed on film thicknesses of ~250 nm ± 20 nm. Compared to the evanescent length previously calculated of 153 nm, the optical coating is much thicker. This is possible because the exponentially decaying evanescent wave still has some electric field density beyond the calculated evanescent decay length allowing photon coupling. Improvements in quality factors can translate into higher sensor performance in metrics, such as sensitivity and limits of detection however must be proven with more rigorous sets of studies.

4.3.1.2 Fiber coupling

Several methods can be used, such as fiber coupling, prism coupling and waveguides, to evanescently couple light into microspheres. We have primarily utilized prisms to couple light into resonators taking advantage of the ability to excite a field of spheres with easy alignment. Prisms exhibit efficiencies around 80 – 90%, where the loss is mainly due to the phase mismatch. Fiber optic waveguides, on the other hand, can provide almost perfect coupling capable of coupling efficiencies up to 99.99% in previous studies.[5] While fibers have been used to couple light into WGM structures, more unique platforms using tapered fibers as a sensor device have yet to be fully explored.

One group led by Teraoka have developed a more robust dip sensor platform by bending the stem of a fiber, with a sphere at the end, roughly 90° to align two optical fibers.[18] One fiber acts as the light feed and the other fiber as a light monitor. They demonstrated a repeated dipping measurement between water and a 0.10 wt % sucrose solution.[18] These initial demonstrations show the promise of WGM light coupling in a robust manner, however, they are relatively difficult to fabricate primarily due to the difficulty in aligning two fibers precisely parallel to be able to record the resonators WGM spectra. These fabrication challenges can be alleviated using WGM imaging where we require just one fiber as the light feed and use a camera as a method to readout WGM resonances. Here we explore the use of fiber optic coupling for applications as a dip sensor using WGM imaging.

Dip sensors have the advantage of being robust and easy to use devices. They are compact by design and thus are amenable to point-of-care testing.[19] Polished or tapered fibers are more compact and can be incorporated as a dip sensor. The light from a fiber optic undergoes TIR through the core of the fiber creating an evanescent wave that can be coupled into the resonator. **Figure 4.6** shows a fiber that was tapered using a laser-based micropipette puller (Sutter instrument, Novato, CA). The taper portion of the fiber was thinly coated with a PDMS solution diluted in 50% ethanol solution. The adhesion properties of PDMS were exploited to fix microspheres to the coupling fiber as shown in **Figure 4.6.**

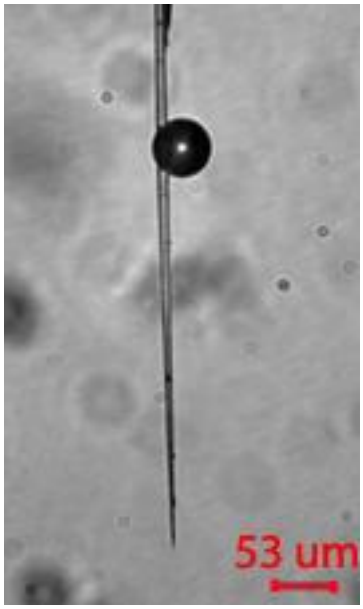

Figure 4.6. An image of a thinned fiber optic with a 53 um microsphere bonded to the fiber using a thin coating of PDMS.

This device was used as a dip sensor by measuring the refractive index changes when placed in a droplet of water versus a droplet of 5% glycerol with rinsing steps in between. Measurements were repeated a total of five times between the two solutions. **Figure 4.7** shows that the resonant wavelength correctly senses the refractive index change between the two solutions of water (n = 1.333) and 5% glycerol (n = 1.340).

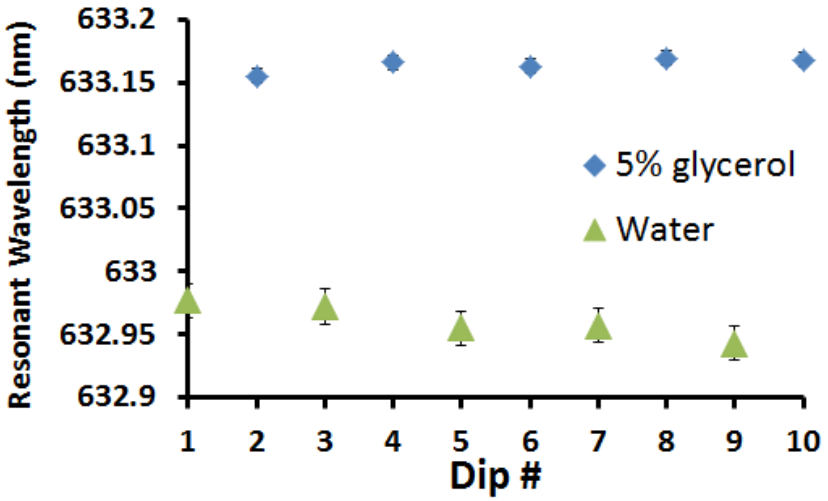

Figure 4.7. The resonant wavelength was measured while the fiber optic dip sensor was alternatingly placed into a droplet of water and a droplet of 5% glycerol.

The standard deviations for the measurements in solutions were 5 pm and 8 pm for water and glycerol, respectively. We also note that this light coupling scheme routinely exhibited quality factors at ~10^5, roughly an order of magnitude higher than prism coupling. These initial results show the promise of sensing for droplet sensing using microsphere resonators in a dip sensor platform using WGM imaging. However, for routine uses of these dip sensors, using fluorescent dye as a reporter for WGM resonance is a drawback due to photobleaching inhibiting long term use. Therefore, an alternative scattering method for WGM measurements is presented to overcome this challenge.

4.3.2 Scattering Signals for WGM measurements

Fluorescently tagged microsphere resonators provide a unique platform for multiplexed detection.[1] For long lasting and robust diagnostics, platform where the WGM signal must be measured for long repeated uses, photobleaching is a limitation. On the other hand, evanescently scattered signals, which can be used to track resonances, provide a consistent signal, where its intensity solely

depends on the intensity of the light source. These signals can be measured using less expensive CMOS cameras reducing the cost of the platform. Here, evanescent scatter signals are demonstrated as a useful alternative for tracking WGM resonances in sensing applications.

4.3.3 Evanescent wave scattering

Previously, we have described the formation of the evanescent wave when total internal reflection occurs at the interface between two different refractive index media. When WGM microspheres are placed in the evanescent wave, the energy transfers into the material and scatter light. The intensity of the scattered light has been determined to be a function of distance between the surface and microsphere described by the equation:[20,21]

$$I_{sc}(h) = I_{sc,0}\exp(-2k_2\beta * d) \qquad \text{Equation 4.2}$$

where I_{sc} is the scattering intensity, d is the distance between the surface and microsphere, k_2 is the wave number and β represents the decay constant. The exponential relationship between the I_{sc} and d has shown utility for measuring electrostatic[22,23], Van der Waals[23,24], depletion[25,26] and steric interactions[27]. Here, we exploit these scattered intensities for a different application. The strong scattering intensity exhibited by a microsphere placed close to the light coupling surface can measured as a tool for tracking WGM resonances.

WGM imaging, as mentioned previously, can visualize the light path and exhibit mode patterns which may have unique applications. However, the fluorescent dye photobleaches with prolonged use which is a drawback for real time signal monitoring. Scattering WGM, on the other hand, relies on signals formed by the evanescent wave scattering signals that only depend on intensity of the light

source. **Figure 4.8** shows images from a CMOS camera using scattering WGM in transmission light (left) and no light (right).

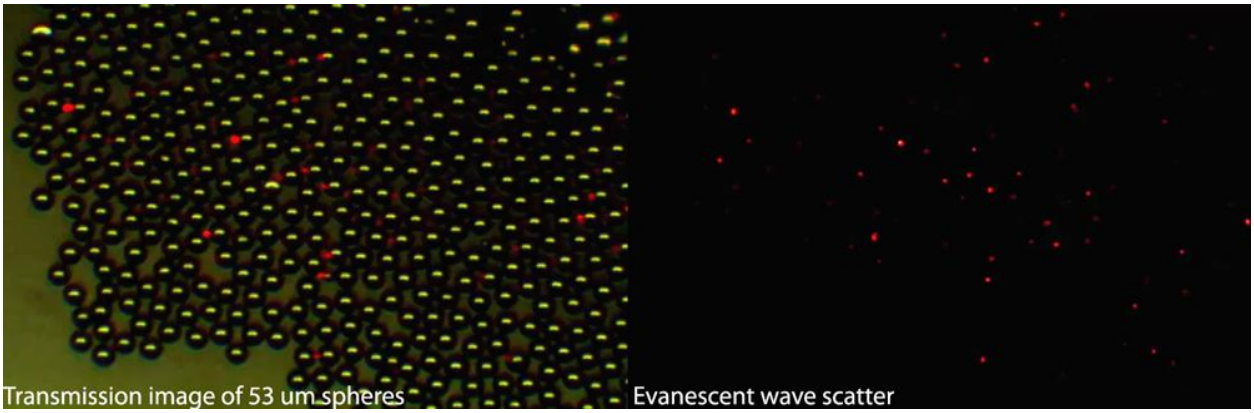

Figure 4.8. (left) Transmission image of 53 um spheres on top of a dove prism. The evanescent scattered spots can be seen as red dots on the edge of the spheres. (right) The background light is turned off to visualize the scattering spots for WGM measurements.

The resonant wavelength can be determined by monitoring the intensity of each scatter spot while tuning the laser wavelength similar to WGM imaging. The bright, laser power dependent signal provides a flexible and consistent signal for which to perform WGM refractive index and immune-specific assays. These images were captured using an inexpensive CMOS camera (~$300 vs ~$6,000 for a CCD). These USB cameras are compatible with LabView automation which can markedly improve data handling throughput.

4.3.4 Data analysis programming: LabViews

The ability to excite a large field of spheres with high signal intensities using scattering WGM enables a platform where hundreds of resonances can be measured simultaneously in a short experiment (less than a minute). However, analysis of data for hundreds of resonators is done

manually, where each resonance spectra is fit using a lorentzian curve using Origin software taking roughly 5 minutes for each resonator and calibration point. To truly improve the throughput of analysis, an automated analysis program was devised.

LabView programs have a variety of functions that can interface most current instruments to a computer portal. Their programming features for current USB cameras (LabView Vision) along with available mathematical functions were used to automate the analysis of WGM spectra. The user-interface of the program is shown in **Figure 4.9**. The image stacks obtained during the tuning of the laser is organized into frames.

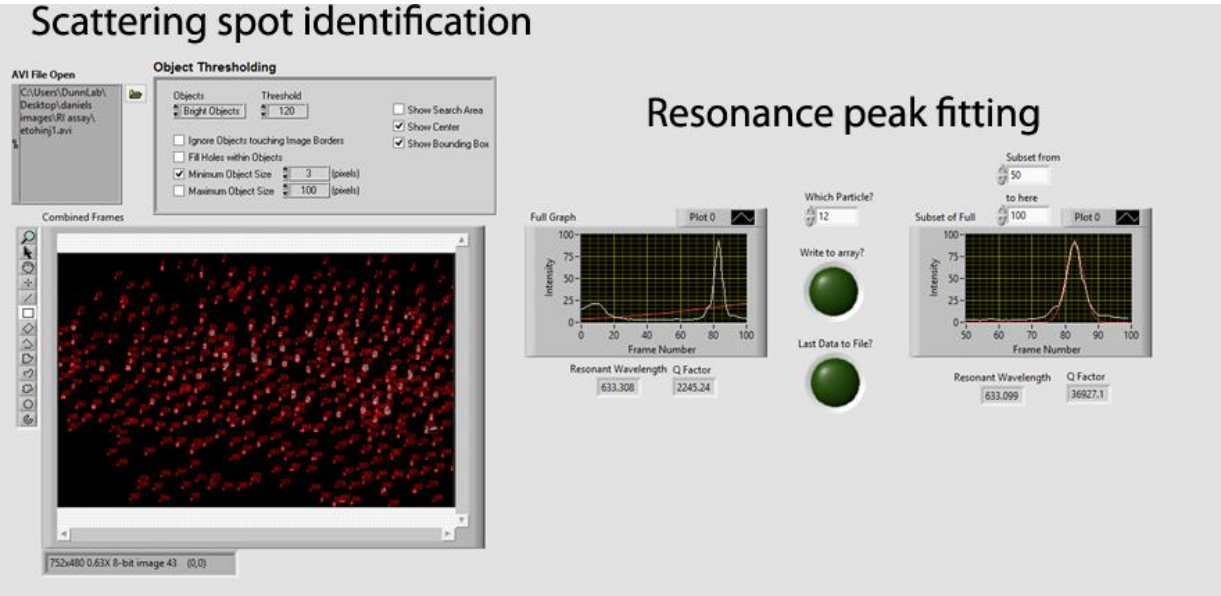

Figure 4.9. The collected scattering WGM image stacks are analyzed by identifying individual scattering spots first. Then the program fits each WGM spectra to a Guassian peak to extract the resonant wavelength. The data is recorded to a user-friendly file for subsequent analysis.

Immediately, each evanescently scattered spot is identified and cataloged into arrays. The intensity versus laser wavelength plot is graphed and fit to a Gaussian curve. We note here that the WGM spectra are Lorentzian in shape, however, identification of the resonant wavelength can also be obtained using a Gaussian curve. The scattered spots and calculated resonant wavelengths are paired

and output into a file easily transferrable to an Excel spreadsheet. Using this program, the time required for WGM assay and analysis was reduced to less than 10 mins for hundreds of resonators. The following refractive index and IL-6 immunoassay data were obtained via this high throughput analysis program.

4.3.5 Refractive index and IL-6 Measurements

Using a low cost set-up for the sensitive detection of analytes has a tremendous impact on the adoption of the technique. Therefore, enabling the use of a lower cost CMOS camera (which typically cost ~$300 USD compared to ~$6,000 CCD camera) to measure the intense scattering signals to track WGM is a significant advantage. To verify that evanescently scattered light can be utilized as non-photobleaching signal needed for WGM assays, the following refractive index assay was performed and the results are shown in **Figure 4.10**. For these measurements, sequential 10 µL injections were made to obtain this calibration plot. **Figure 4.10** indicates the linear trend (R^2 = 0.998) between the resonant wavelength shifts and refractive index.

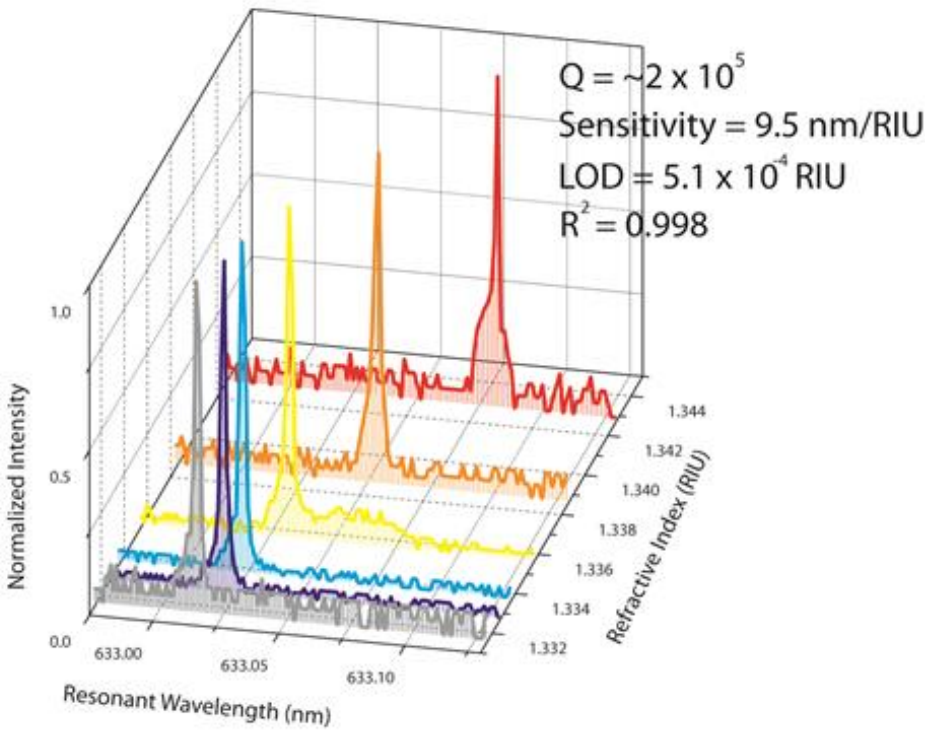

Figure 4.10. The WGM spectra are shown here as a 3-D plot with refractive index on the Z-axis. The resonant wavelength shifts changes linearly with the refractive index of the solution. The resonator using scattering WGM exhibited quality factors of 2.0 x 10^5, sensitivity of 9.5 nm/RIU and LOD of 5.1 x 10^{-4} RIU.

The quality factor of this particular resonator was 1.8 x 10^5 and exhibited a sensitivity of 9.5 nm/RIU and a limit of detection of 5.1 x 10^{-4} RIU comparable to the metrics obtained using WGM imaging (Q-factors = 10^4 – 10^5, sensitivity = 10 nm/RIU and LODs = 10^{-4} to 10^{-5}).

To further investigate the utility of evanescently scattered light as a signal for WGM measurements, we performed immunoassays in a field of ~200 spheres tracking the shifts due to binding of IL-6 to the surface of 15 resonators simultaneously. The reduced statistics is not an equipment limitation, where all 200 resonances can be measured and recorded. Rather, it is due to the limited laser tuning range (632.98 nm to 633.12 nm, or 140 pm total) such that all spheres may not exhibit resonances within this relatively condensed tuning range. Also, many of these spheres shift out of the measurable tuning range, which limits the number of microspheres that can be used in a single

assay. Using a laser with larger scanning ranges can be used to fully take advantage of this WGM detection platform to improve the statistics. Regardless, **Figure 4.11**, displays calibration plot for IL-6 with a linear correlation value of $R^2 = 0.994$.

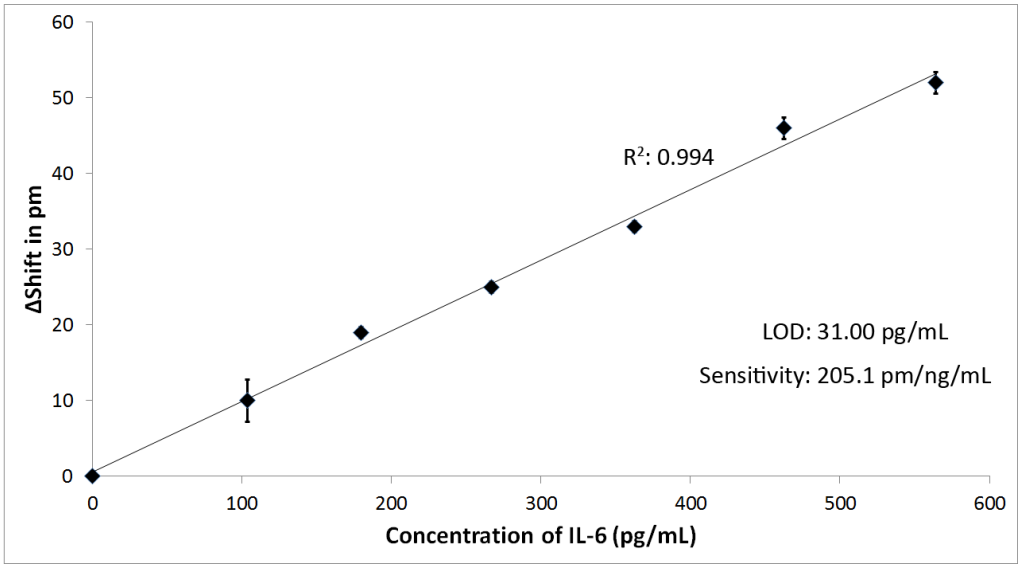

Figure 4.11. IL-6 calibration curve using scattering WGM with sensitivity of 205 pm/ng/mL and LOD of 31.00 pg/mL.

Scattering WGM exhibited generally higher LODs and sensitivities of 31.00 pg/mL and 205.1 pm/ng/mL respectively compared to previous WGM imaging immunoassays measuring CA-125, osteopontin and prolactin as shown in **Table 4.1**.

Analyte of Interest	Size	Sensitivity	LOD	Exp. Setup
CA-125	>200 kDa	18 pm/U/mL	0.23 U/mL	WGMI[28]
Osteopontin	80 kDa	14 pm/ng/mL	270 pg/mL	WGMI[28]
Prolactin	24 kDa	15 pm/ng/mL	290 pg/mL	WGMI[28]
Interleukin-6	24 kDa	205.1 pm/ng/mL	31 pg/mL	Scattering WGM

Though this is not a direct comparison, for proteins of similar molecular weights we observe improved sensitivities and lower limits of detection in the scattering WGM setup. We hypothesize that the dye used in WGM fluorescence imaging access the same surface chemistry sites as the antibodies resulting in lower surface densities of antibody for WGM imaging resonators. Without the need for dye on the resonator surface in scattering WGM detection, there may be more functional sites available for the antibodies to bind. Further characterization of antibody surface densities can be performed to confirm this observation. Here, scattering WGM was validated to enable long term continuous measurements.

4.3.6. Optical detection in microfluidics

The small footprint of WGM detector is highly suitable for separations systems in microfluidics. Microfluidic devices platforms have numerous inherent advantages of being miniature, scalable and cheap. The developed technologies have enabled the construction of devices containing multiple components with different functionalities. For example, the sampling, pre-processing, and measurement of cell lysate can all be performed in a single miniaturized device.[29-32] These demonstrations have led to the idea that one could fit an entire "lab on a chip" for a "micro total analysis system (μTAS).[32] Since the demonstration of the earliest microfluidic systems, the advancements in elastomeric materials such as poly(dimethylsiloxane) PDMS have enabled simple fabrication.[33,34] Further developments of integrating systems such as microvalves, micropillars and microwells have expanded microfluidics to a technology found in many applications[34], such as polymerase chain reaction[35,36], cell counting and sorting[37,38], drug screening[39], electrophoretic separations[40-42], DNA sequencing[43], single cell manipulation[44] and immunoassays[45]. This section will focus on the comparison of optical detectors that are commonly utilized for immunoassay applications.

Within a broad class of optical detectors, intensity based detectors that provide either fluorescent or luminescent signals are most commonly employed in microfluidic systems. Both forms of intensity based detection have advantages of being relatively easy to incorporate and being amenable to small volume systems. They provide high sensitivities and fast response useful for high throughput microfluidic systems. Fluorescence detection is achieved by incorporating labels such as a fluorophore or quantum dot to the analyte of interest. Luminescence signals can be produced by enzymatic reaction of a luminogenic substrate like luminol or luciferin derivatives or electron transfer process with an applied potential. While these approaches provide sensitive and easy detection platforms, the requirement of a label limit its application as a broad, general detection scheme for microfluidics. Labelling steps can be avoided reducing the cost and assay duration in microfluidic platforms by utilizing label-free detection.

Several common label-free platforms have been demonstrated in microfluidics platforms. To conduct SPR imaging measurements for multiplexed detections, additional microfluidic networks and gold surface patterning must be performed. Kanda et al. achieved a lateral resolution of 2 μm of their gold patterns and detected the binding of anti-bovine IgG to bovine IgG patterned on the surface.[46] Luo et al. utilized pneumatic valve microfluidic device to pattern an array of gold patches with antibodies.[47] A 96-component array was fabricated using this approach. Krishnamoorthy et al. used electrokinetic flow focusing on a SPR imaging surface to selectively deliver samples over a single row of an array.[48] This label-free platform in microfluidics achieves sufficient lateral resolution enabling multiplexing. However in all of these examples, additional strategies such as microvalves, flow focusing or gold pattern fabrication were required for multiplexed detection.

4.3.7 WGM integrated in microfluidic devices

There has been a demonstration of WGM resonators used in a microfluidic platform by Keng et al.[17] The group placed a microsphere held by a capillary stem in a microfluidic cell molded from silicone. A thin fiber optic was placed near the resonator to couple light into the structure. After the microsphere and fiber optic was aligned for WGM detection, to enclose the microfluidic device, silicone was molded over the capillary stem and fiber optic to create a fluidic seal. Though this device was capable of detection in a small volume system capable of detection down to single particle levels, where Brownian motion of polystyrene particles were measured, the limited flexibility in the fabrication of the device is a major drawback in most microfluidic devices.[17] Instead it would be ideal for WGM resonators to be integrated in a less obstructive design. Here, we show several prototypes of microfluidic devices for the integration of a WGM microsphere detector.

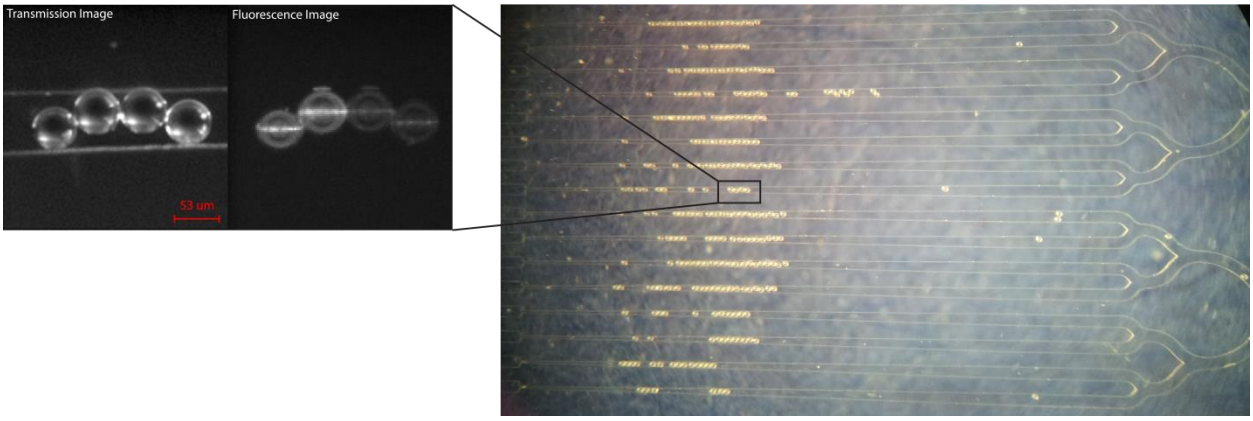

Figure 4.12. The 16-channel microfluidic device is shown on the right where each channel tapers from a 100 um widths, on the right side, down to 1 um, on the left side. The tapering design enables 53 um microspheres to be placed within the channel for detection. The inset is a magnified view of one of these channels of both transmission and fluorescence image of the microspheres. The enhanced ring of fluorescence indicates a WGM resonance used for refractive index sensing.

Figure 4.12 is an image of a 16-channel microfluidic device. All of the channels have a common inlet which then splits into 16, 100 µm wide, channels. Each channel narrows gradually towards the

outlet to a width of ~1 µm. The tapering of the channels holds the microspheres along the channel. The stability provided by the narrowing microfluidic walls hold the spheres firm during flow injections. Each channel can be loaded by controlling the outlet pressure, where one can envision the placement of 16 different antibody coated microspheres addressed to their respective channels. Scattering WGM was a slight challenge due to the scattering of light by the PDMS surfaces. Thus, WGM resonances were visualized using fluorescently labeled spheres as shown in the inset of **Figure 4.12.**

Another prototype including WGM resonators is shown in **Figure 4.13** where a diamond well placed at the end of a single microfluidic channel of a T-microchip design is used to hold a microsphere. These designs are used for microchip-electrophoresis for the separation of primary amines, oxidative stress biomarkers and cell lysate material.[40,44] WGM microspheres placed at the end of the channel can serve as a general detection scheme. This can have applications as a detector for microchip capillary electrophoresis where

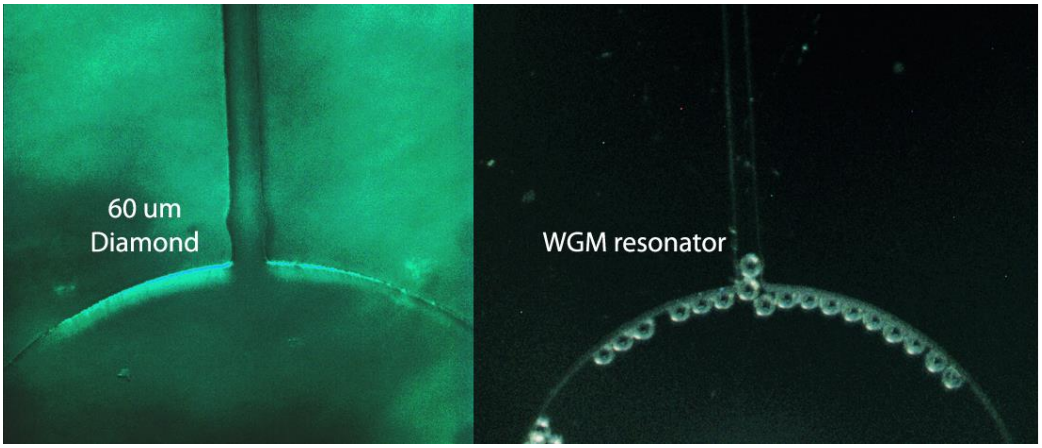

Figure 4.13. (left) A PDMS chip with a 60 um wide diamond-shaped well was fabricated at the end of a microfluidic channel. (right) A 53 um WGM resonator is placed into the diamond well for WGM detection.

First, the demonstration of refractive index detection in a microfluidic design, as shown in **Figure 4.13,** respond to changes in refractive index as resonance shifts when solutions of water and 5% ethanol were delivered through the microfluidic channels (data summarized in **Table 4.2**).

Table 4.2. The resonant wavelength in both water and 5% ethanol solution were measured and recorded below. A change of roughly 0.001 RIU corresponds to a resonant shift of 29 pm leading an estimated sensitivity of 20.7 nm/RIU

	Water	5% Ethanol
Refractive Index (RIU)	1.333	1.334
Resonant wavelength (nm)	633.035	633.064
Quality Factor	6922	
Projected sensitivity	20.7 nm/RIU	

The ease with which microspheres can be placed in microfluidics allows WGM detection in a variety of microfluidic channel designs. These initial results hold significant promise for WGM resonators as sensitive, flexible and low-cost detectors in microfluidic devices.

4.3.8 WGM detection for droplet microfluidics

Droplet microfluidics (DMF) is an emerging type of microfluidics that facilitates the transport of discrete droplets of fluid across the surface of an array of electrodes.[49,50] Electrowetting properties of fluids allow the precise positional control of micron-sized fluids within a device. When a voltage is applied, the surface tension of the liquids decreases leading to lower contact angles. These instantaneous changes in surface tension can propel droplets to selected locations useful for mixing, merging and directing fluid droplets.[49,51] Jebrail et al. outlines the typical fabrication process, starting with plate coated thinly with chromium.[52] Photolithography and etching process creates the electrode patterns similar to those illustrated in **Figure 4.14**.

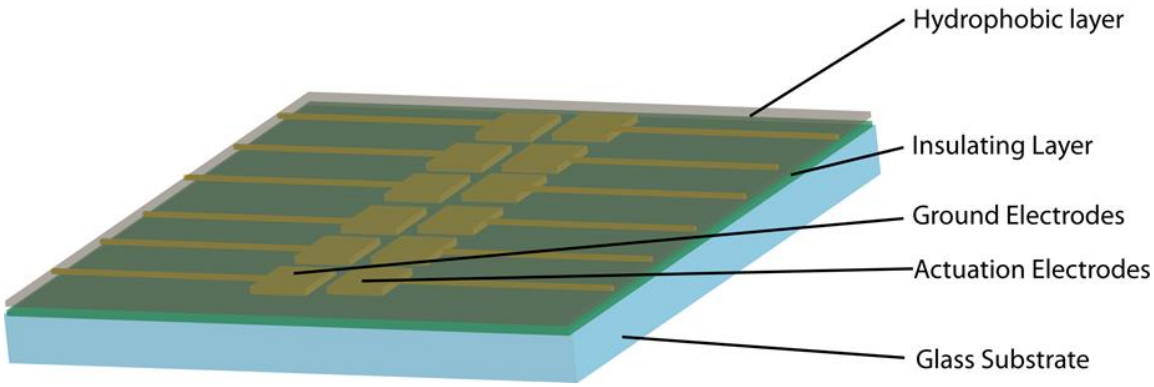

Figure 4.14. Schematic of a Digital Microfluidic Device. A glass substrate with actuation and ground electrodes fabricated on its surface is coated with an insulating layer and a hydrophobic layer.

A film ~2.5 µm of Parylene-C is then vapor deposited on top of the patterned electrodes to serve as an insulator. To create a hydrophobic surface for facile droplet movement, Teflon-AF is spin coated to a thickness of ~50 nm. These materials provide the best insulating and hydrophobic qualities for a robust system.[52] However more commonly attainable material such as Saran wrap (insulating film) and Rain-X (hydrophobic coating) can be utilized as DMF devices as shown in **Figure 4.15**. This device was initially tested for droplet actuation across several contact pads.

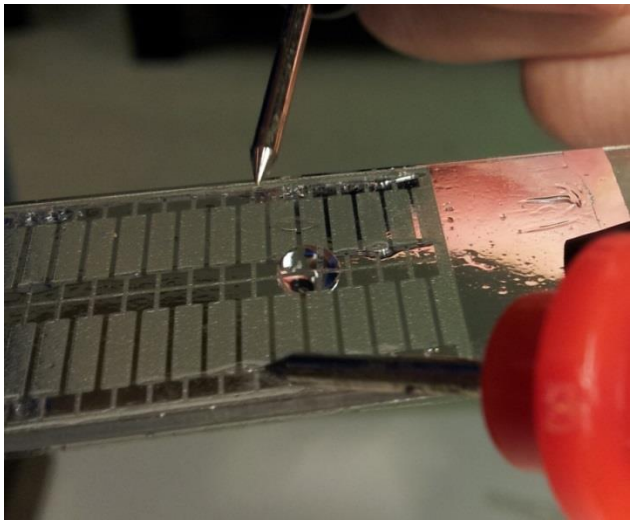

Figure 4.15. An image of a digital microfluidic device fabricated using aluminum electrodes, silicon oil, Saran wrap and Rain-X for the actuation of an uL aqueous droplet.

Droplets actuated in an open platform require higher potentials applied across the electrodes. Higher voltages lead to heating within the droplet eventually causing evaporation of droplet fluids. To minimize this, voltages were applied in short 1 second intervals. This allowed for sufficient forces required for fluids to glide across towards neighboring electrode pads while minimizing droplet evaporation. The devices showed reproducibility of droplet actuation in an open air configuration where the films of the device would damage after ~5 to 10 actuation voltages applied. Longer lasting devices were fabricated instead using Teflon AF coated surfaces which improved the device lifespan.

DMF devices employ similar detection strategies as microfluidics where fluorescence is most commonly used. Initial results using tapered fiber WGM microsphere measurements, described previously in 4.3.2, demonstrate the potential of droplet analysis in an effort to integrate a label-free detection system in DMF devices. Applications of this device can enable a true "lab-on-a-chip," where whole blood spots can be measured.[31,52]

Currently, DMF devices have been used to measure amino acid concentrations in dried blood spots.[52] Blood from newborn were introduced into the device. Once samples were loaded, all of the extraction and analysis were performed on-chip. Offline MS/MS and fluorescence detection methods were employed to measure methionine, phenylalanine and tyrosine in concentrations of tens of μM.[52] Label-free sensing via WGM resonators has the potential to enable lower detection limits coupled with all the inherent advantages of droplet analysis in DMF devices. Coupling WGM detectors with microfluidic or digital microfluidics for immunoassays requires continuous or repeated monitoring of WGM resonance. While WGM imaging allows the tracking of multiple sensors simultaneously, the use of the dye as a resonance reporter as described previously can have limited use for these applications. Photobleaching of the dye, used as a resonance reporter over the course of long measurements, is a challenge. Additionally, chapter 3 measured decreased quality factors as a result of increased dye

concentrations which can limit sensor performance. Therefore, for future microfluidic applications, the proposed evanescent wave scattering signals will be utilized.

4.4 Conclusions

In conclusion, a wide investigation of WGM resonator platform for sensing was performed. Light coupling gap distance between the resonator and its coupling surface was explored. Here we showed that refractive index matched film such as AL-2233 can be used as an optical gap to improve quality factors for a field a spheres. In another effort to improve quality factors, a fiber light coupled WGM system was introduced. Additionally, the discussed fiber light coupled WGM system with utility as dip sensors for modular, point of care sensing. Alongside these developments, WGM resonators were integrated to digital microfluidic and PDMS microchannels devices for more automated fluidic implementation. We envision that the fiber-WGM device is well-suited as droplet sensors for digital microfluidic devices where detection schemes are largely limited to labeled detection platforms. Opportunities for WGM resonators within PDMS microchannels were initially explored, where the small footprint and flexibility of WGM resonators can be used for sensitive, label-free detection for these devices. Finally, the development of a scattering WGM detection scheme with automated analysis promises high throughput, longer lasting, sensitive and low cost platform for the development of a clinical diagnostic.

4.5 References

1. Huckabay, H. A., et al. Whispering gallery mode imaging for the multiplexed detection of biomarkers. *Sens. Actuators, B* **2011**, *160*, 1262-1267.
2. Kim, D. C., et al. Integration of microsphere resonators with bioassay fluidics for whispering gallery mode imaging. *Analyst* **2013**, *138*, 3189-3195.
3. Khaled, E. E. M., et al. Near-resonance excitation of dielectric spheres with plane waves and off-axis Gaussian beams. *Applied optics* **1992**, *31*, 1166-1169.
4. Barton, J., et al. Internal and near-surface electromagnetic fields for a spherical particle irradiated by a focused laser beam. *Journal of Applied Physics* **1988**, *64*, 1632-1639.
5. Ward, J., et al. WGM microresonators: sensing, lasing and fundamental optics with microspheres. *Laser & Photonics Reviews* **2011**, *5*, 553-570.
6. Vernooy, D., et al. Cavity QED with high-Q whispering gallery modes. *Physical Review A* **1998**, *57*, R2293.
7. Tien, P. K., et al. Theory of Prism–Film Coupler and Thin-Film Light Guides. *J. Opt. Soc. Am.* **1970**, *60*, 1325-1337.
8. Ahmad, M., et al. Effect of taper geometries and launch angle on evanescent wave penetration depth in optical fibers. *Biosensors & bioelectronics* **2005**, *20*, 1312-1319.
9. Yariv, A. Critical coupling and its control in optical waveguide-ring resonator systems. *IEEE Photonics Technology Letters* **2002**, *14*, 483-485.
10. Iqbal, M., et al. Label-free biosensor arrays based on silicon ring resonators and high-speed optical scanning instrumentation. *Selected Topics in Quantum Electronics, IEEE Journal of* **2010**, *16*, 654-661.
11. Menon, V., et al. Control of quality factor and critical coupling in microring resonators through integration of a semiconductor optical amplifier. *Photonics Technology Letters, IEEE* **2004**, *16*, 1343-1345.
12. Cai, M., et al. Observation of critical coupling in a fiber taper to a silica-microsphere whispering-gallery mode system. *Physical review letters* **2000**, *85*, 74.
13. Vahala, K. J. Optical microcavities. *Nature* **2003**, *424*, 839-846.
14. Vollmer, F., et al. Protein detection by optical shift of a resonant microcavity. *Appl. Phys. Lett.* **2002**, *80*, 4057-4059.
15. Vollmer, F., et al. Multiplexed DNA quantification by spectroscopic shift of two microsphere cavities. *Biophys. J.* **2003**, *85*, 1974-1979.
16. Chiasera, A., et al. Spherical whispering-gallery-mode microresonators. *Laser Photonics Rev.* **2010**, *4*, 457-482.
17. Keng, D., et al. Resonance fluctuations of a whispering gallery mode biosensor by particles undergoing Brownian motion. *Applied Physics Letters* **2007**, *91*, 103902.
18. Agarwal, M., et al. Whispering gallery mode dip sensor for aqueous sensing. *Analytical Chemistry* **2015**, *87*, 10600-10604.
19. Schartner, E. P., et al. Driving down the Detection Limit in Microstructured Fiber‐Based Chemical Dip Sensors. *Sensors* **2011**, *11*, 2961-2971.
20. Prieve, D. C., et al. Scattering of an evanescent surface wave by a microscopic dielectric sphere. *Applied optics* **1993**, *32*, 1629-1641.
21. Bike, S. G. Measuring colloidal forces using evanescent wave scattering. *Current opinion in colloid & interface science* **2000**, *5*, 144-150.
22. Bike, S., et al. Measurements of double-layer repulsion for slightly overlapping counterion clouds. *International Journal of Multiphase Flow* **1990**, *16*, 727-740.

23. Prieve, D. C., et al. Total internal reflection microscopy: a quantitative tool for the measurement of colloidal forces. *Langmuir* **1990**, *6*, 396-403.
24. Suresh, L., et al. Direct measurement of the effect of surface roughness on the colloidal forces between a particle and flat plate. *Journal of colloid and interface science* **1997**, *196*, 177-190.
25. Sober, D., et al. Measurement of long range depletion energies between a colloidal particle and a flat surface in micellar solutions. *Langmuir* **1995**, *11*, 2352-2356.
26. Rudhardt, D., et al. Direct measurement of depletion potentials in mixtures of colloids and nonionic polymers. *Physical review letters* **1998**, *81*, 1330.
27. Haughey, D., et al. Studies of colloidal interactions using total internal reflection microscopy. *Colloids and Surfaces A: Physicochemical and Engineering Aspects* **1998**, *136*, 217-230.
28. Huckabay, H. A., et al. Label-free detection of ovarian cancer biomarkers using whispering gallery mode imaging. *Biosens. Bioelectron.* **2013**, *45*, 223-229.
29. Streets, A. M., et al. Chip in a lab: Microfluidics for next generation life science research. *Biomicrofluidics* **2013**, *7*, 011302.
30. Choi, K., et al. Digital microfluidics. *Annual review of analytical chemistry* **2012**, *5*, 413-440.
31. Shamsi, M. H., et al. A digital microfluidic electrochemical immunoassay. *Lab Chip* **2014**, *14*, 547-554.
32. Khandurina, J., et al. Bioanalysis in microfluidic devices. *Journal of Chromatography A* **2002**, *943*, 159-183.
33. Anderson, J. R., et al. Fabrication of microfluidic systems in poly (dimethylsiloxane). *ELECTROPHORESIS* **2000**, *21*, 27-40.
34. Abgrall, P., et al. Lab-on-chip technologies: making a microfluidic network and coupling it into a complete microsystem—a review. *Journal of Micromechanics and Microengineering* **2007**, *17*, R15.
35. Zhang, C., et al. PCR microfluidic devices for DNA amplification. *Biotechnology advances* **2006**, *24*, 243-284.
36. Khandurina, J., et al. Integrated system for rapid PCR-based DNA analysis in microfluidic devices. *Analytical Chemistry* **2000**, *72*, 2995-3000.
37. Krüger, J., et al. Development of a microfluidic device for fluorescence activated cell sorting. *Journal of Micromechanics and Microengineering* **2002**, *12*, 486.
38. Wang, X., et al. Enhanced cell sorting and manipulation with combined optical tweezer and microfluidic chip technologies. *Lab Chip* **2011**, *11*, 3656-3662.
39. Dittrich, P. S., et al. Lab-on-a-chip: microfluidics in drug discovery. *Nature Reviews Drug Discovery* **2006**, *5*, 210-218.
40. Gawron, A. J., et al. Microchip electrophoretic separation systems for biomedical and pharmaceutical analysis. *European journal of pharmaceutical sciences* **2001**, *14*, 1-12.
41. Roman, G. T., et al. Fully integrated microfluidic separations systems for biochemical analysis. *Journal of Chromatography A* **2007**, *1168*, 170-188.
42. Wu, D., et al. Electrophoretic separations on microfluidic chips. *Journal of Chromatography A* **2008**, *1184*, 542-559.
43. Paegel, B. M., et al. Microfluidic devices for DNA sequencing: sample preparation and electrophoretic analysis. *Current opinion in biotechnology* **2003**, *14*, 42-50.
44. Metto, E. C., et al. An integrated microfluidic device for monitoring changes in nitric oxide production in single T-lymphocyte (jurkat) cells. *Analytical Chemistry* **2013**, *85*, 10188-10195.
45. Lim, C., et al. Bead-based microfluidic immunoassays: the next generation. *Biosensors & bioelectronics* **2007**, *22*, 1197-1204.
46. Kanda, V., et al. Label-free reading of microarray-based immunoassays with surface plasmon resonance imaging. *Analytical Chemistry* **2004**, *76*, 7257-7262.

47. Luo, Y., et al. Microfluidic device for immunoassays based on surface plasmon resonance imaging. *Lab Chip* **2008**, *8*, 694-700.
48. Krishnamoorthy, G., et al. Integrated electrokinetic sample focusing and surface plasmon resonance imaging system for measuring biomolecular interactions. *Analytical Chemistry* **2009**, *81*, 1957-1963.
49. Pollack, M. G., et al. Applications of electrowetting-based digital microfluidics in clinical diagnostics. *Expert review of molecular diagnostics* **2011**, *11*, 393-407.
50. Cho, S. K., et al. Electrowetting on dielectric (EWOD): new tool for bio/micro fluids handling. *Biochip Journal* **2008**, *2*, 79-96.
51. Wheeler, A. R. Putting electrowetting to work. *Science* **2008**, *322*, 539-540.
52. Jebrail, M. J., et al. A digital microfluidic method for dried blood spot analysis. *Lab Chip* **2011**, *11*, 3218-3224.

4.6 Appendices

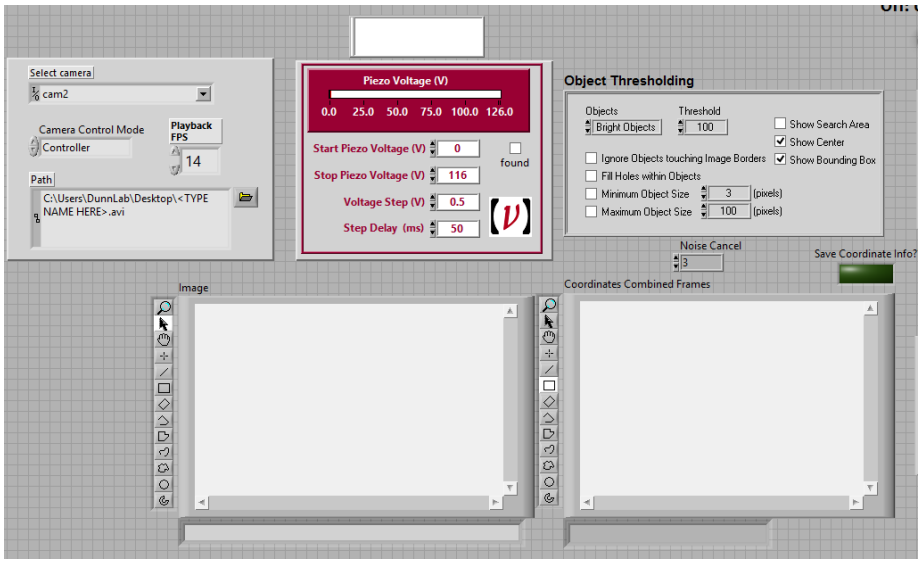

Appendix 1 – The front panel of the LabView File: Scattering Analysis Program v2.vi. The camera is initialized and is coordinated with the laser tuning such that each laser tuning increment results in an captured image. Then the object thresholding portion addresses each scattering WGM spot for subsequent analysis.

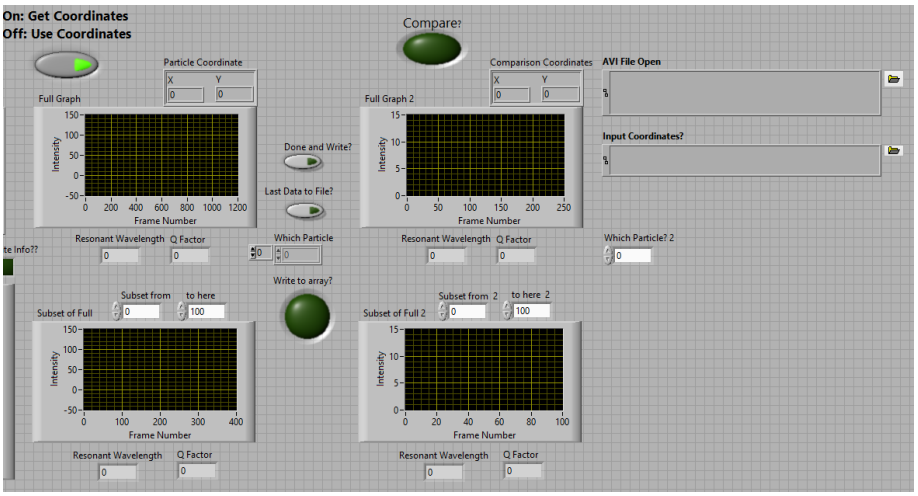

Appendix 2 – This portion displays data from the analysis portion and shows a Gaussian peak fit for identification of the resonant wavelength. Quality factor is also calculated and displayed here. A feature of this program is that previously recorded video images can be reopened concurrently to compare data shifts.

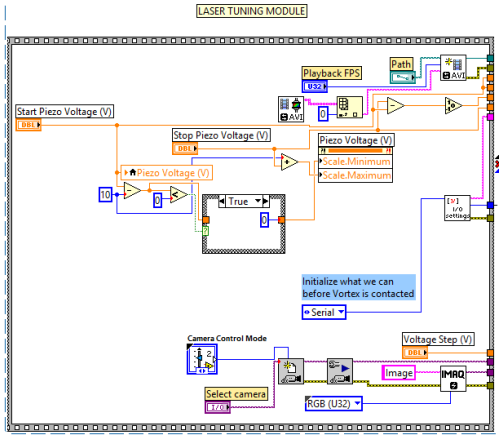

Appendix 3 – This code portion shows the laser tuning module where the computer pairs with tunable laser controller. The camera is also initialized here simultaneously.

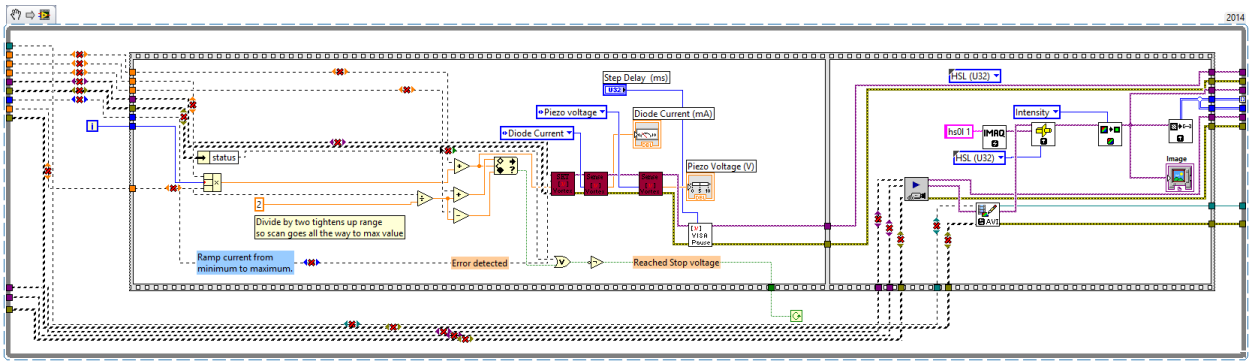

Appendix 4 – This loop shows how the laser is tuned in increments. Immediately after the piezo voltage is increased the camera captures an image then compiles the image into a stack of images.

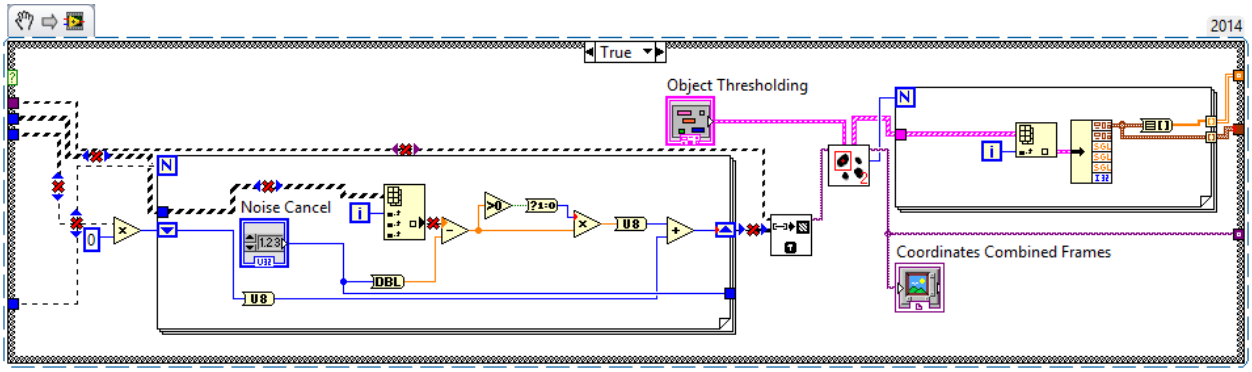

Appendix 5 – This loop identifies and addresses each scattering spot in the field of view for subsequent data analysis.

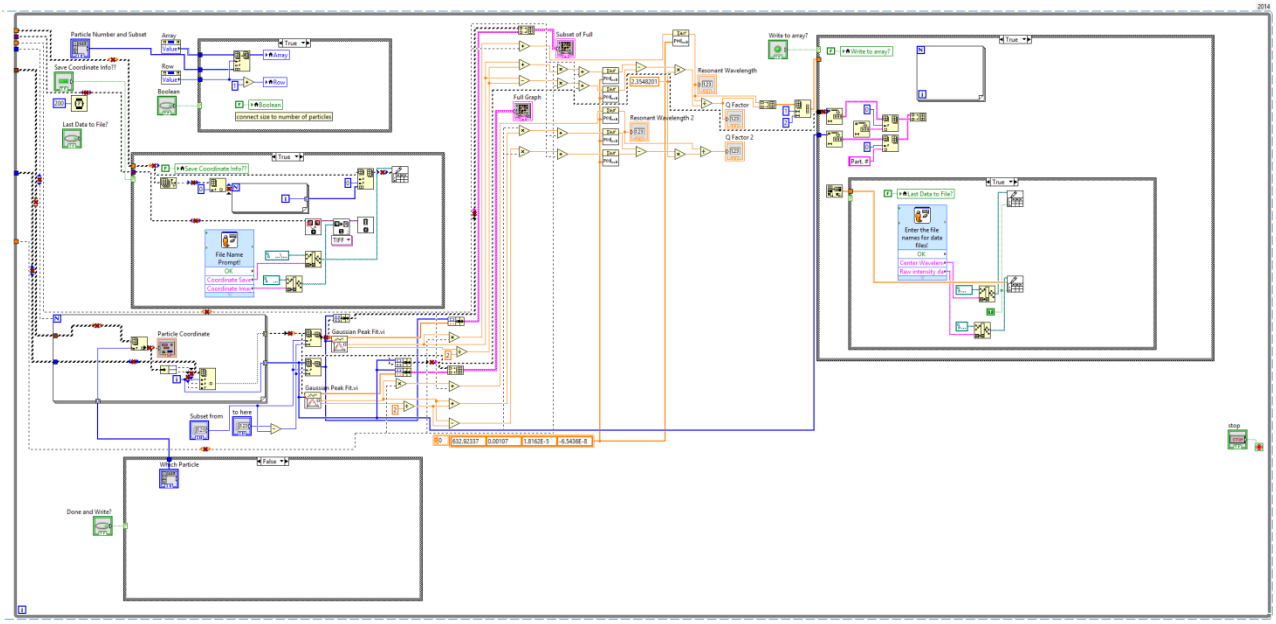

Appendix 6 – This portion is analyzes and records each WGM spectra and also calculates the best Gaussian peak fit. The data obtained can be adjusted to narrow the tuning range to focus on a particular peak of interest. The final data set the user would like to save is recorded into a .txt format which can be transferred into an excel spreadsheet.

Chapter 5

WGM Refractive Index Sensing with CE Separations using Phase Detection

5.1 Introduction

5.1.1 Introduction to capillary electrophoresis

Capillary electrophoresis (CE) achieves rapid, high-resolution separations for a broad class of analytes based largely on differences in mass-to-charge ratio. There are a host of CE techniques such as capillary zone electrophoresis (CZE), capillary gel electrophoresis (CGE), micellular electrokinetic capillary chromatography (MEKC) and capillary isoelectric focusing (CIEF).[1,2] The versatility, small sample volumes required, large plate numbers, and relative simplicity of the equipment have made CE a popular choice for many analytical challenges. Applications in clinical analysis[3,4], environmental monitoring[5,6], and proteomics[5,7] have all exploited the useful characteristics of CE to efficiently separate species of interest.[3,7-9] Here, we will briefly discuss the fundamentals of CE and present opportunities for WGM resonators as a refractive index detector compatible with CE.

5.1.2 Electrophoretic mobility

In electrophoresis, sample ions move in the presence of an electric field based on their electrophoretic mobility. The term electrophoretic mobility, μ_{EM}, describes the magnitude of force that

the ion will experience based on their net charge, and translation friction coefficient as shown in **Equation 5.1**:[10]

$$\mu_{EM} = \frac{q}{f} = \frac{q}{6\pi\eta r} \qquad \text{Equation 5.1}$$

where q is the net charge, f is the translational friction coefficient for a small sphere given by Stokes' law, η is the viscosity of the solvent and r is the hydrated radius. The rate at which these ions migrate is dictated by their charge to hydrated radius or more simply, charge to size ratio. Each sample ion exhibits velocities that are equal to the product of their electrophoretic mobility and electric field strength as shown in **Equation 5.2**:[10]

$$v = \mu_{EM} * E$$

where v is the velocity and E is the electric field. Therefore, sample ions can be separated by exploiting their differences in electrophoretic mobilities.

5.1.3 Electroosmotic flow

To perform electrophoresis experiments, a channel is filled with an electrolyte buffer followed by a small sample injection, which are then separated. This is achieved by applying a voltage across the channel to produce electroosmotic flow (EOF). The chemical makeup of the channel surface is typically glass and silica which, at buffer pH greater than 3, generate negatively charged surfaces due to the ionization of the silanol groups. The negatively charged walls electrostatically attract cations to its surface due to its potential field. At a certain potential, called the zeta potential, cations adhere to the surface creating an absorbed layer.

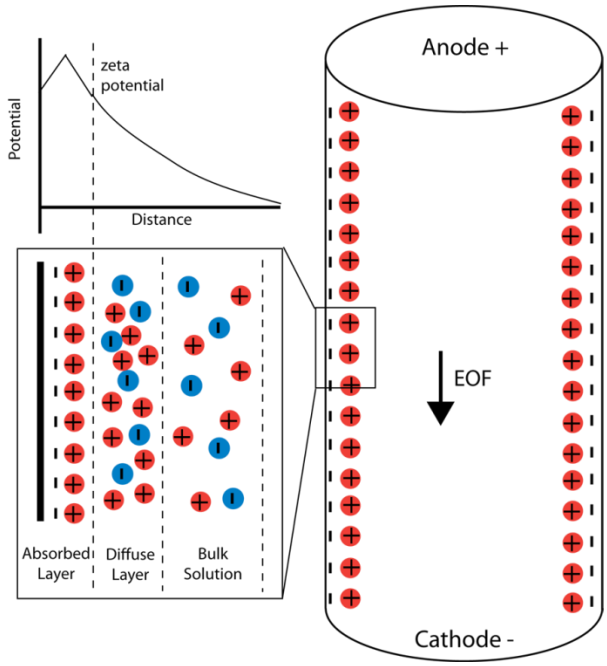

Figure 5.1. A capillary containing buffer solution creates an electric double layer as a result of zeta potential distributions. The inset shows a magnified view of the electric double layer.

There also exists a second diffuse layer that is closely associated with the surface in an attempt to neutralize the negatively charged walls. This results in an electrical double layer where the absorbed layer is fixed and the diffuse layer is mobile shown in **Figure 5.1**. When an electric field is applied to the system the positively charged ions in the diffuse layer are drawn towards the cathode creating a bulk flow that moves all analytes regardless of their charge. This EOF exhibits a plug flow profile that is significantly flatter towards the center with a slight drag along the walls. Laminar flow has a parabolic distribution of flow velocities where the flow at the walls is significantly slower than the flow in the center of the channel. EOF however has a flat flow velocity profile resulting in less broadening as shown in **Figure 5.2**. Capillary electrophoresis use the flat flow profile EOF and differences in sample ion electroosmotic mobilities to efficiently separate ions in small volume (nL) systems.

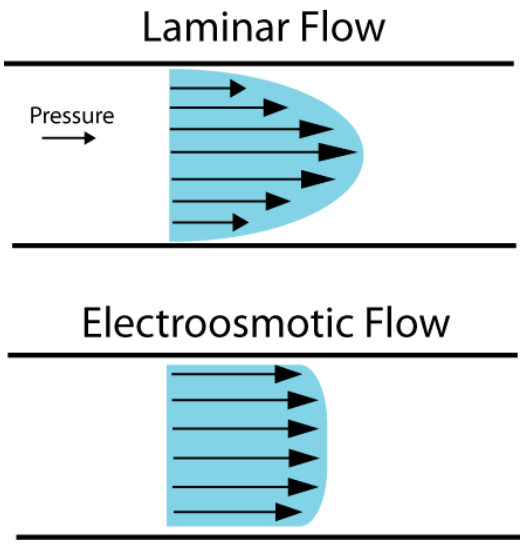

Figure 5.2. Illustration of laminar and EOF flow velocities. EOF exhibits a flatter flow profile compared to laminar flow.

5.1.4 Refractive index sensing in CE

Since the introduction of capillary electrophoresis, a number of detection schemes have been developed to quantitate analyte bands separated in CE. The choice of detection scheme is dictated by the nature of the analytes and the required performance metrics. The most popular method uses UV absorbance measurements. UV detection is easily integrated, inexpensive, and generally applicable.[11] For improved detection limits, methods based on fluorescence can be implemented but requires either an intrinsic fluorophore or additional sample derivatization steps.[12] Likewise, electrochemical detection has been widely employed for its favorable specificity and sensitivity, but requires electro-active species.[13]

Refractive index (RI) sensing, on the other hand, provides a general detection method that is widely applicable for measuring the separation of ions, small molecules, or biomolecules.[14-22] RI detection is concentration sensitive, non-destructive, and can detect species lacking strong UV absorption features. While developed largely for liquid chromatography, CE applications using RI detection have been reported using a variety of techniques. Most approaches use some form of

interferometry given its exquisite detection metrics, but other methods such as surface plasmon resonance (SPR) have also been reported.[19] These approaches offer detection limits with reported values ranging from 10^{-5} to 10^{-8} RIU (refractive index units).[14,17-19,21]

With a notable exception[17], the figures of merits for these approaches are often highly dependent on the inner diameter of the capillary or require modifications to the capillary such as removing the protective coating (interferometry) or introducing a break to shunt current (SPR).[15,19,23] Here we explore the use of small-footprint RI sensors integrated with CE to develop an end-capillary detector that does not require modifications of the capillary, has low detection limits, and is easily modified for specific sensing applications.

5.1.5 WGM detectors for separation systems

Whispering gallery mode (WGM) resonators are small spherical dielectric structures that confine light through continuous total internal reflection. Light evanescently coupled into a WGM resonator is efficiently recirculated when the resonance condition as previously described by **equation 2.3**.[24-26] As seen in this equation, WGM resonances shift in response to changes in surrounding refractive index. Moreover, despite their small size, WGM resonators have a long effective sensing pathlength as light recirculates within these high-Q resonators. We and others have reported the utility of WGM resonators for biosensing, where the resonator surface is functionalized for the specific detection of proteins or oligonucleotides.[27-31] However, less has been reported using WGM sensors for bulk refractive index measurements in analytical separations.

5.1.5.1 Liquid core optical ring resonator for Capillary Flow

A unique on-column WGM detector was introduced by Fan and coworkers using tapered capillaries with thinned walls capable of supporting WGM resonances.[20] The capillary wall thickness was

etched to less than 10 µm to enable circulating light to sense RI changes in the fluid interior. Using this liquid core optical ring resonator (LCORR) arrangement, electrosmotic flow (EOF) was used to drive neutral glycerol plugs through the thinned capillary section where changes in the WGM resonance were monitored. Estimated detection limits of 10^{-6} RIU were reported based on glycerol calibration curves and noise experiments performed separately.[20] This impressive demonstration showed the promise of coupling WGM detection with CE; however, the tapering and chemical etching required produces highly specialized and fragile capillaries.

5.1.5.2 Microring resonators as a detector for Liquid Chromatography

More recently, Bailey and coworkers integrated WGM detection with HPLC using microfabricated microring resonators.[21] Using this robust coupling, they detected the separation of ibuprofen and simvastatin using gradient elution. Non-isocratic separations are challenging for refractive index detection since changes in run buffer refractive index leads to complicated backgrounds. The large dynamic range (0.1 RIU), however, enabled peak detection despite the complicated background with a reported detection limit of 1.5 x 10^{-6} RIU using a commercialized system.[21]

5.1.6 Opportunities for microsphere based WGM in capillary electrophoresis

The small footprint of WGM resonators and their universal refractive index sensing is well suited for integration with the small-bore capillaries used in CE. Here we show that easily implemented end-capillary geometry enables WGM resonators to be coupled with CE using unmodified, commercially available capillaries. This flexible geometry also enables simultaneous on-column UV detection to help validate the approach and optimize detection metrics. This approach will be especially useful for future biosensing applications where surface functionalized WGM resonators specifically detect and quantify species eluting from the capillary.

Using WGM resonators for bulk refractive index sensing, as required for a general separation detector, can lead to modest detection limits. This is in contrast with biosensing, where specific recognition elements on the WGM resonator surface concentrate analytes in the evanescent field, thus maximizing response. Similar challenges have been discussed when integrating SPR detection with CE.[19] To begin addressing this analytical challenge, we introduce a modulation approach using phase sensitive detection to measure small shifts in the WGM resonance. This approach enables real-time monitoring of WGM resonance shifts using phase sensitive detection, improving both analysis time and signal-to-noise. Using this scheme, detection limit improvements of two orders of magnitude is observed when directly compared to traditional WGM resonance tracking measurements. The utility of PS-WGM detection as a real-time, low detection limit detection scheme is demonstrated through the CE separation of the non-UV absorbing ions: sodium, lithium, and potassium.

5.2 Materials and methods

5.2.1 WGM Resonator Measurement

The output from a tunable diode laser (Vortex II TLB-7004, <500 kHz linewidth, 160 GHz mode-hop free tuning, New Focus, Santa Clara, CA) centered at 633.020 nm is focused into a Dove prism (Edmund Optics, Barrington, NJ). Light entering the Dove prism is directed towards a glass substrate at an angle leading to total internal reflection. The associated evanescent field excites resonances in 53 µm barium titanate resonators (53 µm ± 3% diameter, MO-SCI, Rolla, MO) on the glass substrate surface as shown in **Figure 5.3a**.

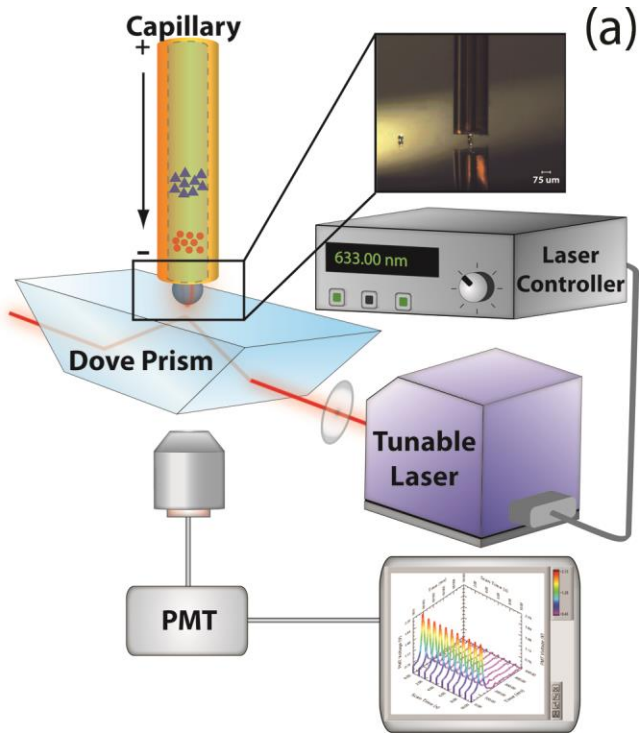

Figure 5.3. Schematic showing end-capillary WGM refractive index sensing coupled with CE. The output of a CE capillary (75 µm I.D., 363 µm O.D.) is positioned above a 53 µm diameter WGM resonator as shown in the inset. To monitor shifts in the WGM resonance as analyte bands elute from the capillary, light from a tunable diode laser is directed into a Dove prism, creating an evanescent field that couples light into the resonator. As the excitation wavelength of the laser is scanned, scattered light from the resonator is collected from below and detected on a PMT.

A microwell on the substrate surface confines the resonator in ≈500 µL of run buffer as shown in **Figure 5.3**. Evanescently scattered light from the resonator is collected from below using a 10X objective (Olympus UMPlanFL NA=0.3, Center Valley, PA) and detected on a photomultiplier tube.

5.2.2 Capillary Electrophoresis/WGM Interface

WGM detection was integrated with capillary electrophoresis (CE) using a custom-built apparatus. The inlet of the 70 cm (unless otherwise specified) CE capillary (75 µm I.D., 363 µm O.D.; PolyMicro Technologies, Phoenix, AZ) was equipped with a T-valve connected to a custom pressure injection system with 0.01 second accuracy. The outlet of the capillary was held in a *xyz* micromanipulator (Model A LHFF, Line Tool Co., Allentown, PA) to precisely position it above a WGM

resonator. The capillary outlet partially surrounds the resonator on the glass surface and helps hold it in place. Further procedures to immobilize the resonator on the surface were not required. Electroosmotic flow was driven with a high voltage power supply (Spellman CZE1000R, Valhalla, NY) connected through molybdenum wires running parallel to both the inlet and outlet of the capillary as shown in **Figure 5.4**.

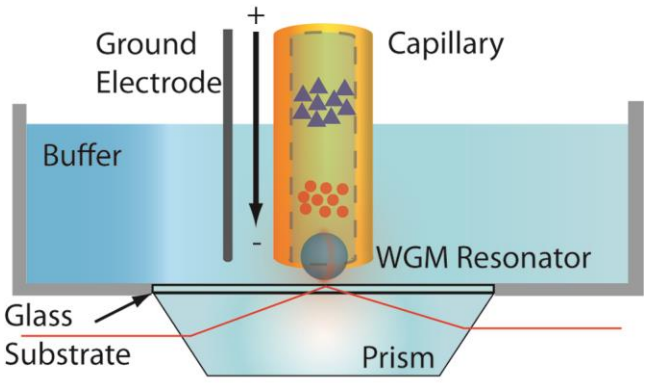

Figure 5.4. Schematic of the fluid volume and electrical connections used for CE separations. The ground electrode runs parallel to the capillary which encapsulates the WGM resonator. The effluent interacts with the resonator as it flows past and diffuses into the 500 µL buffer reservoir.

For all separations, UV detection (SpectraSYSTEM UV1000, ThermoScientific, San Jose, CA) was also implemented using a window created 50 cm from the capillary inlet by removing the capillary coating. Sucrose solutions of concentrations ranging from 0.02% to 20% (2.7 mM to 2.8 M) were used to test flow profiles of this interface.

5.2.3 WGM Spectral Shift Detection

A triangle waveform from a function generator (BK Precision 3011; Yorba Linda, CA) is used to scan the tunable diode laser. For spectra collection, the clock signal from the function generator synchronizes PMT data collection (NI USB-6251 DAQ, National Instruments) using an in-house LabView program. The LabView code is provided in the appendix at the end of this chapter. Spectra as a function of time are collected and fit to a Lorentzian lineshape to extract peak wavelengths.

5.2.4 Phase Sensitive WGM Detection (PS-WGM)

To track WGM resonances using phase sensitive detection, the laser wavelength is modulated with the triangle wave over its entire tuning range (632.920 nm to 633.120 nm) at 215 Hz. The output of the PMT is sent to a track-and-hold circuit (Mattson Mini Modular Model: SH1-B), which is triggered to hold the last valued received by the PMT before the down scan of the triangle wave. This simplifies the measured spectrum to one peak per complete cycle. The output of the track-and-hold circuit is sent to a dual-channel lock-in amplifier (Stanford Research Systems SR830, Sunnyvale, CA) referenced to the laser modulation signal. The phase signal is detected which reflects spectral shifts of the WGM resonator with respect to the laser modulation. An in-house LabView program, code provided in the appendix, was used to communicate with the lock-in amplifier and record phase shifts in real-time.

5.2.5 Cation separation using UV and PS-WGM detection

To establish the validity of the PS-WGM as a detection scheme for routine capillary electrophoresis separations, a three cation separation system was adapted. The separation of the three ions was optimized on a 70 cm length capillary (75 μm I.D., 363 μm O.D.) with the UV detector positioned 50 cm from the capillary inlet. The ion mixture was pressure injected with a volume of 4.9 nL resulting in loadings of 22, 28 and 39 pmol (4.5 mM, 5.7 mM and 7.9 mM) of K^+, Na^+ and Li^+ ions respectively. For indirect UV detection, the pH 5 run buffer included 5 mM of UV absorbing imidazole. The high ionic strength of the imidazole raises concerns over Joule heating so the separation voltage was minimized to 24kV, below the measured nonlinear region of the Ohm's plot. Before each run, the capillary was thoroughly rinsed with at least three capillary volumes each of 0.1 M NaOH, water and the 5 mM imidazole run buffer. PS-WGM detection was done at the outlet (L_d = 70 cm) similar to previous configuration. Data for both UV and PS-WGM were collected simultaneously as described previously.

5.3 Results and discussion

5.3.1 CE-WGM Interface

The interface between a spherical whispering gallery mode (WGM) resonator and CE capillary is depicted in **Figure 5.3**. The magnified view, **Figure 5.4,** shows the relative size of the CE capillary (inner diameter 75 μm) and WGM resonator (53 μm diameter). Excitation light directed into a Dove prism leads to total internal reflectance at the sample interface, creating the evanescent field required to couple light efficiently into the WGM resonator. Light evanescently scattered from the resonator is collected from below and detected on a photomultiplier tube (PMT). As the excitation wavelength of the tunable diode laser is scanned, scattered intensity versus wavelength measures the WGM spectrum.

To align the CE capillary above the resonator, the capillary is held in a three-axis micromanipulator. WGM resonators are sensitive to changes in the surrounding refractive index (RI) and the relative position of the capillary outlet to the resonator affects how efficiently eluting analyte bands are sensed. While completely engulfing the resonator will maximize RI response, the obstruction leads to unacceptable back pressures which broaden the bands in the separation. To optimize the geometry, the capillary was gently lowered around the resonator until just contacting the substrate. The capillary was then moved away from the surface in ~10 μm increments, while the peak from a pressure plug of 5% NaCl solution was measured. For the particular capillary and resonator dimensions studied, optimal peak shape and resonator response was obtained with the capillary end positioned raised approximately 20-30 μm with respect to the glass substrate as shown schematically in **Figure 5.4**. The outlet of the capillary is immersed in a ~500 μL volume of buffer, which allows sufficient diffusion of the effluent leading to negligible effects on peak shapes.

5.3.2 CE-WGM and electroosmotic flow compatibility

WGM detection is compatible with the high voltages required to produce electroosmotic flow (EOF). The flow is sufficient to drive sample plugs past the detector resulting in reversible WGM spectral shifts. The sample plug profile was characterized as shown in **Figure 5.5**.

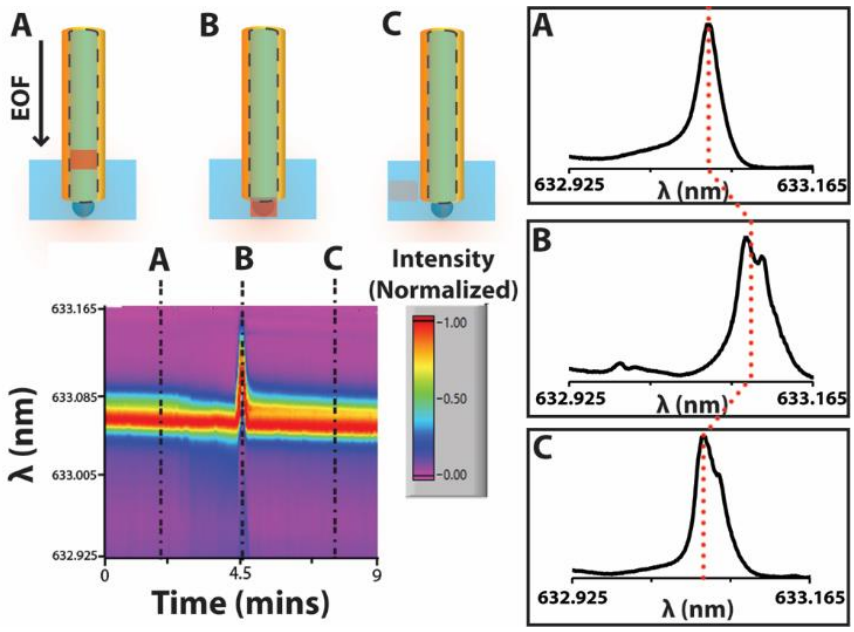

Figure 5.5. Reversible shift in WGM resonance as a 38 nL injection of 5% NaCl elutes from the capillary. The NaCl plug corresponds to a change of 8.7 x 10^{-3} RIU in the 5 mM imidazole run buffer and was driven by the EOF generated through a 30 kV applied potential as shown schematically in the upper left. The waterfall plot below shows the WGM spectra as a function of time collected every 0.5 s. Spectra extracted from the indicated locations illustrate the reversible shift in the WGM resonance as the plug elutes from the capillary.

A 5% NaCl solution was pressure injected at 5 psi for 1 second into a capillary filled with 5 mM imidazole buffer (pH 5). This was driven by EOF past the WGM detector using a 30 kV potential. The false color waterfall plot in **Figure 5.5** records the WGM spectrum as a function of time, collected at a rate of 2 Hz. A Gaussian plug profile is observed in the waterfall plot as the WGM spectra reversibly shifts in response to the migrating plug. Three representative spectra extracted from the indicated locations (A, B and C)

in the waterfall plot and displayed in the right of **Figure 5.5**, along with a schematic representation of the plug locations.

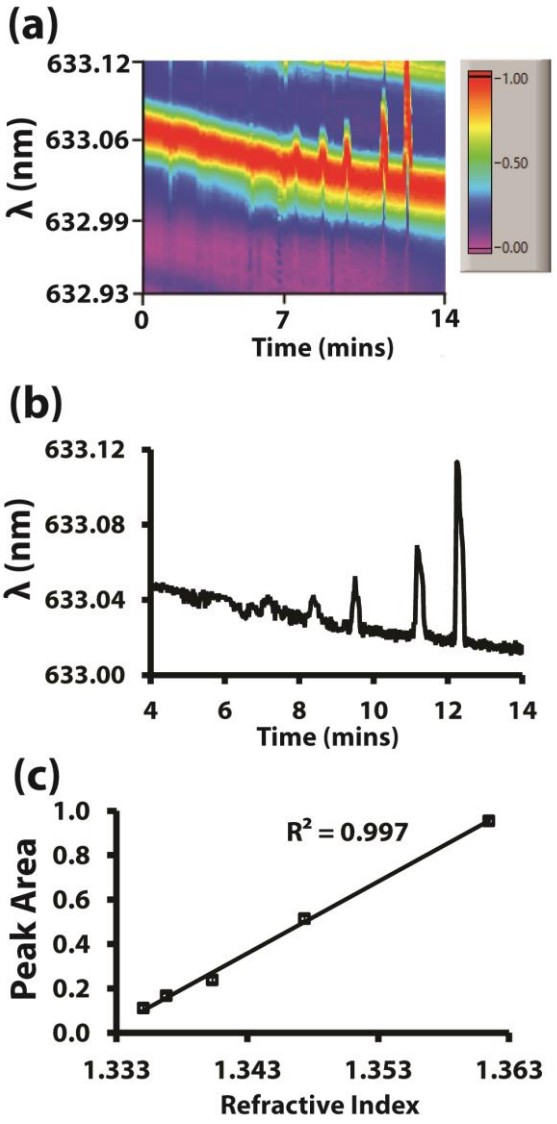

Figure 5.6. (A) WGM spectra as a function of time (0.5 s per spectrum) showing shifts from sequential injections of sucrose in increasing concentration (1%, 2.5%, 5%, 10% and 20%). Each injection volume of 22 nL in 5 mM imidazole buffer was driven past the WGM detector using the EOF from a 30 kV applied potential. (B) Each vertical slice from the waterfall plot is fit to a Lorentzian line shape to extract the peak wavelength, which is plotted as a function of time to generate an electropherogram. (C) The peaks in B are integrated and plotted versus RI of the sucrose solutions to generate the linear calibration plot. Propagation of the uncertainty in the peak height and width are used to calculate the error bars, which are within the points shown.

The linear response of WGM detection with increasing analyte concentration is shown in **Figure 5.6**. In this measurement, sucrose solutions of increasing concentration (1%, 2.5%, 5%, 10% and 20%)

were injected at 5 psi for 1 sec in approximately one minute intervals into the CE column. Injected volumes of approximately 22 nL in the 5 mM imidazole run buffer were driven with an EOF generated by a 30 kV potential. The electropherogram, shown in **Figure 5.6a,** contains five successive peaks with increasing spectral shift, corresponding to the increasing sucrose concentration. Each WGM spectra (vertical line-cut) in the waterfall plot (**Figure 5.6a**) is fit to a Lorentzian line shape to extract the peak wavelength at each time point. A plot of peak wavelength versus time is shown in **Figure 5.6b**. The electropherogram in **Figure 5.6b** is baseline adjusted and integrated to extract peak areas used to produce the linear calibration curve shown in **Figure 5.6c**. In these initial measurements, a small blue shift in the baseline arose from thermal drifts that were subsequently eliminated using longer equilibration times with the CE voltage on.

While these measurements illustrate the feasibility of coupling end-capillary WGM detection with CE, the approach outlined above results in modest detection limits. Characterizing the response with pressure plugs of both NaCl and sucrose at varying concentrations, we measure detection limits ranging from 1.3×10^{-4} to 7.6×10^{-5} RIU with the CE-WGM platform. These limits were measured using 8 different resonators with Q factors ranging from 10^4 to 10^5.

5.3.3 Phase Sensitive Detection for WGM Resonance Tracking

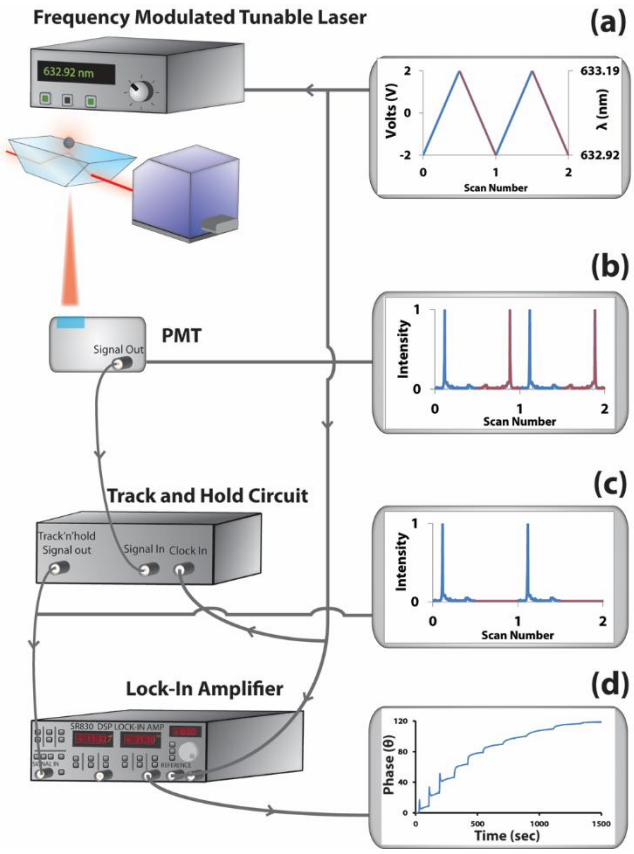

Figure 5.7. Schematic diagram showing the sequence used for phase sensitive detection of WGM resonances. (A) A triangular waveform from a function generator is used to modulate the wavelength from the tunable diode laser and provide the reference signal for the lock-in amplifier. (B) WGM resonances detected at the PMT exhibit mirror image peaks as the same resonance is detected on the up scan (blue) of the triangle wave and then again on the down scan (red) as the laser resets back to the starting wavelength. (C) The PMT output is sent to a track-and-hold circuit, triggered using the triangle wave, to eliminate the second peak in each cycle. The removal of the redundant peak results in one measured WGM resonance per modulation cycle, thus enabling spectral shifts to be quantified through changes in phase with respect to the laser modulation. (D) The simplified spectrum is sent to the lock-in amplifier, where shifts in the spectra are detected through phase changes with respect to the reference signal.

To improve detection limits, we introduce a modulation scheme for measuring resonance shifts using phase sensitive detection. The scheme is shown in **Figure 5.7** and revolves around modulating the excitation wavelength from the tunable diode laser while using phase sensitive lock-in detection to monitor shifts in the WGM resonance.

A triangle waveform is used to tune the frequency of the tunable diode laser as shown in **Figure 5.7a**. As the voltage increases during the up scan of the triangle wave, the laser output tunes to longer wavelengths. When the waveform transitions to the down scan, the decreasing voltage tunes the laser to shorter wavelengths and eventually returns it to its initial value before starting the next cycle. Excitation light from the laser is directed into a dove prism, creating the evanescent field required to couple light into the resonator. Increases in the evanescently scattered light from the resonator reflect resonances, which are detected with a PMT. As shown in **Figure 5.7b**, a peak reflecting a WGM resonance is observed on the up scan of the waveform and then again on the down scan as the laser wavelength is reset. This results in the mirror image detection of the same WGM resonance during one complete cycle of the triangle waveform.

Assuming a band eluting from the CE column increases the refractive index around the resonator, a red shift in the WGM resonance will be observed as shown in **Figure 5.7b**, this will shift the peak observed on the up scan to the right while the peak measured on the down scan will shift to the left with an equal magnitude. The second peak measured on the down scan, therefore, causes problems for using phase measurements to track spectral shifts. One way to eliminate the second peak is to use a sawtooth waveform to modulate the laser. The rapid reset of the laser wavelength on the falling edge of the sawtooth waveform prevents the PMT from registering the second resonant peak. This approach, however, is limited to slow modulation frequencies for lasers using piezoelectric tuning elements as high frequency Fourier components in the waveform lead to ringing. A more flexible approach enabling higher modulation rates is outlined in **Figure 5.7**.

To eliminate the second peak on the down scan, the output of the PMT is sent to a track-and-hold circuit. The track-and-hold passes the output of the PMT until a triggering event is received. Upon triggering, the track-and-hold circuit will output the last voltage level received and hold that output until reset. In **Figure 5.7c**, the track-and-hold passes the signal from the PMT on the rising slope to register

the WGM resonance. When the scan voltage reaches its maximum value, the track-and-hold circuit is triggered. This holds in the last voltage level received from the PMT and outputs this value during the down scan. Once the laser wavelength has been reset to its initial value, the track-and-hold is unlatched and the process is repeated as shown in **Figure 5.7c**.

The output of the track-and-hold circuit simplifies the signal to just one peak per complete cycle, thus enabling phase detection of the resonant shift. The track-and-hold output is then sent to the input of a dual channel lock-in amplifier referenced to the laser modulation frequency. The phase signal is monitored to detect shifts in the resonant peak with respect to the laser modulation waveform, thus enabling real-time tracking of RI changes as shown in **Figure 5.7d**.

5.3.4 Phase sensitive-WGM comparison to spectral WGM

Refractive index sensing with WGM resonators is most often used in specific sensing applications where binding of analytes to surface immobilized recognition molecules leads to significant changes in the local refractive index.[28,29,32] Using WGM detection to monitor bulk refractive index changes, as needed in separations, leads to less favorable detection metrics since the response is not enhanced by concentrating species at the sensor surface. These challenges have been discussed previously using other RI detection platforms and can be addressed by chemical or molecular functionalization to increase the affinity of ions at the sensor surface.[19,33] Here, the use of a phase sensitive detection greatly improves detection limit metrics without the need for sensor surface modification.

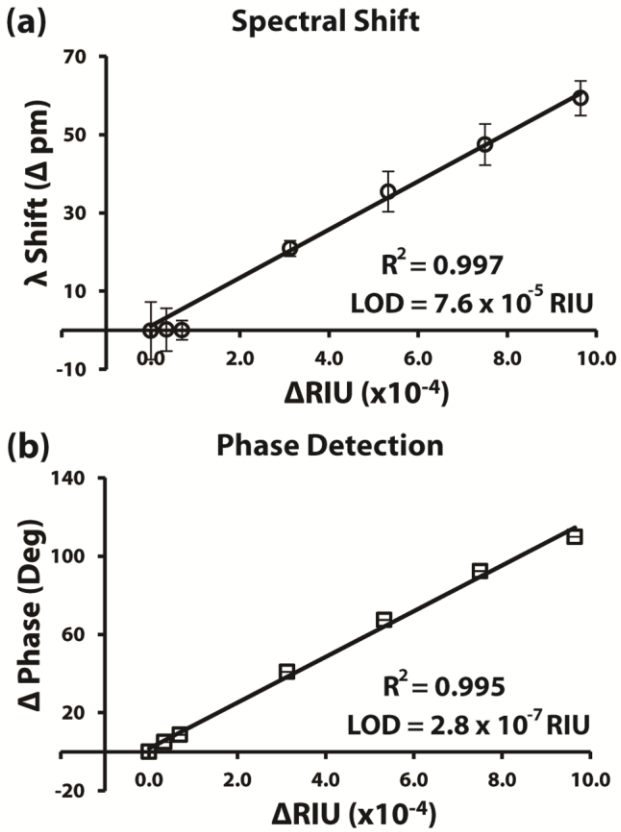

Figure 5.8. Calibration plots measured using (A) spectral collection and (B) the phase sensitive detection outlined in Fig. 4. To ensure a direct comparison, the same resonator was used for simultaneous measurements. In (A), spectral measurements lead to a LOD of 7.6 x 10^{-5} RIU and are unable to detect changes from the first few injections at low concentration. With phase sensitive detection in (B), these injections are clearly detected and the LOD improves significantly to 2.8 x 10^{-7} RIU (error bars within the points). Included error bars are smaller than the symbols shown and are calculated from the noise at each point following equilibration.

To directly compare typical WGM spectral shift measurements with phase sensitive WGM (PS-WGM) detection, spectral and phase data were collected simultaneously from the same resonator in a single assay. **Figure 5.8** shows refractive index calibration plots measured using conventional spectral measurements compared with the phase sensitive approach. NaCl solutions were used to increase the refractive index in stepwise fashion and both calibration curves were measured using the same resonator, which had a Q-factor of ~10^5. We note that Q-factors vary between resonators which can cause differences in sensitivities.[34,35] By using the same resonator to collect both spectral and phase data during the RI assay, a direct comparison between the two methods can be performed. The linear

response of the phase sensitive measurements track the response measured using spectral measurements, validating the phase sensitive approach.

For the phase sensitive approach, the laser wavelength was modulated at 215 Hz over its entire tuning range (632.920 nm to 633.120 nm). Using a time constant of 1 sec, the enhanced signal-to-noise obtained with the phase sensitive method leads to a limit of detection (LOD) of 2.8 x 10^{-7} RIU (27 µM NaCl), compared with an LOD of 7.6 x 10^{-5} RIU (7.5 mM NaCl) measured using spectral measurements with the same resonator. Phase sensitive detection, therefore, results in almost 300 fold improvement in LOD while streamlining both data collection and analysis time. Both approaches typically exhibit a dynamic range of 3 to 4 orders of magnitude which is limited by the laser tuning range (200 pm).

5.3.5 CE-PS-WGM Separation

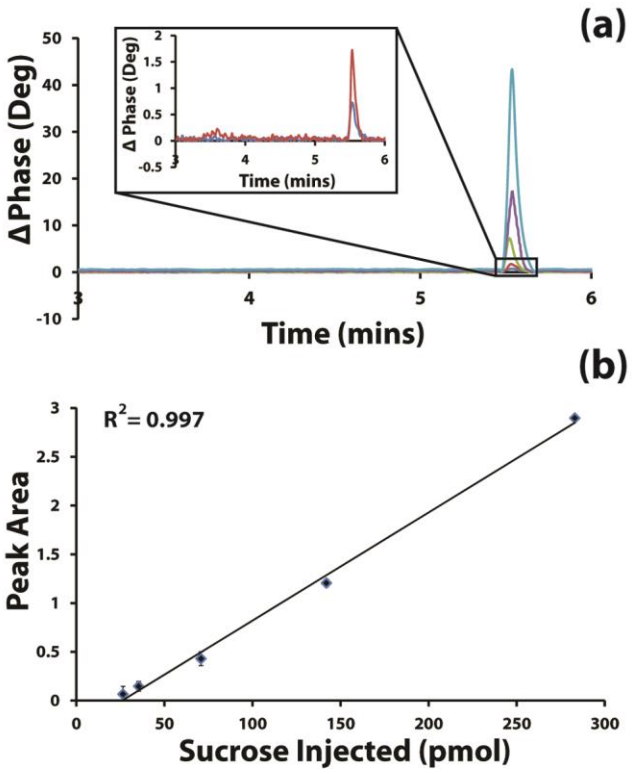

Figure 5.9. (A) Overlay of 5 separate runs following injection of sucrose plugs (0.09%, 0.12%, 0.25%, 0.5% and 1%) detected using PS-WGM. The sucrose injected ranged from 26.5 to 283 pmol in a volume of 9.7 nL (2.7 to 29 mM). The inset shows an expanded view for the two lowest concentrations, detected with a S/N ratio greater than 8. (B)

Peak area is plotted against sucrose injected, showing good linearity. Error bars represent standard deviation from 3 separate measurements.

Having validated the PS-WGM detection scheme, **Figure 5.9** shows initial studies to characterize its integration with CE. In **Figure 5.9a**, sucrose bands migrating through a 55 cm capillary using EOF are detected with end-capillary PS-WGM detection. **Figure 5.9a** overlays five different electropherograms collected as sucrose injections increased from 27 pmol to 283 pmol in an injected volume of 9.7 nL (2.8 mM to 30 mM). At a pH of 5, sucrose is neutral leading to a migration time of 5.6 minutes. The relative standard deviation (RSD) in migration times between all five injection are less than 3%, illustrating the reproducibility of the integrated system. This suggests that the placement of the resonator at the outlet of the capillary does not cause significant turbulent flow profiles. The expanded view in the inset shows the detection achieved, with a signal-to-noise of 8 measured at the lowest injection of 2.8 mM sucrose. The linear trend in peak area versus sucrose injected is plotted in **Figure 5.9b**.

The integration of PS-WGM detection with CE shares the advantage that other refractive index sensors have as universal detectors of analytes. Techniques such as WGM and SPR, however, can also be easily expanded for specific detection as demonstrated by Whelan et al. While surface plasmon resonance and optical resonators have been well adopted for HPLC, demonstrations of CE separation using resonators are limited. Here validation of the CE-PS-WGM approach which takes advantage of the small footprint of the resonator and universal detection properties is performed. Specifically three non-UV absorbing ions K^+, Na^+, and Li^+ are separated using this this novel PS-WGM approach.

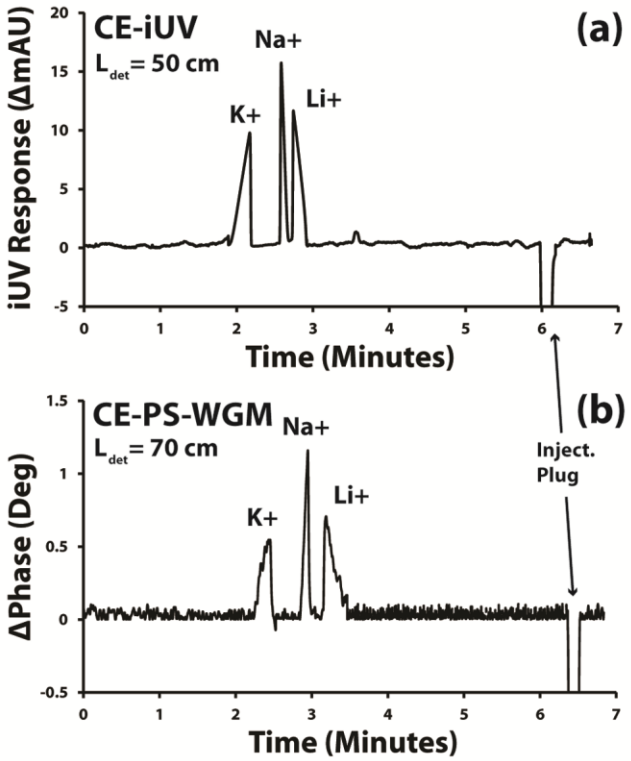

Figure 5.10. Separation of a three component mixture of potassium, sodium and lithium ions (22 pmol, 28 pmol and 39 pmol respectively) detected with (A) UV and (B) PS-WGM. The separation was optimized using a 70 cm capillary with the UV window located 50 cm from the inlet. The ions are separated in 5 mM imidazole at pH 5, using an injection volume of 4.9 nL and an applied potential of 24 kV. The electropherogram in (A) shows good separation with characteristic peak shapes reflecting the ion migration in the background electrolyte. End-capillary PS-WGM detection in (B), measured during the same separation, yields very similar results thus validating the approach. Characteristic peak shapes are similar and additional 20 cm of capillary travel to the detector does not significantly broaden the peaks and slightly improves resolution.

In **Figure 5.10a**, the separation of the three ions was optimized on a 70 cm length capillary (75 µm I.D., 363 µm O.D.) with the UV detector positioned 50 cm from the capillary inlet. The sample of ion mixture was pressure injected with a volume of 4.9 nL resulting in loadings of 22, 28 and 39 pmol (4.5 mM, 5.7 mM and 7.9 mM) of K^+, Na^+ and Li^+ ions respectively. For indirect UV detection, the pH 5 run buffer included 5 mM of UV absorbing imidazole. The high ionic strength of the imidazole raises concerns over Joule heating so the separation voltage was minimized to 24kV, below the measured nonlinear region of the Ohm's plot. Before each run, the capillary was thoroughly rinsed with at least

three capillary volumes each of 0.1 M NaOH, water and the 5 mM imidazole run buffer. This resulted in reproducible EOFs between each run and consistent peak shapes and migration times.

The UV electropherogram shown in **Figure 5.10a** reveals the separation of K^+, Na^+, and Li^+ ions and exhibits distinctive peak shapes that are consistent with previous studies.[9,36] The potassium ion elutes first and has a higher mobility than the background electrolyte (BGE). This leads to the sawtooth shaped peak that gradually rises on the leading edge and abruptly falls on the trailing edge. Lithium ion, on the other hand, elutes last and has a lower mobility than the BGE. This leads to an asymmetrical peak shape that mirrors that of potassium, now quickly rising on the leading edge while gradually decreasing on the trailing edge. Finally, the middle peak due to Na^+ is more symmetric reflecting a similar mobility with BGE.

Figure 5.10b shows the same ion separation run as that in **Figure 5.10a**, but with end-capillary detection using PS-WGM. For these measurements the laser wavelength was modulated at 215 Hz over the entire tuning range (632.920 to 633.120 nm) and a 300 ms lock-in time constant was utilized. Three baseline separated ion peaks are observed with the same distinctive peak shapes as that detected 20 cm upstream using UV absorbance. **Table 5.1** compares the plate number and RSD values for UV detection at a length to detector (L_D) of 50 cm and PS-WGM detection with an L_D of 70 cm. The additional 20 cm of travel for PS-WGM detection results in increased diffusion of the peaks, which is reflected in the lower plate numbers reported in **Table 5.1**. The extra capillary length for PS-WGM detection, however, results in slightly increased resolution of the ions with both arrangements showing RSD values of less than 3.7%.

Table 5.1. Theoretical plates are calculated from Fig. 7 and adjusted to length to detector. The extra 20 cm travel to reach the PS-WGM detector results in lower plate numbers due to diffusion of the ions. RSD values less than 3.7% were achieved for all ions (N = 3).

UV Detection (L_D = 50 cm)		
Analyte	**N (plates/m)**	**RSD (N = 3)**
K^+	1970	3.3%
Na^+	15534	1.8%
Li^+	5834	2.7%

PS-WGM (L_D = 70 cm)		
Analyte	**N (plates/m)**	**RSD (N = 3)**
K^+	1894	2.3%
Na^+	5284	2.2%
Li^+	3186	3.7%

These results show that PS-WGM integration with CE enables real-time detection of small refractive index changes (10^{-7} RIU) without any modification to the capillary or microresonator. For the future, WGM microresonators are easily functionalized and often used in biosensing applications. Using the same approach outlined here, integrating specific sensing with CE using modified WGM resonators is conceptually straightforward. For applications such as serum protein CE, where the complicated nature of the mixture leads to proteins separated broadly by class, integrating specific sensing can target specific species within a band.

5.4 Conclusions and outlook

We demonstrate integration of end-capillary WGM refractive index sensing for peak detection in CE separations. Unlike most refractive index detectors for CE, no physical modification of the capillary is required, the approach is compatible with a wide range of capillary types, and the method is modular and easily extended for specific sensing applications. While we demonstrate the approach using 53 µm diameter resonators, we can routinely measure resonances in barium titanate microspheres less than 20

μm in diameter, enabling integration with smaller bore capillaries. As shown by others, resonator size can help optimize LODs by reducing tunneling and absorption losses.[37] To increase performance metrics for bulk refractive index sensing, we introduce a novel wavelength modulation approach using phase sensitive detection to characterize spectral shifts in the WGM detector. We show that this method improves detection limits two orders of magnitude over simultaneous measurements done using traditional spectral collection. This approach also streamlines the data collection and analysis by providing real-time measures of WGM peak shifts. Phase sensitive detection of WGM shifts are used to characterize the CE separation of potassium, sodium, and lithium ions, validating the approach. The small footprint of WGM resonators and the ease with which specific biosensing can be implemented through surface functionalization should add powerful new dimensions in separations using small capillaries or lab-on-a-chip platforms.

5.5 Reference

1. Ewing, A. G., et al. Capillary electrophoresis. *Analytical Chemistry* **1989**, *61*, 292A-303A.
2. Kuhr, W. G., et al. Capillary electrophoresis. *Analytical Chemistry* **1992**, *64*, 389R-407R.
3. Moser, A. C., et al. Clinical Applications of Capillary Electrophoresis-Based Immunoassays. *Electrophoresis* **2014**, *35*, 937-955.
4. Petersen, J. R., et al. Capillary electrophoresis and its application in the clinical laboratory. *Clin. Chim. Acta* **2003**, *330*, 1-30.
5. Zhu, Z., et al. Protein Separation by Capillary Gel Electrophoresis: A Review. *Anal. Chim. Acta* **2012**, *709*, 21-31.
6. Riddick, L., et al. In *Capillary Electrophoresis*, Schmitt-Kopplin, P., Ed.; Humana Press, 2008, pp 119-134.
7. Fonslow, B. R., et al. Capillary Electrophoresis Applied to Proteomic Analysis. *J. Sep. Sci.* **2009**, *32*, 1175-1188.
8. Kraly, J. Bioanalytical Applications of Capillary Electrophoresis. *Anal. Chem.* **2006**, *78*, 4097-4110.
9. Heiger, D., et al. Determination of small ions by capillary zone electrophoresis with indirect photometric detection. *HP Application Note* **1994**.
10. O'Brien, R. W., et al. Electrophoretic mobility of a spherical colloidal particle. *Journal of the Chemical Society, Faraday Transactions 2: Molecular and Chemical Physics* **1978**, *74*, 1607-1626.
11. Walbroehl, Y., et al. On-column UV absorption detector for open tubular capillary zone electrophoresis. *J. Chromatogr. A* **1984**, *315*, 135-143.
12. Chabinyc, M. L., et al. An Integrated Fluorescence Detection System in Poly(dimethylsiloxane) for Microfluidic Applications. *Anal. Chem.* **2001**, *73*, 4491-4498.

13. Baldwin, R. P. Recent advances in electrochemical detection in capillary electrophoresis. *Electrophoresis* **2000**, *21*, 4017-4028.
14. Bruno, A. E., et al. On-column laser-based refractive index detector for capillary electrophoresis. *Anal. Chem.* **1991**, *63*, 2689-2697.
15. Swinney, K., et al. Detection in capillary electrophoresis. *Electrophoresis* **2000**, *21*, 1239-1250.
16. Swinney, K., et al. Ultrasmall volume refractive index detection using microinterferometry. *Rev. Sci. Instrum.* **2000**, *71*, 2684-2692.
17. Swinney, K., et al. Universal detection in capillary electrophoresis with a micro-interferometric backscatter detector. *Analyst* **1999**, *124*, 221-225.
18. Burggraf, N., et al. Holographic refractive index detector for application in microchip-based separation systems. *Analyst* **1998**, *123*, 1443-1447.
19. Whelan, R. J., et al. Surface Plasmon Resonance Detection for Capillary Electrophoresis Separations. *Anal. Chem.* **2003**, *75*, 1542-1547.
20. Zhu, H., et al. Integrated Refractive Index Optical Ring Resonator Detector for Capillary Electrophoresis. *Anal. Chem.* **2007**, *79*, 930-937.
21. Wade, J. H., et al. Refractive Index-Based Detection of Gradient Elution Liquid Chromatography using Chip-Integrated Microring Resonator Arrays. *Anal. Chem.* **2014**, *86*, 913-919.
22. Kussrow, A., et al. Measurement of Monovalent and Polyvalent Carbohydrate−Lectin Binding by Back-Scattering Interferometry. *Anal. Chem.* **2009**, *81*, 4889-4897.
23. Bornhop, D. J., et al. Simultaneous laser-based refractive index and absorbance determinations within micrometer diameter capillary tubes. *Anal. Chem.* **1987**, *59*, 1632-1636.
24. Vollmer, F., et al. Label-free detection with high-Q microcavities: a review of biosensing mechanisms for integrated devices. *Nanophotonics* **2012**, *1*, 267.
25. Gorodetsky, M. L., et al. Optical microsphere resonators: optimal coupling to high-Q whispering-gallery modes. *J. Opt. Soc. Am. B* **1999**, *16*, 147-154.
26. Knight, J. C., et al. Phase-matched excitation of whispering-gallery-mode resonances by a fiber taper. *Opt. Lett.* **1997**, *22*, 1129-1131.
27. Kim, D. C., et al. Integration of microsphere resonators with bioassay fluidics for whispering gallery mode imaging. *Analyst* **2013**, *138*, 3189-3195.
28. Huckabay, H. A., et al. Whispering gallery mode imaging for the multiplexed detection of biomarkers. *Sens. Actuators, B* **2011**, *160*, 1262-1267.
29. Huckabay, H. A., et al. Label-free detection of ovarian cancer biomarkers using whispering gallery mode imaging. *Biosens. Bioelectron.* **2013**, *45*, 223-229.
30. Washburn, A. L., et al. Label-free quantitation of a cancer biomarker in complex media using silicon photonic microring resonators. *Anal. Chem.* **2009**, *81*, 9499-9506.
31. Vollmer, F., et al. Multiplexed DNA quantification by spectroscopic shift of two microsphere cavities. *Biophys. J.* **2003**, *85*, 1974-1979.
32. Hanumegowda, N. M., et al. Label-free protease sensors based on optical microsphere resonators. *Sensor Letters* **2005**, *3*, 315-319.
33. Hanumegowda, N. M., et al. Aqueous mercuric ion detection with microsphere optical ring resonator sensors. *Sensors and Actuators B: Chemical* **2006**, *120*, 207-212.
34. Foreman, M. R., et al. Optimizing detection limits in whispering gallery mode biosensing. *Opt. Express* **2014**, *22*, 5491-5511.
35. Reynolds, T., et al. Optimization of whispering gallery resonator design for biosensing applications. *Opt. Express* **2015**, *23*, 17067-17076.
36. Gross, L., et al. Indirect fluorometric detection of cations in capillary zone electrophoresis. *Anal. Chem.* **1990**, *62*, 427-431.

37. Arnold, S., et al. MicroParticle photophysics illuminates viral bio-sensing. *Faraday Discuss.* **2008**, *137*, 65-83.

5.6 Appendices

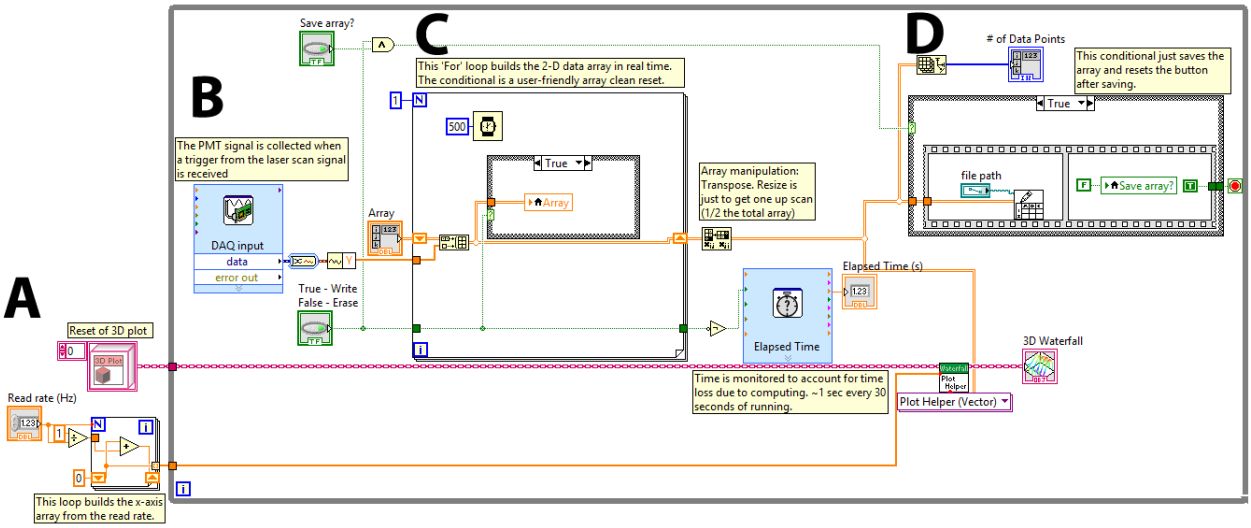

Appendix 1 – (A) These parameters outside the 'while' loop reset the waterfall plot before each run and initializes the array used for real-time data storage. (B) This portion collects the data when triggered by the edge of the triangle wave used for modulating the tunable laser. (C) This 'For' loop builds the array where the PMT signal for one tuning cycle of the laser is individually addressed over time. (D) This portion allows the data array built in real-time to be saved as a .txt or .xls file when a Boolean is pressed by the user.

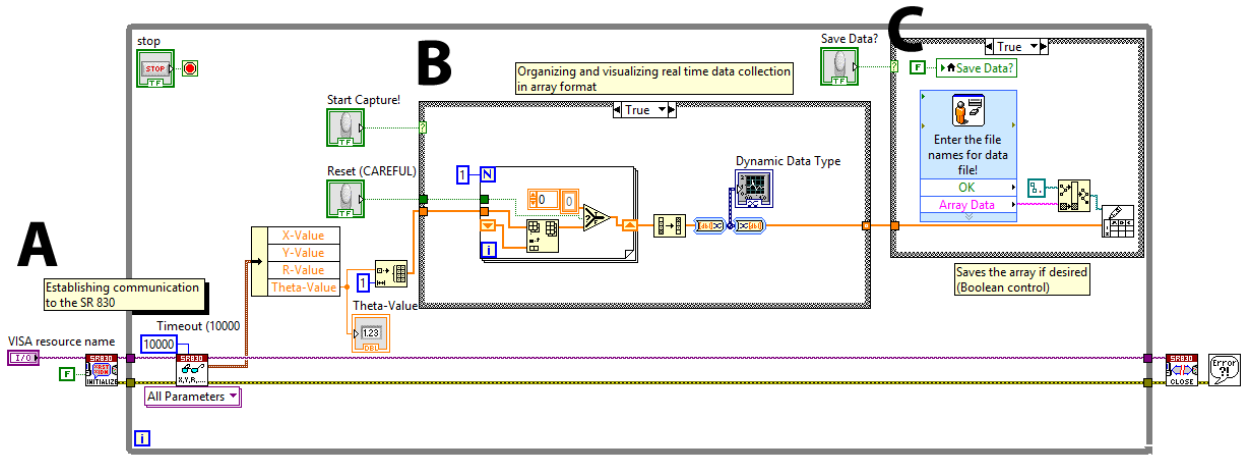

Appendix 2 – (A) This establishes communication to the SR830 to the LabView interface such that data can be read for the SR 830 directly. (B) The theta values are read in real time and store them in an array format where each data point is sequentially addressed. Dynamic data is graphed giving the user real-time graphical either .txt or .xls form.

Chapter 6

Specific Detection of Proteins in Capillary Electrophoresis using Whispering Gallery Mode Resonators

6.1 Introduction

In chapter 5, three cations (Na^+, Li^+, K^+) were separated and detected through bulk refractive index changes using phase sensitive-WGM (PS-WGM) and UV detection simultaneously illustrating the compatibility of the WGM with CE separations. Here we extend the utility of the CE-WGM interface as a CE-immunoassay technique by placing a WGM resonator with recognition proteins attached to its surface. CE-based immunoassay combines the separation power of CE with the specificity between antigen and antibody to achieve 2-dimensional assays.[1-4] Many capillary electrophoresis based immunoassay approaches require immobilizing the antibody or antigen onto the inner wall of the capillary along the separation path.[5-7] Attachment of biocapture materials on the walls of capillary is an effective approach, however, the capillary must be replaced entirely after several uses. The required use of low pH elution buffers, to disrupt the binding interaction, can also negatively affect the antibody function. We introduce CE-WGM immunoassay as a modular (no capillary modification), post-separation (no low pH elution buffer) immunoassay as a unique capillary electrophoresis based immunoassay approach.

6.1.1 Capillary electrophoresis based immunoassays (CEIA)

The current gold standard for the quantification of biomarkers is enzyme-linked immunosorbent assay (ELISA) which has played a central role in diagnostic and clinical research for several decades. ELISA can be used for the detection of prostate specific antigen (PSA) as a biomarker for early stage prostate cancer which has effectively reduced mortality rates. However, there are many applications in which ELISA, as a mono-dimensional immunoassay, suffer from false-positive results. False positives have been described in a number of ELISA tests for diseases such as HIV[8], multiple myeloma[9] and ovarian cancer among many others. False-positive results in mono-dimensional immunoassays are largely a result of the polyreactive nature of antibodies.[10-12] This results in non-specific binding of antigen which is especially prominent in complex sample matrices such as serum. Emerging multi-dimensional techniques which couple immunoassays with a separation system are gaining acceptance in diagnostic applications.

One such 2-D method is capillary electrophoresis based immunoassays (CEIA), often called immunoaffinity capillary electrophoresis (IACE).[2,4,13,14] These techniques can be performed as homogeneous immunoassays, where antibody and antigens are present in free-solution, or heterogeneous immunoassays, where either the analyte or the antibody is immobilized onto a solid support.[3,4,13] Here we will focus on the review of heterogeneous based CEIA, as it is more closely relevant to WGM immunoassays.

Heterogeneous CE immunoassays employ an immobilized antibody or antigen as a stationary phase for online solid phase extraction.[13] The technique relies on the strong affinity of antigen-antibody interaction as a means of removing analytes of interest from a sample matrix. These 2-dimensional techniques can significantly diminish false-positive information because non-specifically bound targets that are structurally unrelated to the analyte of interest can be differentiated by differences in migration times.[13] The outline of the technique is illustrated in **Figure 6.1**.

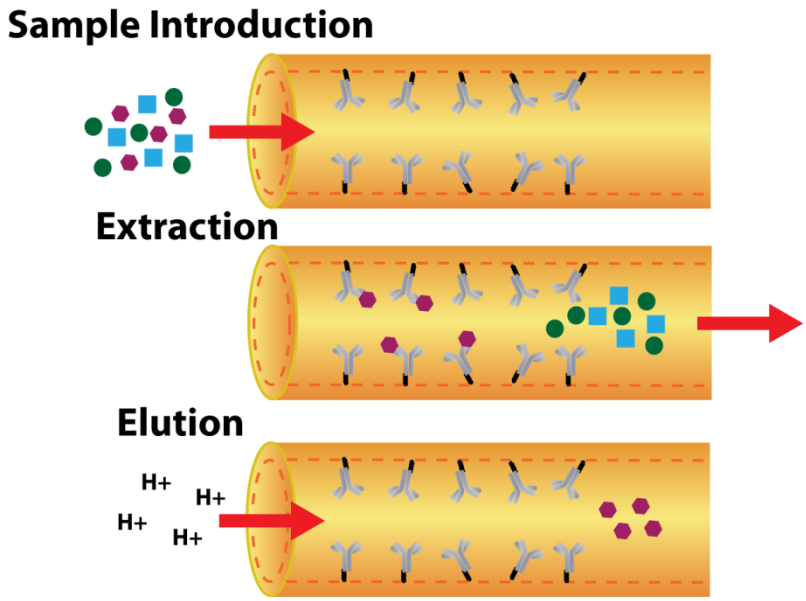

Figure 6.1. Procedural illustration of heterogeneous capillary electrophoresis immunoassays. The sample is introduced to the antibody functionalized capillary walls for specific capture of an analyte of interest. Then a low pH elution buffer is used to release the captured analyte for subsequent separation and detection.

Antibodies are covalently attached to the walls at a region near the inlet of the capillary. Then the sample is then injected and driven past this region by laminar flow, allowing a particular antigen to bind to the immobilized antibodies excluding all other material. Once the antibody-antigen complex is formed, a small plug of weakly acidic elution buffer is injected to release the captured antigen for subsequent detection.

The most straight-forward method for protein immobilization is to utilize the surface chemistry of the walls of the capillary to covalently attach the affinity capture material. This results in an open tubular SPE extraction along the capillary flow path that can specifically bind analytes of interest. To improve the surface area to volume ratio and enhance the number of available binding molecules, small beads of either polymeric or glass material can be packed into a glass fiber frits as a junction between two separate capillary tubes as shown in **Figure 6.2a**.[15,16] Another design utilized functionalized magnetic beads introduced into the capillary and localized via external magnets at a particular region along the capillary as shown in **Figure 6.2b.**[17,18]

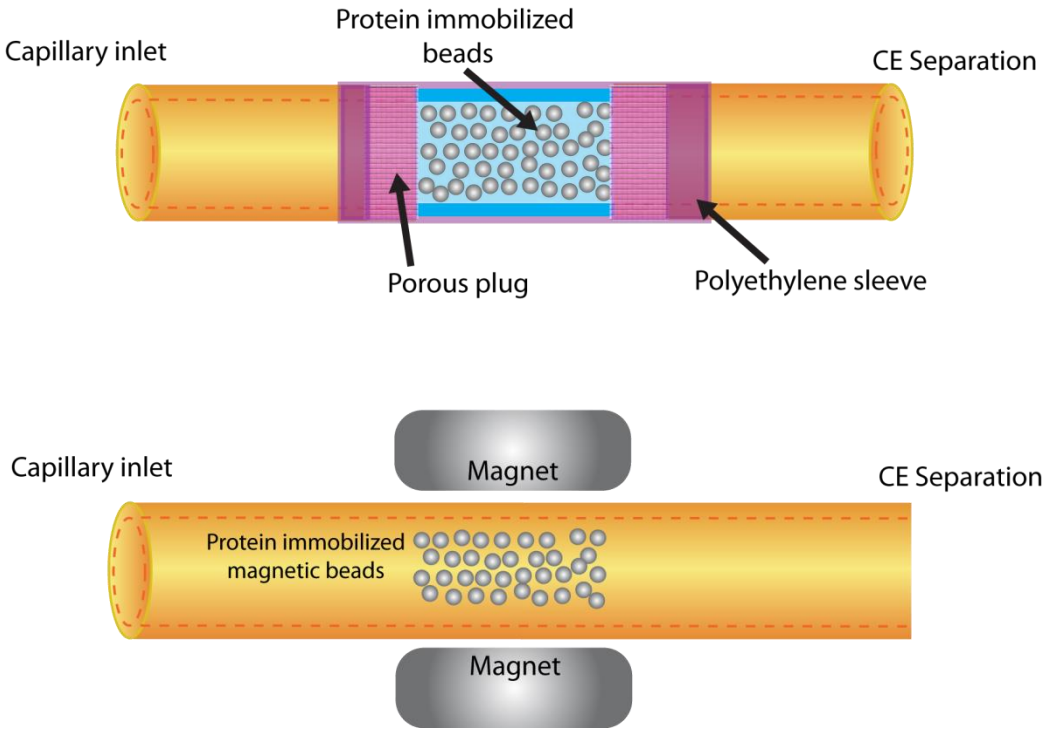

Figure 6.2. Illustrations of a two approaches for on-capillary protein immobilization. The top schematic illustrates the use of a polyethylene junction between two capillaries combined with porous plugs to place protein immobilized beads along the capillary. The bottom schematic utilizes protein immobilized magnetic beads with externally placed magnets to localize the beads inside the capillary.

A variety of detection methods can be used for heterogeneous CE immunoassays. Fluorescence detection offer low detection limits (low pM) with the use of numerous labeling strategies. This requires a fluorescently labeled secondary to bind to the antibody-antigen complex much like ELISA. Then the elution buffer disrupts the binding interactions leading to the release of fluorescently labeled secondary for subsequent detection. Another approach uses chemiluminescent properties of luminol to provide rapid and low background signals. Luminol (5-amino-2, 3-dihydro-1,4-phthalzinedione) is a common chemiluminescent tag that forms 3-aminophthalate through a reaction with hydrogen peroxide under basic conditions. Gold nanoparticles have also been used to catalyze luminol chemiluminescence. One drawback of chemiluminescence is the need for a post-column reaction tube to produce the chemiluminescent signal. The use of additional post-capillary reagents requires tedious optimization of

the reaction conditions and suffers from higher assay costs. Label-free techniques, such as SPR and WGM can, therefore, make positive contributions for these applications.

Despite an impressive list of applications using CEIA in pharmaceutical analysis,[19-21] biomarker detection[22-24] and immunology,[25,26] there are some limitations that can be addressed by a re-design of the assay steps. Typically, the capillary is filled entirely with the sample as this technique relies on the incubation for the extraction of the analyte of interest. This leads to waste of precious sample volume. Even though the volumes in capillary electrophoresis are relatively small, for several applications such as tear sample analysis and pre-natal diagnostics it may be of considerable interest to preserve as much sample as possible. Another drawback of CE immunoassays is that the extraction of different analytes then naturally requires newly validated separation conditions. A high information sample, such as serum, contains thousands of biomarkers for a plethora of diseases. Each disease diagnostic requires an entirely new separation step, which practically limits the use of the technique by trained lab technicians. It would be beneficial to develop a more modular immunoassay platform combined with CE that requires little optimization of the CE separation. Additionally, most current detection methods used in CEIA require the use of fluorescent labels with secondary antibody or chemiluminescent reagents.[27] Using a label-free WGM resonator as an immunoassay at the outlet of the capillary holds considerable promise for the development of a modular and label-free immunoassay detector that can be integrated without modifications to the separation conditions for a 2-D separations technique.

6.1.2 Opportunities for CE-WGM immunoassays

Previous researchers have demonstrated the sensitive, label-free detection of various putative biomarkers for ovarian cancer.[28] Demonstration of the detection of cancer antigen-125 spiked in a serum sample was an impressive feat considering the complexity of the serum sample and chances of non-specific binding.[28] In an initial investigation, CA-125 detection in serum, compared to its detection

in a less complex PBS buffer, exhibited an order of magnitude higher detection limits (1.8 U/mL in serum compared to 0.11 U/mL in buffer) and lower sensitivities (1.8 pm/U/mL in serum compared to 18 pm/U/mL in buffer).[28,29] These initial metrics suggest that immunoassays in complex samples can be more challenging due to effects such as non-specific binding.

As non-specific binding is a significant challenge for all label-free biosensors, we propose the use of 2-D immunoassays where we first separate proteins then specifically detect a protein of interest using WGM resonators. CE based serum protein electrophoresis stratifies proteins into zones where the most abundant protein, albumin, migrates last. By coupling this separation with WGM immunoassays where diagnostically relevant proteins for most cancers migrate prior to albumin, we effectively simplify the serum sample matrix in an effort to improve the immunoassay platform.

Additionally, placement of the immunoaffinity step after the separation step results in a completely modular separation and immunoassay test where the separation is unaffected by the immunoassay. This can be a tremendous advantage because already validated separation methods can be coupled with CE-WGM immunoassays to achieve a 2-D immuno-separation system. We also take advantage of the intrinsic benefits of the WGM detection scheme as a label-free, highly sensitive detector described in Chapter 2. Here, we demonstrate a 2-D immune-separation of two proteins as a proof-of-concept for a novel CE-immunoassay device.

6.2. Materials and Methods

6.2.1 Instrumentation

The instrumentation set-up described in section 5.2.1 was utilized in this chapter. The output from a tunable diode laser (Vortex II TLB-7004, <500 kHz linewidth, 160 GHz mode-hop free tuning, New Focus, Santa Clara, CA) centered at 633.020 nm is focused into a Dove prism (Edmund Optics, Barrington,

NJ). Light entering the Dove prism is directed towards a glass substrate at an angle leading to total internal reflection. The associated evanescent field excites resonances in 53 µm barium titanate resonators (53 µm ± 3% diameter, MO-SCI, Rolla, MO) on the glass substrate surface as shown previously in **Figure 5.3**. A microwell on the substrate surface confines the resonator in ≈500 µL of run buffer. Evanescently scattered light from the resonator is collected from below using a 10X objective (Olympus UMPlanFL NA=0.3, Center Valley, PA) and detected on a photomultiplier tube.

6.2.2 Capillary Electrophoresis-WGM and UV detection

WGM detection was integrated with capillary electrophoresis (CE) using a custom-built apparatus. The inlet of the 70 cm (unless specified) CE capillary (75 µm I.D., 363 µm O.D.; PolyMicro Technologies, Phoenix, AZ) was equipped with a T-valve connected to a custom pressure injection system with 0.01 second accuracy. The outlet of the capillary was held in a *xyz* micromanipulator (Model A LHFF, Line Tool Co., Allentown, PA) to precisely position it above a WGM resonator. The capillary outlet partially surrounds the resonator on the glass surface and helps hold it in place. Further procedures to immobilize the resonator on the surface were not required. Electroosmotic flow was driven with a high voltage power supply (Spellman CZE1000R, Valhalla, NY) connected through molybdenum wires running parallel to both the inlet and outlet of the capillary. For all separations, UV detection (SpectraSYSTEM UV1000, ThermoScientific, San Jose, CA) was also implemented using a window created 50 cm from the capillary inlet by removing the capillary coating.

6.2.3 Phase detection for WGM resonances

As previously described in chapter 5, to track WGM resonances using phase sensitive detection, the laser wavelength is modulated with the triangle wave over its entire tuning range (632.920 nm to 633.120 nm) at 215 Hz. The output of the PMT is sent to a track-and-hold circuit (Mattson Mini Modular

Model: SH1-B), which is triggered to hold the last valued received by the PMT before the down scan of the triangle wave. This simplifies the measured spectrum to one peak per complete cycle. The output of the track-and-hold circuit is sent to a dual-channel lock-in amplifier (SR830, Stanford Research Systems) referenced to the laser modulation signal. The phase signal is detected which reflects spectral shifts of the WGM resonator with respect to the laser modulation. Here, all protein binding and bulk refractive index measurements were done using phase sensitive detection.

6.2.4 Microsphere functionalization

To prepare microspheres for binding assays, proteins were covalently attached by the following procedure. Approximately 0.1 g of 53 μm barium titanate spheres was placed in a 4 mL glass vial. The spheres were rinsed with 10% Contrad (Decon Contrad 70, Fisher Scientific) solution then incubated and sonicated in 30% H_2O_2 (ACS certified, Fisherbrand) for 15 mins. The resonators were rinsed sequentially in water, ethanol (ACS certified, Fisherbrand) and toluene (extra dry, Acros Organics) then reacted in 10% (3-aminopropyl)triethoxysilane (APTES, AcroSeal©, Acros Organics) and rotated for 2 hours. Following silanization, spheres were rinsed in toluene then acetone (ACS certified, Fisherbrand). All solvent were then removed from the vial and the spheres were placed in a 60°C oven for 2 hrs. During the oven incubation, the vial was gently agitated until spheres could freely move to ensure no solvent is trapped between the spheres. The spheres were removed from the oven then placed in a vial containing molecular sieves overnight to remove any remaining moisture. The spheres were then reconstituted in ethanol and sonicated for 10 mins. After this step, spheres were placed into a new glass vial, then rinsed in water and stored in phosphate buffer saline (PBS, MP Biomedicals). The new glass vial walls should have little to no silanized surfaces for the following step. A 10% solution of glutaldehyde (25% in water, Fisherbrand) was prepared in the sphere vial and rotated for 30 mins. After the reaction, the spheres were rinsed with PBS then transferred to a new glass vial and stored in PBS. The sphere

surfaces now contain free aldehyde groups that can react with primary amines. Aldehyde functionalized spheres were then reacted with streptavidin for at least 6 hrs at 4°C. Finally, the spheres were rinsed then stored in PBS at 4°C for future use. For the detection of IL-6, biotinylated anti-IL-6 (IL-6 ELISA kit, BD OptEIA, BD Biosciences) was incubated for at least 6 hrs to complex with the covalently bound streptavidin.

6.2.5 Bioassay procedures for BSA-biotin and IL-6

For BSA-biotin and IL-6 assays, microspheres functionalized with streptavidin (for the detection of BSA-biotin) or biotinylated anti-IL6 (for the detection of IL-6) were placed on a glass slide and placed in a flow cell with a reservoir volume of 500 μL. To validate the functionalization of the microspheres, an assay for each of the two proteins was separately performed. Injections of a 0.1 μg/mL solution of BSA-biotin (lyophilized, Sigma-Aldrich) were made resulting in a concentration range of 0.15 to 0.81 nM BSA-biotin. The molecular weight of BSA-biotin (69.4 kDa) was estimated based on manufacturer data showing ~12 moles biotin per 1 BSA molecule. For the IL-6 assay, injections from a stock solution (2175 pg/mL IL-6) were made to generate a concentration range of 1.8 to 23.8 pM. Each injection was followed by a 10 min incubation period before the phase measurement was recorded.

6.2.6 CE-WGM immunoassay of BSA-Biotin and IL-6

The separation of bovine serum albumin-biotin (BSA-biotin) and interleukin-6 (IL-6) was optimized on a 70 cm length capillary (75 μm I.D., 363 μm O.D.) with the UV detector positioned 50 cm from the capillary inlet. The sample containing 0.2 mg/mL BSA-biotin and 217 pg/mL IL-6 was pressure injected with a volume of 4.9 nL. The separation of these two proteins was optimized in 10 mM sodium phosphate monobasic and 10 mM sodium phosphate dibasic at pH 7.4. A potential of 18 kV was used in this run buffer resulting in a separation current of roughly 47 μA. UV detection at 50 cm from the inlet

and PS-WGM detection at the outlet of the capillary (L_d = 70 cm) were simultaneously collected. The separation was performed using an unlabeled microsphere as a control and a streptavidin-labeled microsphere for specific detection of BSA-biotin binding both using the same separation conditions.

6.2.7 Serum protein electrophoresis of Clinical Samples

All samples used in our experiments were de-identified and collected for other purposes. A total of 10 serum samples, 5 from multiple myeloma patient and 5 serum sample from a healthy patient, was obtained from the University of Kansas Cancer Center Biospecimen Repository Core Facility. The MM patient sample was collected in 2012, post-treatment (Barcode = 003849). The control sample was collected in 1995 (Barcode = 000030). Additional information of these samples and other available samples can be found in the appendix. Serum protein electrophoresis of these samples was optimized on a 70 cm length capillary (75 µm I.D., 363 µm O.D.) with the UV detector positioned 50 cm from the capillary inlet. The sample was diluted at 1:40 serum to water ratio. A 4.9 nL sample injection was separated at 18 kV in pH 10, 7.5 mM sodium tetraborate or 30 mM borate (Sigma Aldrich).

6.3 Results and discussion

In previous studies, we have validated the use of phase sensitive WGM detection in the capillary electrophoresis separation of three cations, measuring the bulk refractive changes as these sample plugs are driven past the resonator. These studies revealed that the placement of a WGM detector directly at the outlet of the capillary minimally affects the separation profile. CE-WGM is capable of detecting the plug profile as a general bulk refractive index detector, however, the main motivation for interfacing CE with WGM resonators was to extend the utility of serum protein electrophoresis by performing an immunoassay after the initial serum separation. To move towards this 2-D separation and specific

detection system, we first validate the attachment of biocapture molecules to the sensor surface by measuring the specific binding of two proteins. We also present here several considerations critical for the attachment of recognition proteins to the surface of WGM resonators for label-free sensing. Finally, we utilize these functionalized microspheres as a biosensor integrated with capillary electrophoresis for the development of CE-WGM immunoassays.

6.3.1 Protein immobilization

Equation 2.4 introduced previously, illustrates that WGM resonator response ($\Delta\lambda/\lambda$) is directly proportional to the surface coverage of recognition element (σ_p).[30] It is therefore of great interest to maximize the number of recognition elements on the surface that is capable of binding analytes of interest. Heterogeneous immunoaffinity based assays employ immobilized antibodies as a stationary phase to capture antigens of interest from the sample matrix. The simplest method for placing recognition elements on a surface is done via passive binding or physical adsorption. This technique utilizes various interactions, such as electrostatic forces and van der Waals, between the surface and the biomolecular species.[31] Label-free sensors often employ surfactant additives to minimize non-specific binding by disruption ionic and hydrophobic biomolecule-surface bonds.[32] Direct adsorption via relatively weak interactions, can therefore, be easily be disrupted by the addition of these beneficial surfactants, resulting in losses of biosensor sensitivity.

In addition, physical adsorption results in random antibody orientations as shown in **Figure 6.3.**

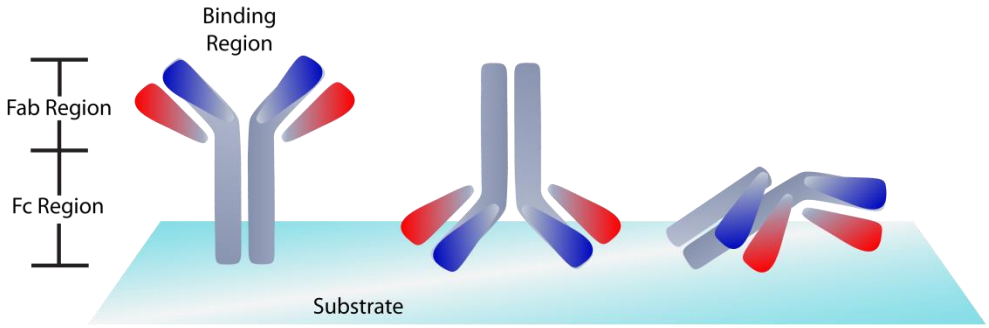

Figure 6.3. Illustration of antibody orientations on a substrate. (left) Antibody is oriented favorably where its binding region faces towards the solution. (middle, right) Antibody binding regions are less accessible for analytes in solution.

It is a clearly advantageous to direct the binding region of the antibody towards the solution rather than the substrate. Immobilization strategies using Protein A/G and streptavidin/biotin to control antibody orientation are illustrated in **Figure 6.4.**

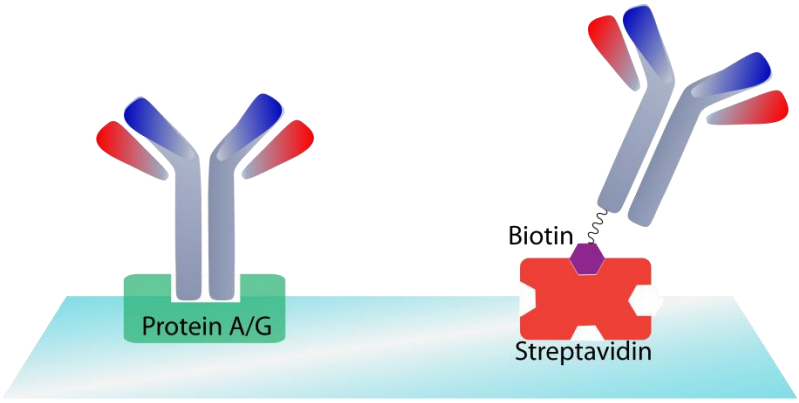

Figure 6.4. Approaches to improve antibody orientations. Protein A/G specific targets the binding of the Fc region of antibodies. Streptavidin is a tetramer and can bind biotinylated antibody for improved antibody orientation.

Bacterial cell wall proteins A and G selectively bind many antibodies at the Fc region with K_d in the range of 10^{-7} to 10^{-9} M.[33] Prolonged use of these sensors can release antibodies from the protein A/G surface leading to losses in sensor performance. Therefore, for a less reversible and more stable attachment, the streptavidin and biotin complex is often utilized as a method to attach antibodies to a surface.

Streptavidin is a bacterial form of avidin that exhibits strong binding with biotin and minimal nonspecific interaction with proteins. The streptavidin-biotin bond is nearly irreversible ($K_d = 10^{-15}$ M) which is stable yet amenable to release of bound material via pH changes.[34] Covalent attachment of streptavidin to a solid support such as glass can be done by reacting silanol groups on the glass surface with primary amine groups on proteins via APTES and glutaraldehyde cross-linking chemistry.[35] Streptavidin is a tetramer containing four binding sites for biotin and therefore the attachment via free-amines should not greatly impact the accessibility of the binding pocket. As illustrated in **Figure 6.4,** biotinylated antibodies, which are commercially sold, are bound to surface immobilized streptavidin with the binding regions of the antibody available to the solution. We use this approach in the following experiments with additional considerations in the development of a WGM biosensor.

6.3.2 Considerations for barium titanate microspheres for the attachment of recognition proteins

When starting the protein functionalization process, it is important to consider the abundance of surface functional groups to maximize protein surface coverage for sensing. Barium titanate (BT) microspheres have silanol groups that react with the APTES solution to initiate the functionalization process. However, the doping of bigger barium atoms, in chemical compositions of roughly 40% (reported by the MoSci), may reduce the number of surface silanol groups available for protein attachment. There is also evidence in previous studies that barium ions may be concentrated at the surface of a material further perpetuating the notion that there may be reduced –OH groups available for functionalization chemistry.[36,37] Therefore, it is advantageous to ensure that all the –OH groups on the surface of the microspheres are readily available to initially react with APTES.

Modifications of the method described by Huckabay et al.[28] have been made in an effort to improve the number of proteins attached to the surface. In addition to the described incubation of microspheres in hydrogen peroxide under sonication to enhance the activation of –OH groups, we

added a 45 second plasma treating step using a plasma reactor (PDC-32G, Harrick). Plasma treatment is a cleaning process that improves the homogeneity of the surface chemistry via the reaction of plasma radicals on the glass surface to remove water layers and other contaminants, such as absorbed gases and polymer fragments.[38] Additionally, the radicals transfer additional energy to the surface, therefore, increasing the activation energy to form desirable interfacial binding between silanol and APTES.

Label-free detection enables the monitoring of this functionalization process, by measuring resonance shifts of WGM resonators after the attachment of the recognition element and the binding of the analyte of interest. Here, we discuss the results of the experiment using streptavidin/biotinylated-anti-IL6 as a model system to assess functionalization. First we measure the covalently binding of anti-IL-6 to the glutaraldehyde linker surface using WGM resonators. After confirmation of antibody attachment through WGM resonance shifts, we measure subsequent binding of IL-6 to characterize sensitivity and statistics in a 16 microsphere WGM immunoassay.

6.3.3 Anti-IL-6 covalent bonding to glutaraldehyde surface

A hydrolysis reaction forms a covalent bond between the aldehyde functional groups on the resonator to the primary amines on the antibody. After the microspheres were incubated in the glutaraldehyde solution, we washed the spheres thoroughly in PBS buffer to ensure no unbound glutaraldehyde remained in solution. These microspheres were placed in the flow cell containing 500 μL of the anti-IL-6 solution from BD Biosciences. The resonant wavelengths of a total of 16 microspheres in the field of view were tracked over time, as shown in **Figure 6.5,** to a total of 20 hours.

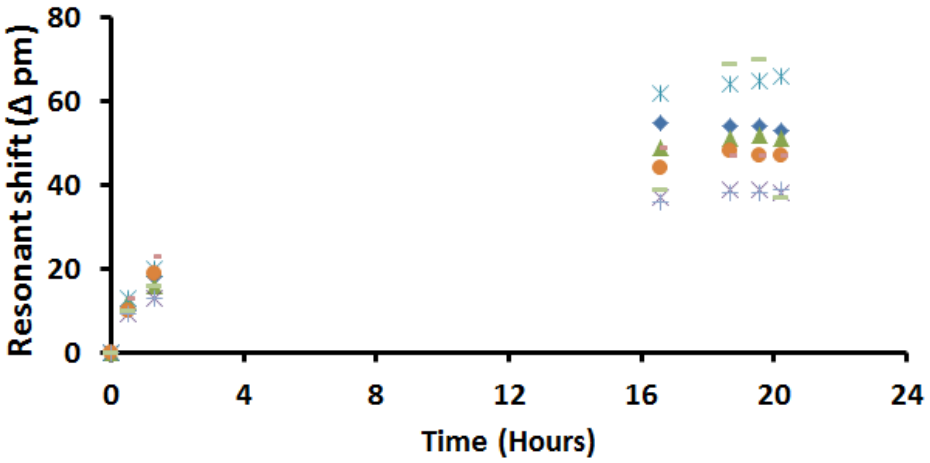

Figure 6.5. Free amine groups on anti-IL-6 binding covalently attaches to glutaldehyde functionalized microspheres. The attachment was monitored by tracking the resonant shift over time. The data includes the resonant shifts for 16 microspheres in the same assay.

The binding of anti-IL-6 to the surface is observed as red shifts in the resonant wavelength, which over time reached a maximum indicating saturation of the resonator surface. The binding kinetics observed in **Figure 6.5** confirms that anti-IL6 is, in fact, being attached to the surface. This confirmation allowed us to test the overall sensor performance for the specific detection of IL-6.

6.3.4 IL-6 detection using WGM resonators

Post anti-IL-6 attachment, the specific detection of IL-6 was made by introducing a small volume 435 pg/mL stock IL-6 solution then allowed to incubate for 10 mins before measurement. Of the 16 microspheres, eight displayed linear calibrations as shown in **Figure 6.6**. The other 8 resonators did not exhibit measureable changes in resonant wavelength. This is a marked improvement in statistics in the number of WGM resonators that exhibit binding, where previously ~10% of the spheres result resonant shifts.

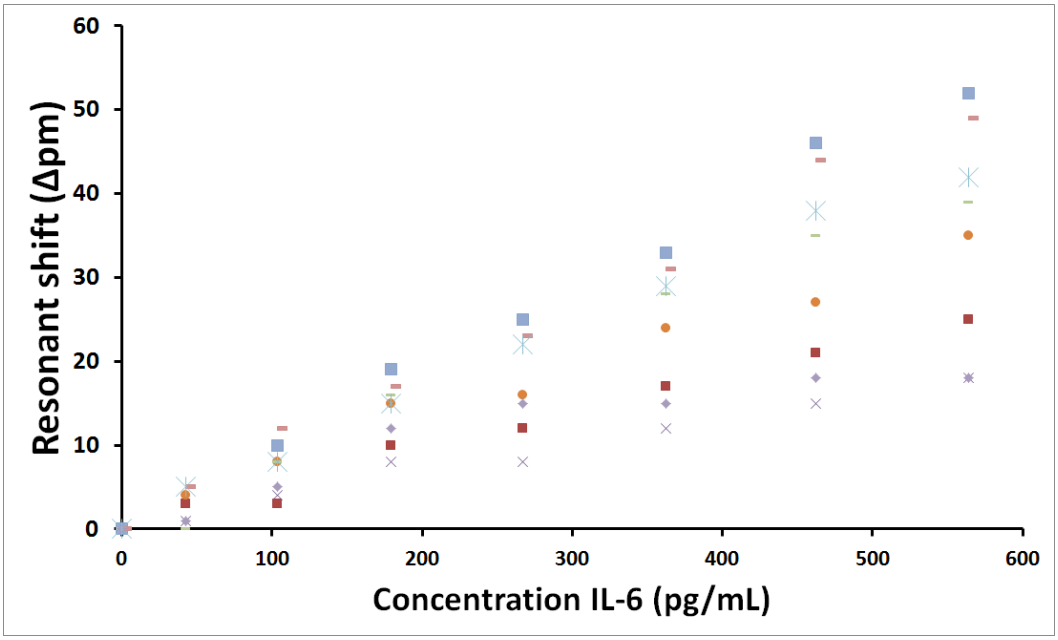

Figure 6.6. The calibration curves for IL-6 introduced to anti-IL6 functionalized spheres. Eight of the 16 microspheres produced a linear calibration while the remaining 8 observed no measurable change in resonant wavelength.

The lower efficiency observed in our experiments is an on-going investigation in the optimization of protein-surface attachment. We do observe binding of the antibody to all 16 spheres, however, only observe subsequent analyte binding in roughly 50%. We suspect several issues, such as loss of protein stability during the attachment process, detrimental tumbling of the microspheres during the functionalization reactions and low surface functional groups. We also observe varying sensitivities from resonator to resonator, this may be related to the individual quality factors of the resonator, however, it should also be noted that sphere to sphere variations in protein surface coverage could also contribute to the sensitivities.

These initial studies, however, using oxygen plasma to clean the surface and increase the surface activation energy demonstrate some improvement of the number of WGM resonators that are capable of detecting analyte binding. The improved number of responsive WGM resonators can have a

marked impact when moving towards a CE-WGM immunoassay platform where a single sphere, instead of a field of spheres, is utilized as a detector.

6.3.5 PS-WGM calibrations for BSA-biotin and IL-6 binding

The specific binding of both BSA-biotin and IL-6 were measured using the phase detection method introduced in chapter 5. Phase detection was developed to reduce noise signals ultimately to improve the detection limit using a lock-in phase detector. Phase detection also enabled the real-time monitoring of resonance shifts in phase units at sample rates of 200 Hz. Both of these criteria facilitate the use of this setup as a post-CE separations detector, where diffusion of analytes require lower detection limits and CE peak widths of roughly 30 seconds require real-time data collection.

Streptavidin was immobilized on 53 μm BT microspheres for the detection of BSA-biotin resulting in a calibration curve shown in **Figure 6.7**. A detection limit of 0.65 ng/mL (9.4 pM) BSA-biotin and a sensitivity of 0.92 degrees/ng/mL were measured.

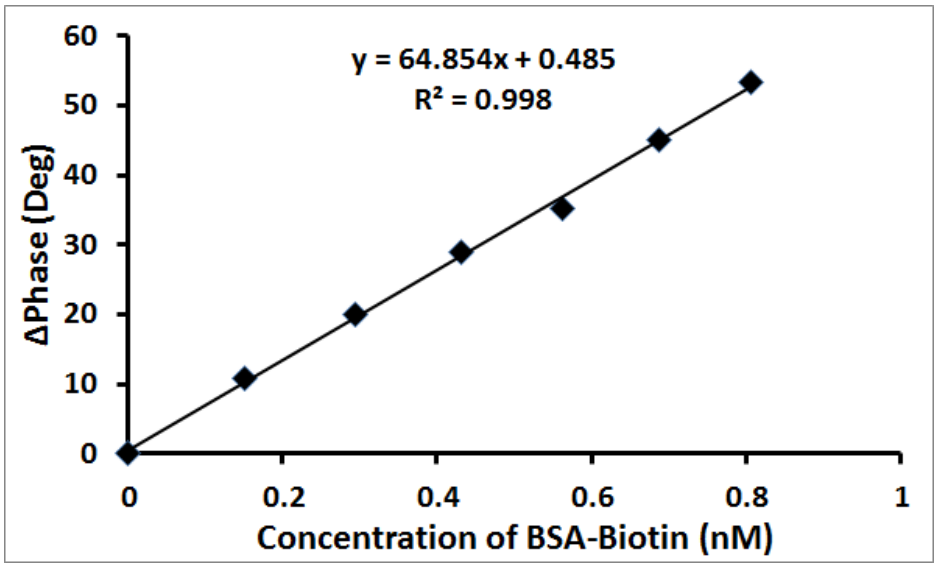

Figure 6.7. Calibration of BSA-Biotin using PS-WGM detection with streptavidin functionalized microspheres

The molecular weight of BSA-biotin was estimated using the average reported mole ratio between biotin and BSA (12 mole biotin:1 mole BSA) in this calculation. **Figure 6.8** is the calibration for IL-6 where anti-IL-6 functionalized spheres were used. A detection limit of 0.64 pg/mL (0.03 pM) and a sensitivity of 0.38 degrees/pg/mL were observed in this IL-6 assay. Using the same antibody and antigen pairing we observe a four-fold improvement in PS-WGM assays compared to the reported limit of detection of 2.5 pg/mL in commercial ELISA kit (BD Biosciences). The calibrations for both proteins exhibit good linearity correlation values ($R^2 > 0.997$).

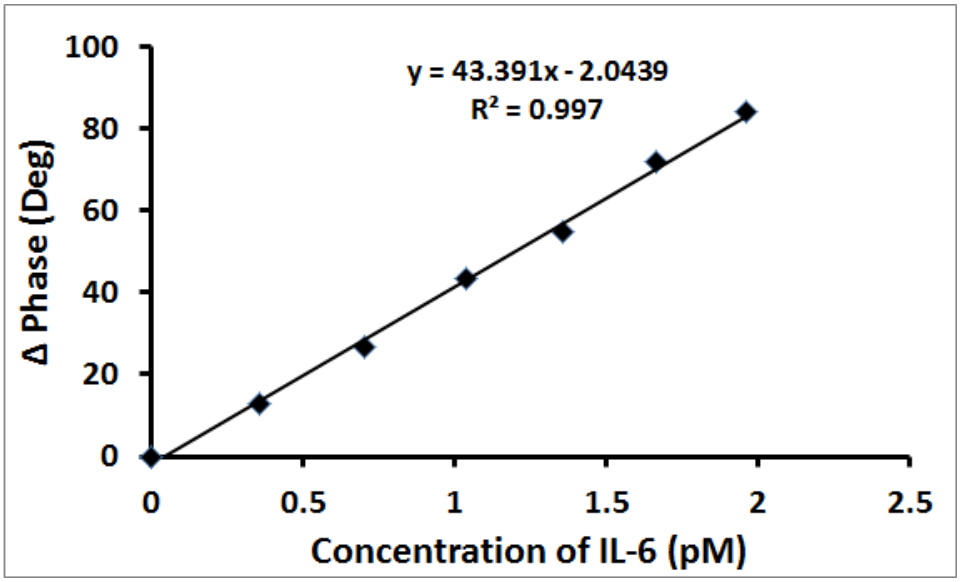

Figure 6.8. Calibration of IL-6 using PS-WGM Detection with streptavidin/biotinylated anti-IL6 microspheres

6.3.6 CE-WGM immunoassay results

BSA-biotin and IL-6 were chosen as a set of model proteins to demonstrate the utility of separation and specific detection of one the two proteins using CE-WGM immunoassays. BSA-biotin emulates the albumin in a serum protein electrophoresis, as the last detected peak while IL-6 is a cytokine that mimics a protein migrating with the beta-2 proteins. For immunoassays, dissociation constants can dictate the overall sensor performance. The binding conditions for proteins such as pH,

ionic strengths and temperature can affect the effective binding constants (K_a) of antibody-antigen, which is directly related to the sensitivity and inversely related to limits of detection. Therefore, we optimize the separation of the two proteins under physiological conditions (pH 7.4) to promote the preservation of protein structure and function during the CE separation.

For CE separation, while it is possible to use PBS as a running buffer, the high concentration of salts, such as KCl and NaCl at 27 and 1400 mM respectively, causes high ionic strengths leading to slower EOF and increased joule heating. To minimize these effects while maintaining similar buffer composition, we used 10 mM of both the monobasic phosphate and dibasic phosphate at pH 7.4. Initially, an unfunctionalized WGM resonator was placed at the outlet of capillary as shown in **Figure 6.9.** When an injection volume of 7.7 nL containing a mixture of 0.2 mg/mL BSA-biotin and 435 pg/mL IL-6 was introduced into the capillary and separated at 18 kV resulting in the electropherogram shown in **Figure 6.9**.

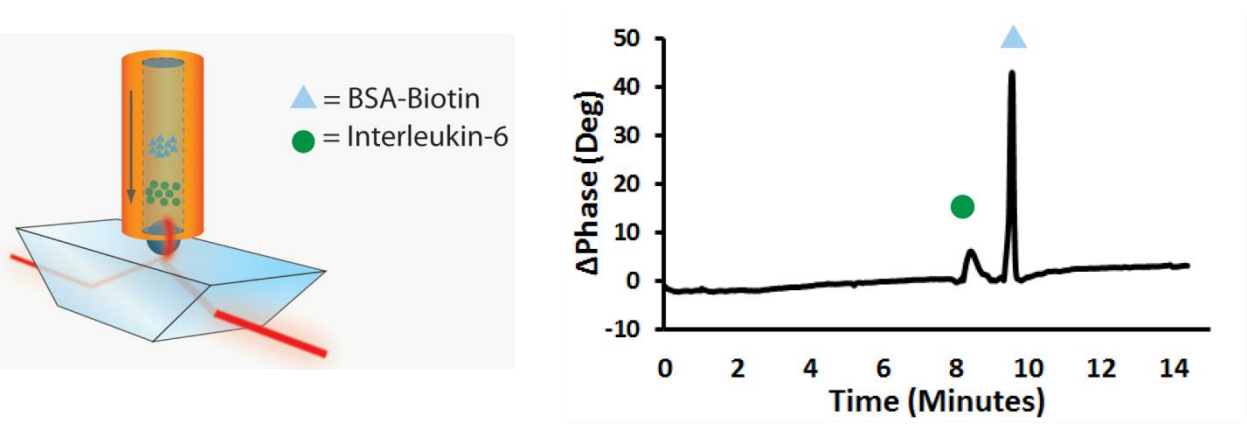

Figure 6.9. (right) Schematic of a CE-WGM interface where an unfunctionalized microsphere was placed at the outlet of the capillary to detect protein separations as bulk refractive index changes. (left) Electropherogram of the separation of IL-6 and BSA-biotin.

The resonator is responding to the bulk refractive index changes due to the protein bands that are migrating past the resonator. IL-6 and BSA-biotin bands are baseline resolved with good resolution

(Resolution = 2.3). Both protein bands returned to baseline demonstrating the detection of these plugs as they travel past the WGM resonator at the outlet. Since the resonator does not have biocapture molecules on its surface, any baseline change observed can be attributed to non-specific binding of proteins. However in our experiments, the protein bands returned back to baseline indicating that little to no non-specific binding is occurring as shown in **Figure 6.9**.

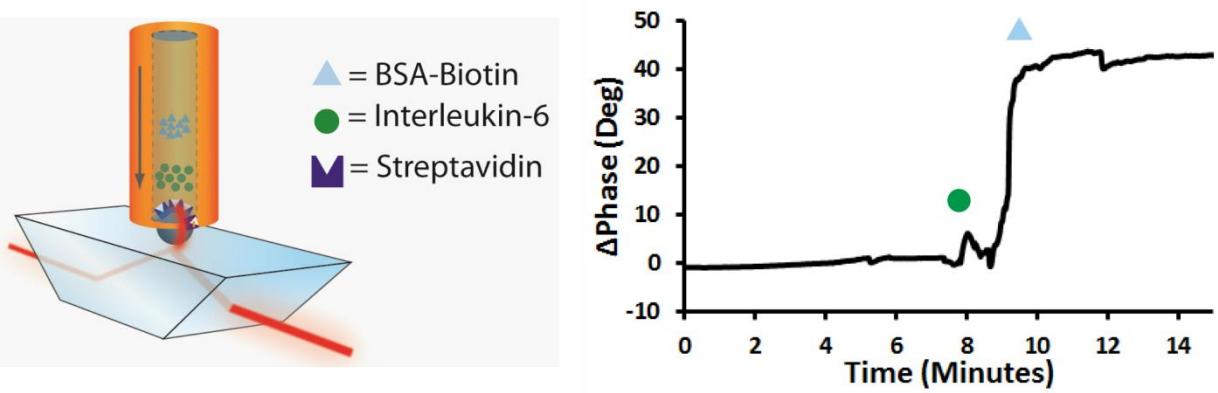

Figure 6.10. (right) Schematic of a CE-WGM interface where a streptavidin functionalized microsphere was placed at the outlet of the capillary to detect protein separations as bulk refractive index changes and specifically bind BSA-biotin. (left) Electropherogram of the separation of IL-6 and BSA-biotin. The change in baseline after the BSA-biotin peak is indicative of specific binding.

To develop a 2-D technique, like western blots, capable of separating and specifically detecting an analyte of interest, we tested the utility of CE-WGM by placing a streptavidin coated resonator at the capillary outlet. As shown in **Figure 6.10**, we specifically detect the binding of BSA-biotin after the initial electrophoretic separation between IL-6 and BSA-biotin. Unlike the previous experiment, we observed the specific binding of BSA-biotin to covalently attached streptavidin on the resonator surface as a baseline shift after the protein band. The result is shown in **Figure 6.10,** where a baseline shift of 41° in phase was observed.

CE-WGM immunoassays are especially unique due to the modularity of the immunoassay portion. CE based immunoassays typically require re-optimization of the separation which limits each assay for a single purpose. A modular CE-immunoassay system, as we demonstrate, requires the

validation of only the immunoassay portion which can be done separately from the CE optimization enabling the use of existing separations with this technique. This holds great promise as an immunoassay tool performed directly after a serum protein electrophoresis (SPE) test in the clinic. For multiple myeloma applications, the SPE done using CE-WGM immunoassay has the potential to be a diagnostic, staging and treatment monitoring tool. The next step for this project is to detect specific proteins in a complex serum matrix during an SPE. Moving towards that goal, we show initial results of clinical samples (obtained from the Biospecimen Repository at the University of Kansas) of both healthy and MM patients on CE-UV systems.

6.3.7 Separation of healthy and MM patient serum samples using CE-UV

A serum sample from multiple myeloma patient and serum sample from a healthy patient was obtained from the University of Kansas Cancer Center Biospecimen Repository Core Facility. Serum protein electrophoresis of these samples was optimized from conditions similar to previously validated serum protein electrophoresis. The WGM immunoassay for specific biomarkers will be performed after the CE separation, thus buffer choices and pH conditions were chosen to minimize the potential of misfolding proteins. Phosphate buffers can also be compatible for serum separations, however, the slightly more acidic pH range results in longer separations (18 minutes). Therefore, borate buffer at pH 10 was used for faster separations (< 8 mins). These conditions have proven to be viable for immunoassays in previous studies. The sample was diluted in water in a 1:40 serum to water ratio. A 4.9 nL sample injection was separated at 18 kV in pH 10, 30 mM borate. The healthy patient and MM patient sample separations are shown in **Figure 6.11a,b.** The M-spike observed in the MM patient electropherogram is observed as expected as a result of the overproduction of a monoclonal immunoglobulin from the proliferation of an abnormal B-cell clone. This initial separation study sets up the next steps for a combined CE-UV-WGM immunoassay test where specific biomarkers, such as free

light chains and lactate dehydrogenase can be measured using WGM directly after the observation of the SPE profile using UV.

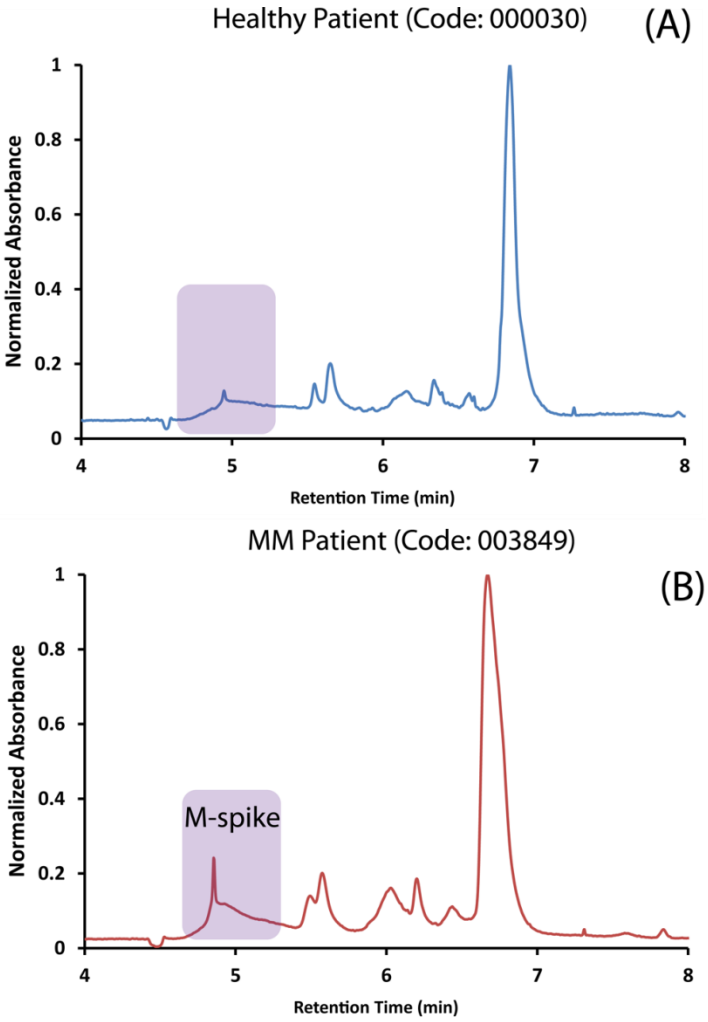

Figure 6.11. The above is a the data from SPE of a healthy (a) and multiple myeloma (b) patient. The M-spike observed in the gamma band of the SPE indicates a monoclonal gammopathy.

6.4 Conclusions

CE separations coupled with WGM resonators for immunoassays are demonstrated as a promising platform as a 2-D immuno-separation system. The functionalization of resonators with

antibodies using streptavidin/biotinylated antibodies demonstrates improvements in the WGM sensor response. We observe detection limits of 0.03 pM for IL-6, which is highly competitive compared to ELISA and CEIA of IL-6 protein (0.03 pM) using labeled fluorescence and preconcentration techniques.[39] We introduce the CE-WGM immunoassay platform for the separation of BSA-biotin and IL-6 as a proof-of-concept. We observe little to no non-specific binding of proteins even under higher concentrations at 0.2 mg/mL BSA-biotin. Additionally, we show the initial separation conditions for clinical serum samples for future application as a MM diagnostic tool.

6.5 References

1. Guzman, N. Immunoaffinity capillary electrophoresis applications of clinical and pharmaceutical relevance. *Analytical and bioanalytical chemistry* **2004**, *378*, 37-39.
2. Amundsen, L. K., et al. Immunoaffinity CE in clinical analysis of body fluids and tissues. *Electrophoresis* **2007**, *28*, 99-113.
3. Schmalzing, D., et al. Capillary electrophoresis-based immunoassays. *Electrophoresis* **2000**, *21*, 3919-3930.
4. Yeung, W., et al. Capillary electrophoresis-based immunoassay. *Journal of Chromatography B* **2003**, *797*, 217-228.
5. Dalluge, J. J., et al. Precolumn affinity capillary electrophoresis for the identification of clinically relevant proteins in human serum: application to human cardiac troponin I. *Analytical Chemistry* **1998**, *70*, 5339-5343.
6. Guzman, N. A. Improved solid-phase microextraction device for use in on-line immunoaffinity capillary electrophoresis. *Electrophoresis* **2003**, *24*, 3718-3727.
7. Phillips, T. M., et al. Analysis of recombinant cytokines in human body fluids by immunoaffinity capillary electrophoresis. *Electrophoresis* **1998**, *19*, 2991-2996.
8. Jian, L., et al. Systemic lupus erythematosus patient with false positive results of antibody to HIV: A case report and a comprehensive literature review. *Technology and Health Care* **2015**, *23*.
9. Taylor, N. Transient false-positive urine human chorionic gonadotropin in septic shock. *The American journal of emergency medicine* **2015**, *33*, 864. e861-864. e862.
10. Notkins, A. L. Polyreactivity of antibody molecules. *Trends in immunology* **2004**, *25*, 174-179.
11. Dimitrov, J. D., et al. Antibody polyreactivity in health and disease: statu variabilis. *The Journal of Immunology* **2013**, *191*, 993-999.
12. Van Regenmortel, M. H. Specificity, polyspecificity, and heterospecificity of antibody-antigen recognition. *Journal of Molecular Recognition* **2014**, *27*, 627-639.
13. Guzman, N. A., et al. An emerging micro-scale immuno-analytical diagnostic tool to see the unseen. Holding promise for precision medicine and P4 medicine. *Journal of Chromatography B* **2015**.
14. Schmalzing, D., et al. Capillary electrophoresis based immunoassays: a critical review. *Electrophoresis* **1997**, *18*, 2184-2193.

15. Strausbauch, M., et al. Concentration and separation of hypoglycemic drugs using solid-phase extraction-capillary electrophoresis. *Journal of Chromatography A* **1995**, *717*, 279-291.
16. Armenta, J. M., et al. Design and evaluation of a coupled monolithic preconcentrator-capillary zone electrophoresis system for the extraction of immunoglobulin G from human serum. *Journal of Chromatography A* **2005**, *1097*, 171-178.
17. Chen, H.-X., et al. Magnetic beads based immunoaffinity capillary electrophoresis of total serum IgE with laser-induced fluorescence detection. *Analytical Chemistry* **2008**, *80*, 9583-9588.
18. Morales-Cid, G., et al. On-line immunoaffinity capillary electrophoresis based on magnetic beads for the determination of alpha-1 acid glycoprotein isoforms profile to facilitate its use as biomarker. *Anal Chim Acta* **2013**, *773*, 89-96.
19. Ramseier, A., et al. Screening for urinary amphetamine and analogs by capillary electrophoretic immunoassays and confirmation by capillary electrophoresis with on-column multiwave-length absorbance detection. *Electrophoresis* **1998**, *19*, 2956-2966.
20. Mi, J. Q., et al. Determination of Morphine by Capillary Zone Electrophoresis Immunoassay Combined with Laser-Induced Fluorescence Detection. *Journal of Immunoassay and Immunochemistry* **2004**, *25*, 57-70.
21. Chen, H. X., et al. Antibody development to testosterone and its application in capillary electrophoresis-based immunoassay. *Electrophoresis* **2008**, *29*, 3406-3413.
22. Li, X. M., et al. Capillary electrophoresis enzyme immunoassay for alpha-fetoprotein and thyroxine in human serum with electrochemical detection. *Journal of separation science* **2008**, *31*, 336-340.
23. Kawabata, T., et al. "Electrokinetic Analyte Transport Assay" for α-fetoprotein immunoassay integrates mixing, reaction and separation on-chip. *Electrophoresis* **2008**, *29*, 1399-1406.
24. Liu, Y. M., et al. Sensitive detection of tumor marker CA15-3 in human serum by capillary electrophoretic immunoassay with chemiluminescence detection. *Journal of separation science* **2008**, *31*, 1151-1155.
25. German, I., et al. Rapid simultaneous determination of glucagon and insulin by capillary electrophoresis immunoassays. *Journal of Chromatography B: Biomedical Sciences and Applications* **2000**, *742*, 353-362.
26. Guillo, C., et al. Simultaneous capillary electrophoresis competitive immunoassay for insulin, glucagon, and islet amyloid polypeptide secretion from mouse islets of Langerhans. *Journal of Chromatography A* **2011**, *1218*, 4059-4064.
27. Moser, A. C., et al. Clinical applications of capillary electrophoresis based immunoassays. *Electrophoresis* **2014**, *35*, 937-955.
28. Huckabay, H. A., et al. Label-free detection of ovarian cancer biomarkers using whispering gallery mode imaging. *Biosens. Bioelectron.* **2013**, *45*, 223-229.
29. Huckabay, H. A., et al. Whispering gallery mode imaging for the multiplexed detection of biomarkers. *Sens. Actuators, B* **2011**, *160*, 1262-1267.
30. Soria, S., et al. Optical microspherical resonators for biomedical sensing. *Sensors* **2011**, *11*, 785-805.
31. Ahluwalia, A., et al. A comparative study of protein immobilization techniques for optical immunosensors. *Biosensors & bioelectronics* **1992**, *7*, 207-214.
32. Laboratories, B., Working with Microspheres; **2013**.
33. Watanabe, H., et al. Optimizing pH response of affinity between protein G and IgG Fc how electrostatic modulations affect protein-protein interactions. *Journal of Biological Chemistry* **2009**, *284*, 12373-12383.
34. Weber, P. C., et al. Structural origins of high-affinity biotin binding to streptavidin. *Science* **1989**, *243*, 85-88.

35. Kim, D., et al. Protein immobilization techniques for microfluidic assays. *Biomicrofluidics* **2013**, *7*, 041501.
36. Neubrand, A., et al. Room-Temperature Solubility Behavior of Barium Titanate in Aqueous Media. *Journal of the American Ceramic Society* **2000**, *83*, 860-864.
37. Yoon, D.-H., et al. Barium ion leaching from barium titanate powder in water. *Journal of Materials Science: Materials in Electronics* **2003**, *14*, 165-169.
38. Bhattacharya, S., et al. Studies on surface wettability of poly (dimethyl) siloxane (PDMS) and glass under oxygen-plasma treatment and correlation with bond strength. *Microelectromechanical Systems, Journal of* **2005**, *14*, 590-597.
39. Phillips, T. M. Rapid analysis of inflammatory cytokines in cerebrospinal fluid using chip-based immunoaffinity electrophoresis. *Electrophoresis* **2004**, *25*, 1652-1659.

6.6 Appendix

Barcode	Year Dx'ed	Primary Ca Dx	Year Collected	Previously treated?	Race	Ethnicity	Sex
003849	2004	Multiple myeloma	2012	yes	White	Non-His	Male
004803	2011	Multiple myeloma	2012	yes	Black or Afr-Am	Non-His	Male
005663	2013	Multiple myeloma	2013	yes	White	Non-His	Male
008224	2012	Multiple myeloma	2013	yes	White	Non-His	Male
008498	2007	Multiple myeloma	2013	yes	White	Non-His	Female
000030	n/a	control	1995	n/a	Black or Afr-Am	Non-His	Female
000028	n/a	control	1995	n/a	Other	Hispanic	Female
000027	n/a	control	1995	n/a	White	Non-His	Female
000021	n/a	control	1995	n/a	White	Non-His	Female
000016	n/a	control	1995	n/a	White	Non-His	Female

Appendix 1 – Information of all samples obtained from KU Cancer Center Biospecimen Repository Core Facility.

Chapter 7

Summary and Future Directions

7.1 Summary

Our goals were to develop WGM optical resonator for their use in the clinical setting. The compact size, high sensitivity and cost effective features of glass microsphere resonators allow numerous designs and implementation for instrumentation development. We have geared this project for the application of cancer diagnostics where implementation of an early detection and routine screening test can tremendously improve cancer patient outlook.

7.1.1 Immobilization of microspheres and lipid layer detection

In chapter 3, we discuss the development of a microsphere immobilization approach to enable the incorporation of microspheres with fluidic systems. For immunoassays, fluid exchanges such as sample introduction, incubation, washing and regeneration steps all require the movement of fluids. These fluid exchanges can perturb the WGM resonance such that the resonant wavelength may no longer be tracked during an assay. To overcome this challenge we modified a method using calcium/alconox solutions for WGM resonators optimizing quality factors and microsphere adhesion to the substrate.[1] This approach enabled WGM resonators to be physically stable during routine fluid changes for a more robust detection platform.[2] Furthermore, the immobilization method enabled the transfer of Langmuir-blodgett (LB) films to immobilized WGM resonators.[2] The precise control of the composition of LB films allowed a controlled study of sensor performance based on dye concentrations.

WGM imaging requires the functionalization of a fluorescent dye to the surface of the microsphere to characterize the resonant condition. Light stored within the resonator cavity experiences losses due to the absorption by the fluorophore. While absorption is known to effect Q, the precise dye loading that could be tolerated, however, had not been characterized due to limitations in the controlling dye concentration. The use of LB films, which enable fine compositional control, with immobilized microsphere resonators allowed a system where dye loading effects could be determined. The LB and microsphere resonator platform also was demonstrated as a biosensor where a bilayer containing ganglioside membrane 1 (GM1) was used to specifically detect the binding of cholera toxin-beta subunit.[2] This platform holds promise for membrane mimic studies where the analysis of lipid-protein and protein-membrane protein interactions can be performed.

7.1.2 Improvements of resonator performance

In chapter 4, we explored various aspects of the platform to further improve the Q-factor of the resonators. As the goal was to develop the WGM imaging method, we first focused on ways to improve quality factors in the prism light coupling system. We introduced the use of refractive index matched coating to create a gap between the resonator and its coupling surface. This improved the quality factor up to two orders of magnitude while maintaining the ability to excite a field of spheres required for multiplexing. In an effort to further improve the platform, the dye loading study performed in chapter 3 encouraged us to explore different ways of capturing the WGM resonance signal without sacrificing any resonator performance. Instead of using dye fluorescence, used in WGM imaging, we utilized evanescent wave scattering to track WGM resonances.

Evanescent wave scattering leads to strong signals that appear when a microsphere is placed close to the light coupling surface.[3,4] Using these signals as a WGM resonance reporter has numerous advantages compared to the WGM imaging platform. Scattering signals are solely dependent on the

intensity of the laser output and are not susceptible to photobleaching, as is the case for dye used in WGM imaging. Additionally, the removal of dye from the surface of the resonator improves quality factors which can increase sensor performance. Another benefit of scattering signals is that less sensitive and inexpensive cameras can be used which are also compatible with high throughput analysis tools such as LabView. We demonstrated the detection of interleukin-6 with the developed scattering WGM platform. Based on our initial studies, we observe a sensitivity of 205 pm/ng/mL for IL-6, using scattering WGM compared to sensitivity of 15 pm/ng/mL for prolactin using WGM fluorescence imaging.[5] These proteins are similar in molecular weight (24 kDa) and have no appreciable difference in binding constants for their respective antibodies. The sensitivity improvement may be due to the lack of the dye molecules. This allows 1) increased sensor surface coverage with antibodies as they do not compete with binding sites with dye molecules. 2) The removal of dye improves resonator quality factors which lead to better sensor performance.[6,7] Moving forward, the ease of obtaining an evanescent wave scatter signal provides a flexible platform when incorporating WGM resonators into various fluidic platforms.

7.1.3 Scattering WGM and implementation into microfluidics

Scattering WGM allows for a non-photobleaching signal which enables long term tracking of WGM resonances for applications such as capillary electrophoresis. We explored several fluidic platforms using microfluidics, digital fluidics and capillary electrophoresis (CE). Chapter 4 describes T-channel microfluidic chips with WGM resonators held by a diamond-shaped well that was integrated within the channel. Another design shows the implementation of many microspheres in a 16-channel microchip that held microspheres with the tapering in the width of the channels. The small micron-sized microspheres seem well suited for the microfluidic technologies and holds significant promise as detectors for these applications.

We also demonstrate the detection of refractive index differences in two droplets using a fiber-sphere as a dip sensor based on WGM resonators. The advantages of being a modular and hand-held type detection platform can be integrated with droplet based microfluidic chips. The fabrication of the tapered fiber and microsphere resonators was described and used to detect the RI difference between two droplets alternately dipping the sensor in water and 5% glycerol. We envision this dip platform to be used in tandem with digital microfluidic technology, which offers excellent droplet manipulation capabilities. This platform, however, requires further development with concern as to the translatability into a practical, clinic-ready device.

7.1.4 WGM detectors for CE separations

In chapters 5 and 6, we introduce WGM resonators to capillary electrophoresis as an end-on detector for separations. Though we initially demonstrate WGM detectors for bulk refractive index measurements in a separation of three cations, our ultimate goal is to demonstrate the flexibility of WGM as both a general detector and a specific sensor in capillary separation systems. First, we demonstrate that WGM resonators are compatible with EOF such that sample peak profiles are undisturbed in the separation of sodium, potassium and lithium cations.[8]

Next, we demonstrate the use of CE to separate two proteins (BSA-biotin and IL-6) based on their differences in electrophoretic mobility then we utilize WGM resonators coated with streptavidin to specifically detect BSA-biotin. These initial studies provide a unique 2-D detection platform compatible with all existing separations. The CE separation is undisturbed in this technique so all previously optimized separation conditions can be used with bioaffinity molecule functionalized WGM resonators, to obtain 2nd dimensional information.

7.2 Future Directions

There is growing interest in the development of compact devices that can analyze patient samples as a point-of-care device. These devices offer near-patient and quick result turnaround that can provide much needed information of the patient state.[9,10] To achieve this, the device must be a robust, fluidic platform with detection schemes that are inexpensive, compact and highly sensitive. Microvolume based fluidic systems such as microfluidics and capillary electrophoresis offer attractive characteristics for the development of diagnostic devices. We have presented initial results and demonstrated the potential of WGM resonators as a sensitive, label-free and compact detector in various fluidic platforms. The integration of these detectors into microfluidic devices provides a general and flexible detection scheme that can be utilized for diagnostics. We propose several WGM platforms that have the potential to analyze complex matrices such as blood and serum for use as a diagnostics.

7.2.1 Digital microfluidics for blood analysis using WGM

Microfluidics is an enabling technology that has catalyzed the field of miniaturized analysis systems for numerous applications.[11-14] Clinical diagnostics is one of the most promising avenues for the implementation of these devices for use as a routine screening tool. Measurement of physiologically relevant fluids can reveal critical information about the patient's health and can significant aide in the treatment of a disease. Miniaturized systems enjoy benefits of smaller sample requirement, reduced reagent consumption and lower cost. Currently, most microfluidic devices are a based on continuous flow and utilize electrophoretic flow (EOF). However, many common samples such as whole blood and urine cannot be pumped using EOF due to their high ionic strengths that lead to excessive joule heating and thus efforts have been made to develop alternative pumping mechanisms.[11,15] Active pumping mechanisms such as centrifugation have attracted a lot of attention in more recent years leading to the development of disposable plastic microchips to detect glucose, lactate and O_2 levels in whole blood.[15]

Commercial devices utilize external pressure sources or passive flow such as capillary action or gravity for whole blood analysis in microfluidics. Devices such as the Biosite Triage Cardiac system and the I-Stat analyser are popular microfluidic devices for measurement of cardiac biomarkers and blood chemistry, respectively.[15] Most of these devices have single-use microfluidic modules that become disposable. This typically leads to application specific devices which offer little flexibility and scalability in their design. For blood analysis in a point-of-care setting, it is ideal to have a flexible platform that can perform a list of tests on the same microchip.

Digital microfluidics uses a non-continuous flow system with precise control of droplet movement into distinct locations via electrowetting.[14,16,17] These devices can be designed for dispensing, transport, splitting, merging and mixing of aqueous droplets.[17] Also they have been demonstrated to preserve enzyme activity and protein structure on an electrowetting chip required for binding assays.[11] These devices therefore offer several advantages for the evaluation of biomarkers in blood for clinical diagnostics. Typically detection in these devices uses fluorescence, where additional reagents or labeling must be used to generate a fluorescence signal. Other offline detection schemes such as mass spectrometry have been demonstrated but for blood analysis would require expertise in mass spectrometry analysis therefore less viable for a point-of-care device.[18] As such, we see an opportunity for WGM resonator with digital microfluidic systems to provide a general, label-free and sensitive detection scheme.

We have previously demonstrated the ability to perform sensitive immunoassays within droplets using WGM resonators. Small droplets with improved mass transport enabled initial binding rate assays where initial slopes can be related to the concentration of the analyte.[19] This has the significant advantage of not requiring standard addition for the quantitation of analytes.[19] WGM resonator in droplet assays provides a rapid, on-chip detection platform for digital microfluidic devices.

We hope to combine the on-chip sample preparation using digital microfluidics with small footprint WGM resonators to detect biomarkers for diseases in whole blood in a device as shown in **Figure 7.1.**

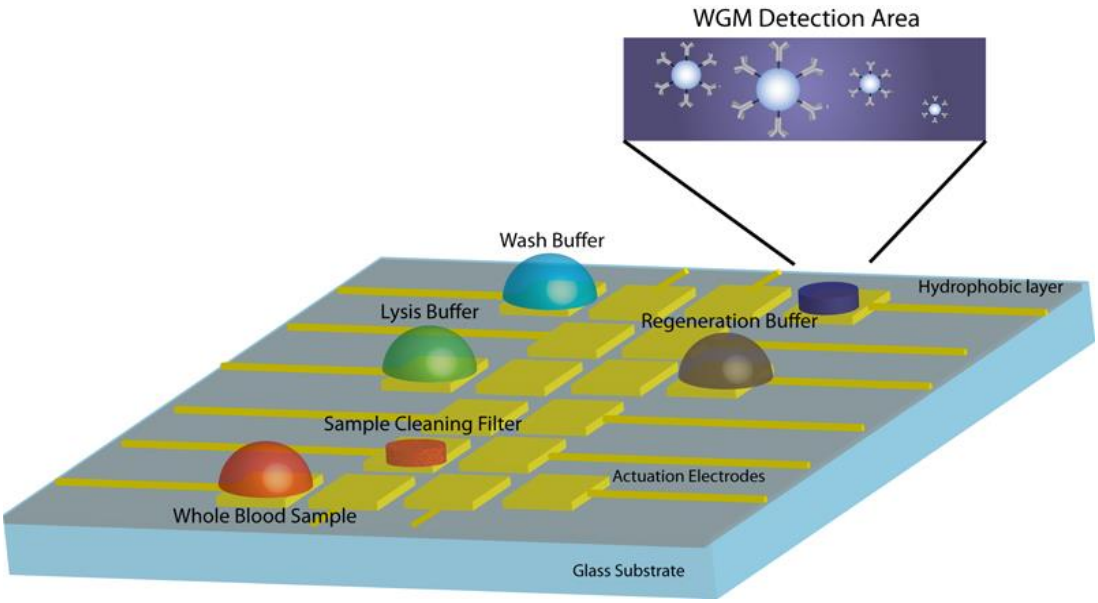

Figure 7.1. Illustration of a design for blood sample analysis using DMF and WGM resonators. All of the steps required to analyze blood such as, sample cleaning, cell lysing, washing, detection and sensor regeneration can be done on this droplet platform.

This initial design has designated areas for the cleaning of whole blood cells to remove cells in preparation for a less complex matrix. The remaining volume contains diagnostically relevant material such as dissolved proteins in a less viscous fluid suitable for WGM resonator detection. Other reagents for resonator washing, cleaning and regeneration solvents can be loaded into the chip as shown in **Figure 7.1**. We hope to take advantages of both WGM resonator and digital microfluidic chips to create a clinical tool that is modular, flexible and scalable for a point-of-care diagnostics.

7.2.2 Serum Protein Electrophoresis for Diagnostics

As shown in chapter 6, a CE-WGM immunoassay device was developed where the separation and specific detection of protein was performed in an integrated platform. We plan to further develop this device and adapt the instrument for serum protein electrophoresis (SPE). SPE are already performed and validated for the clinic as an initial diagnostic screening tool, however, they require additional tests such as immunoassays to diagnose for a variety of diseases.[20] As shown in **Figure 7.2,** abnormal profiles, of either an increase (multiple myeloma, nephrotic syndrome and hepatic cirrhosis) or decrease (anti-trypsin deficiency) of certain peaks, compared to the healthy profile, highlighted in blue, can be indicative of the associated diseases.

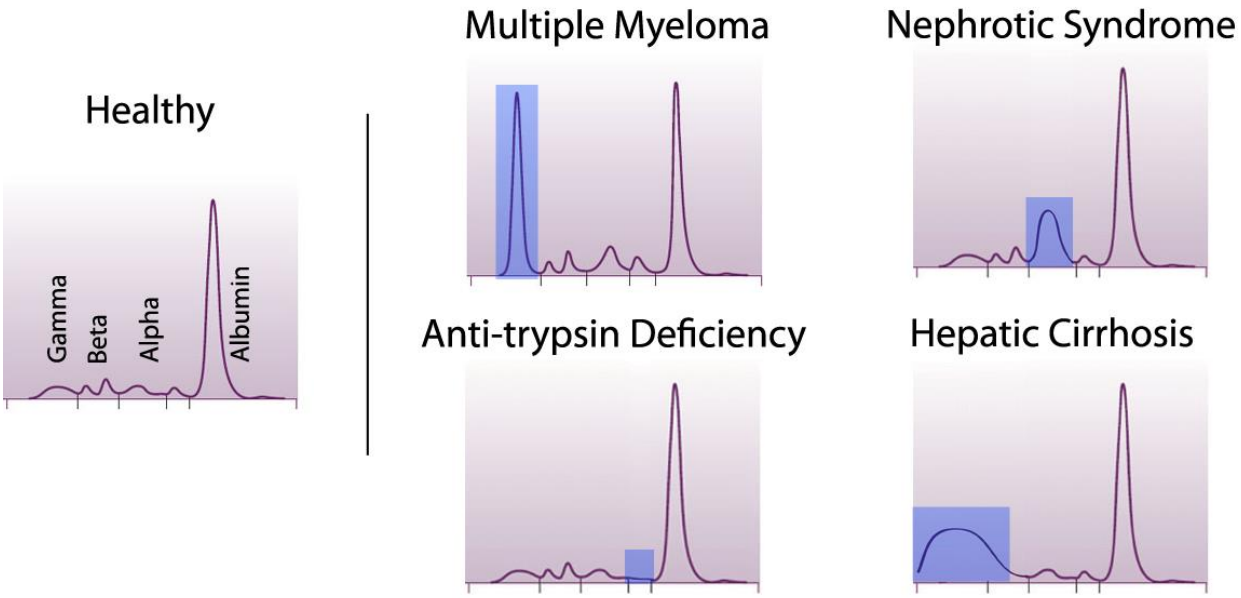

Figure 7.2. (left) CE SPE profile for a health sample containing normal peak intensities in all four zones (gamma, beta, alpha and albumin). (right) SPE profiles for four diseases where an abnormal peak is observed in the SPE profile.

Even though CE-WGM immunoassays can be helpful for the diagnosis of all of these diseases, we focus primarily on multiple myeloma (MM), where the disease demands constant and routine screening due to its 100% recurrence rate.

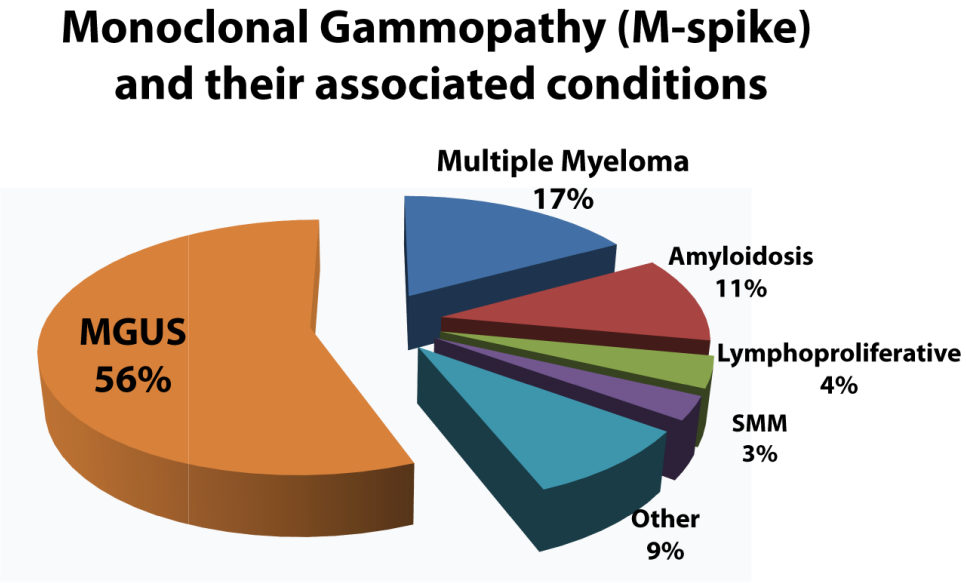

Figure 7.3. A distribution chart of 1,516 SPE tests that exhibited an M-spike. Of the 1,516 M-spikes observed, 56% are attributed to monoclonal gammopathy of unknown significance, 17% are attributed to multiple myeloma.

SPE can exhibit an abnormal spike in the gamma band (M-spike) which may be indicative of several conditions as shown in **Figure 7.3**. As seen in the figure, out of 1,516 tests, monoclonal gammopathy of unknown significance (MGUS) accounts for 56% of M-spikes observed, while only 17% are indicative of MM.[21] Thus, SPE and M-spike observations alone are not an efficient screening tool for MM as most of the cases result in an "unknown significance" diagnosis. To classify and diagnose patients that exhibit M-spikes, there are two serum based immunoassays that hold significant promise for multiple myeloma diagnosis, classification and treatment monitoring. One is an assay measuring the ratio of κ to λ light chains, known as the free light chains or Bence Jones protein, that have both

diagnostic and prognostic value.[22-24] The second is measurement of β_2-microglobulin that can improve staging schemes for multiple myeloma.[25]

Free light chains are antibody light chains that are not bound to the heavy chains. They are elevated in the serum and urine of MM patients. Additionally, unusual ratios of κ to λ light chains can help assess the risk of developing MM.[22,24] Free light chains also have short half lives in the plasma being cleared within hours versus monoclonal gammopathy (M-spike) proteins that take days to weeks.[24] Therefore, measurement of free light chains can enable patient surveillance during treatment to allow more responsive dosing and adjustment of therapeutics. Their concentrations in plasma range from the medium to high μg/mL which is well within the analytical capabilities of WGM bioassays.

Another development for improved staging of MM was recently introduced which has led to better prognostic capabilities. This staging scheme is based on measuring the levels of β_2-microglobulin and serum albumin.[25] While serum albumin levels can be obtained from the initial SPE separation, as it is detected in its own band, β_2-microglobulin co-migrates with other proteins in the beta-2 band and requires separate immunoassays. An additional biomarker, lactate dehydrogenase (LDH) which is involved in tumor initiation and metabolism, can also be included to monitor cancer burden in MM patients. The quantitation of free light chains, β_2-microglobulin and LDH can provide useful information for patients that either have or are suspected for MM. Our current developed CE-WGM immunoassay is limited to a single functionalized sphere placed directly at the outlet of the capillary. While it is possible to physically direct the outlet of a capillary to a different microsphere as a means to detect another biomarker, this would be difficult in practice and cannot easily be automated. We show initial studies using a novel capillary to microfluidics platform, shown in **Figure 7.4** that is capable of directing the eluent into separate channels within the microchip.

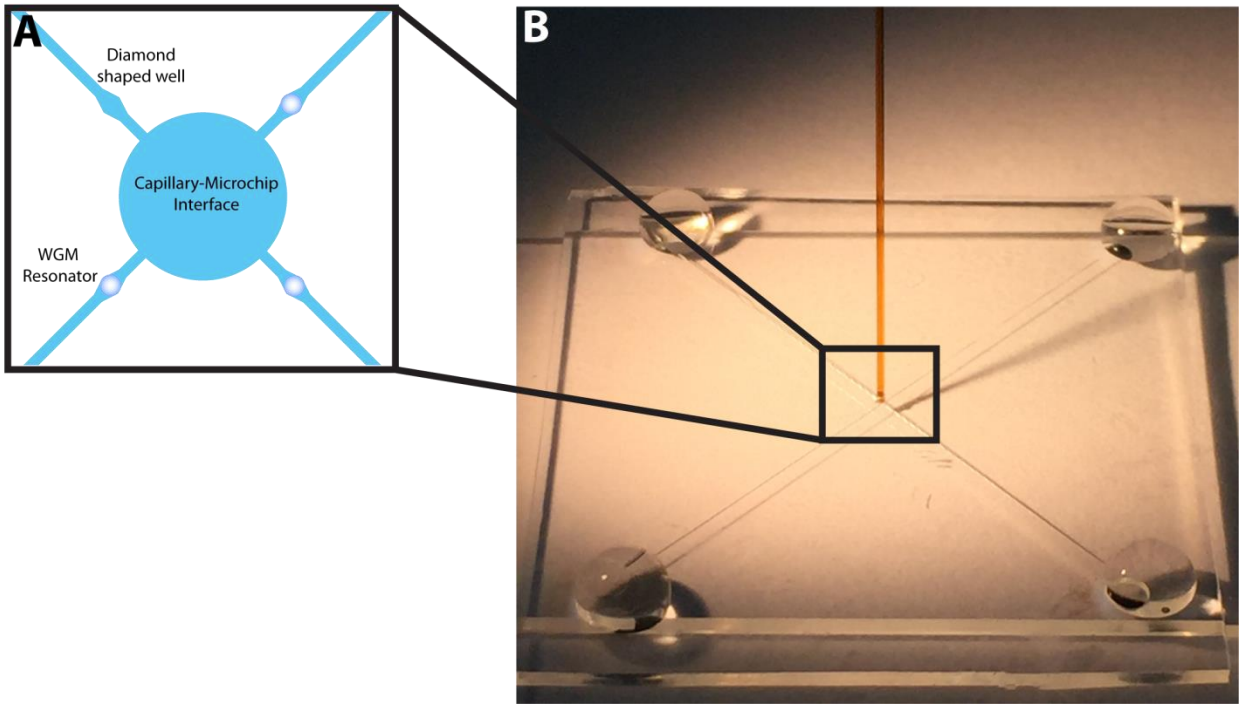

Figure 7.4. CE-Microchip Interface. (a) shows an illustration of at the interface where WGM resonators are placed along the microchip channel. (b) Image of the device is shown where a 365 um O.D. and 75 um I.D. capillary is interfaced with a microchip with channel widths of 75 um. Each channel contains buffer solution with outlets on opposite corners of the device.

Figure 7.4a illustrates the diamond-shaped wells integrated along each microchannel that is fabricated such that the maximum width of the well is ~5 μm greater than the diameter of WGM microspheres. This ensures that the resonator can be held within the well while being exposed to the contents of the microchannel. The interface between the capillary and the microchip was achieved by pre-drilling a hole in the microchip with the size of the outer diameter of the capillary and sealing with UV glue. The resulting device is shown in **Figure 7.4b.** The capillary is interfaced at the center of the microchip which splits into four subsequent microchannels. This design enables physical separation of contents that exit from the capillary into each channel. This is achieved by modifying the location of the ground electrode to direct the flow to a specific microchip channel as shown in **Figure 7.5.**

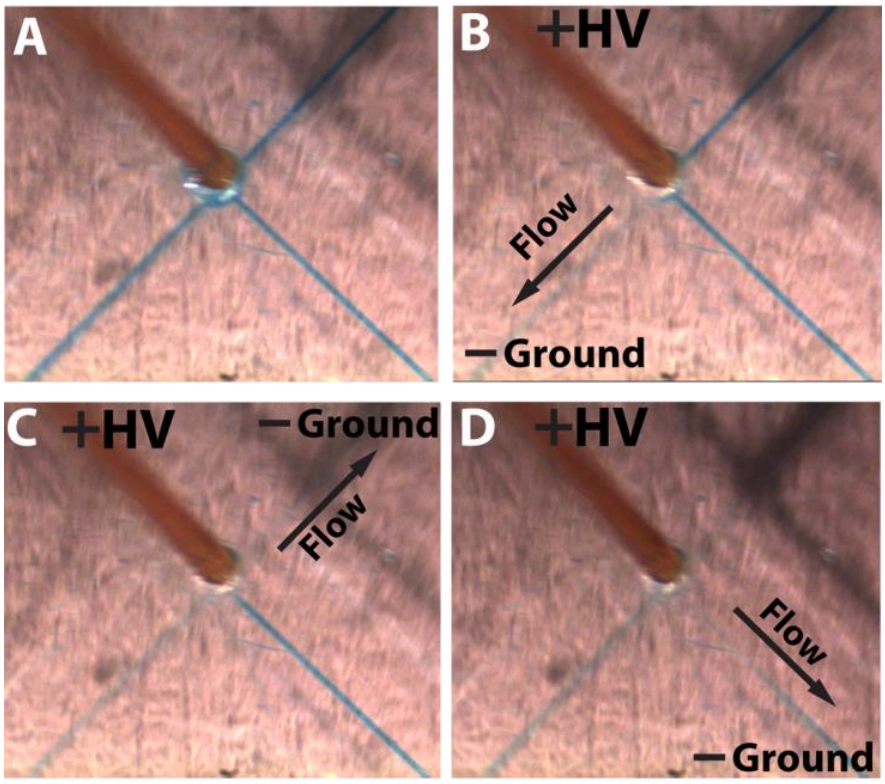

Figure 7.5. Images obtained of the capillary-microchip interface. The microchip channels were filled with blue solution. EOF was produced by placing the +HV at the inlet of the capillary and –ground at one of the outlets of the microchip. The EOF is directed towards the ground electrode thus the eluent from the capillary can be directed. (a) Pre-filled microchip (b) Ground electrode placed in bottom left channel outlet. (c) Ground placed in top right channel outlet. (d) Ground electrode placed in bottom right channel outlet.

In this experiment the microchip channels were prefilled with diluted blue food coloring using pressure flow as shown in **Figure 7.5a**. Afterwards, the capillary was filled with phosphate buffer saline (clear solution) and the ground was placed at the outlet of the bottom left microchannel. This resulted in EOF that travels down the bottom left microchannel as shown by the blue fluid being displaced by the contents from the capillary, **Figure 7.5b.** Then, the ground electrode was placed into the bottom right microchannel, directing the capillary flow into this microchannel, **Figure 7.5c**. The same concept was demonstrated for the top right channel in **Figure 7.5d**. This device can enable multiplexed detection of free light chains, β_2-microglobulin and LDH. These proteins elute in separate bands within the serum protein electrophoresis profile as shown in **Figure 7.6.** Each channel will contain a WGM microsphere

functionalized to bind each analyte for the quantitation of these biomarkers. The interface takes advantage of the already clinically validated SPE test and extends the utility by adding a specific assay.

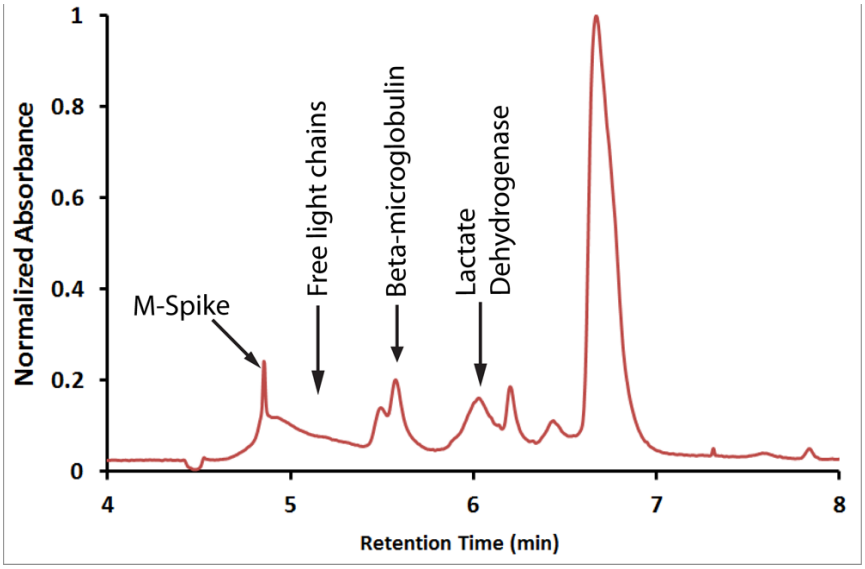

Figure 7.6. Biomarkers related to MM such as free light chains, beta-microglobulin and lactate dehydrogenase elute in separate locations in the SPE.

Several validation steps of the interface must be performed to ensure that there is limited cross-talk between the microchannel at the interface. It is important to characterize the amount of cross-talk to ensure that each analyte from the SPE separation can be directed to the appropriate WGM resonator for specific binding. Furthermore, a COMSOL simulation of the flow at the interface can elucidate the flow physics into each channel when the ground electrode is moved from one microchannel to another. However, initial studies using this device hold significant promise as a clinical tool for the multiplexed detection of several analytes of species in a CE separation system.

7.3 References

1. Allen, P. B., et al. Calcium-Assisted Glass-to-Glass Bonding for Fabrication of Glass Microfluidic Devices. *Anal. Chem. (Washington, DC, U. S.)* **2008**, *80*, 7153-7157.
2. Kim, D. C., et al. Integration of microsphere resonators with bioassay fluidics for whispering gallery mode imaging. *Analyst* **2013**, *138*, 3189-3195.
3. Bike, S. G. Measuring colloidal forces using evanescent wave scattering. *Current opinion in colloid & interface science* **2000**, *5*, 144-150.
4. Bike, S., et al. Measurements of double-layer repulsion for slightly overlapping counterion clouds. *International Journal of Multiphase Flow* **1990**, *16*, 727-740.
5. Huckabay, H. A., et al. Label-free detection of ovarian cancer biomarkers using whispering gallery mode imaging. *Biosens. Bioelectron.* **2013**, *45*, 223-229.
6. Soria, S., et al. Optical microspherical resonators for biomedical sensing. *Sensors* **2011**, *11*, 785-805.
7. Gorodetsky, M. L., et al. Optical microsphere resonators: optimal coupling to high-Q whispering-gallery modes. *J. Opt. Soc. Am. B* **1999**, *16*, 147-154.
8. Kim, D. C., et al. Integrating Whispering Gallery Mode Refractive Index Sensing with Capillary Electrophoresis Separations Using Phase Sensitive Detection. *Analytical Chemistry* **2015**.
9. Tüdős, A. J., et al. Trends in miniaturized total analysis systems for point-of-care testing in clinical chemistry. *Lab Chip* **2001**, *1*, 83-95.
10. Yager, P., et al. Point-of-care diagnostics for global health. *Annu. Rev. Biomed. Eng.* **2008**, *10*, 107-144.
11. Fair, R. B., et al. Chemical and biological applications of digital-microfluidic devices. *Design & Test of Computers, IEEE* **2007**, *24*, 10-24.
12. Mousa, N. A., et al. Droplet-scale estrogen assays in breast tissue, blood, and serum. *Science Translational Medicine* **2009**, *1*, 1ra2-1ra2.
13. Barbulovic-Nad, I., et al. Digital microfluidics for cell-based assays. *Lab Chip* **2008**, *8*, 519-526.
14. Choi, K., et al. Digital microfluidics. *Annual review of analytical chemistry* **2012**, *5*, 413-440.
15. Srinivasan, V., et al. An integrated digital microfluidic lab-on-a-chip for clinical diagnostics on human physiological fluids. *Lab Chip* **2004**, *4*, 310-315.
16. Wheeler, A. R. Putting electrowetting to work. *Science* **2008**, *322*, 539-540.
17. Cho, S. K., et al. Electrowetting on dielectric (EWOD): new tool for bio/micro fluids handling. *Biochip Journal* **2008**, *2*, 79-96.
18. Jebrail, M. J., et al. A digital microfluidic method for dried blood spot analysis. *Lab Chip* **2011**, *11*, 3218-3224.
19. Wildgen, S. M., et al. Whispering Gallery Mode Resonators for Rapid Label-Free Biosensing in Small Volume Droplets. *Biosensors* **2015**, *5*, 118-130.
20. Harris, N. S., et al. *Multiple myeloma and related serum protein disorders: an electrophoretic guide*; Demos Medical Publishing, 2012.
21. Mayo Clinic: Monolonal Gammopathy.
22. Jenner, E. Serum free light chains in clinical laboratory diagnostics. *Clinica Chimica Acta* **2014**, *427*, 15-20.
23. Tate, J. R., et al. Practical considerations for the measurement of free light chains in serum. *Clinical chemistry* **2003**, *49*, 1252-1257.
24. Graziani, M. S., et al. Serum free light chain analysis in the diagnosis and management of multiple myeloma and related conditions. *Expert review of molecular diagnostics* **2014**, *14*, 55-66.

25. Greipp, P. R., et al. International staging system for multiple myeloma. *Journal of Clinical Oncology* **2005**, *23*, 3412-3420.